UNIVERSITY OF CALIFORNIA

Los Angeles

Optical Communication With Micromachined Corner Cube Reflectors

A dissertation submitted in partial satisfaction of the

requirements for the degree

Doctor of Philosophy in Electrical Engineering

By

Patrick Breckow Chu

1998

The dissertation of Patrick Breckow Chu is approved.

William Kaiser

Ming C. Wu

Emily A. Carter

Kristofer S. J. Pister
Committee Chair

University of California, Los Angeles

1998

This dissertation is dedicated to my mother, my aunt,
and the Lord my God.

Contents

List of Tables

List of Figures

Acknowledgements

I praise God for giving me the opportunity to attend UCLA for graduate school and to spend the past few years doing MEMS research under the instruction of Dr. Kristofer Pister. I owe many thanks to many people around me and I will try to take this opportunities to express my thanks.

First I would like to thank my advisor Dr. Pister for his guidance, patience, creativity, and unlimited optimism in accomplishing the seemingly unachievable. I believe he has most definitely brightened my views on research. I also wanted to thank him for providing financial support during the majority of my graduate career. I must also thank DARPA for funding this research.

I also want to thank all the past and present KPGroupers such as Gisela Lin, Roger Lo, Richard Yeh, Brett Warneke, Bev Eyre, Ezekiel Kruglick (and the list goes on) for their technical assistance and comradery which added much life and color to my graduate career. I especially want to thank now Dr. Gisela Lin, who had encouraged me to take my first step into the MEMS world (during breakfast at Hershey Hall) and who is responsible for nearly all the excellent SEM photos in this dissertation. Roger Lo had also been most helpful during the many computer crisis I encountered. I would like to acknowledge Victor Hsu at UCB for many discussions on optical simulations. I also wanted to acknowledge my undergraduate assistants over the years including Erik Liu, Mark Tachiki, Jeff Huang, and Jeff Chen.

I want to thank Dr. Emily Carter, Dr. Bill Kaiser, and Dr. Ming Wu for taking time to be on my committee. Dr. Carter's detailed reading of my dissertation is especially appreciated. I also want to thank Dr. Wu's group and Dr. Kaiser's group (especially Shi-Sheng Lee and Mike Pottenger), Dr. Chih-Ming Ho's group (especially Wen Li, Kevin Tseng, and Winn Hong) for their help in many different

circumstances.

I would also like to thank Dr. Oscar Stafsudd and his group (including Dr. Phyllis Nelson and David Chang) for many insightful optics discussions and help. I especially appreciated Dr. Stafsudd's welcoming and encouraging attitude to provide instructions and advice. I also want to thank Balaji Sridharan from Dr. C.-J.Kim's group for his help with SAM coating. My appreciation also goes to Dr. Ioannis Kanellakopoulos for many technical discussions, LaTeX help, and general encouragement.

Special thanks go to Tom Kwon for helping me in my long range CCR experiments, Erik Berg for his electronics help in the first CCR demo, Rich Mylin and Dan Wax for allowing me to carry my experiments in Pauley and in John Wooden Center. Many thanks also go to Makoto Muira for wire bonding, members of the Center for High Frequency Electronics for wire bonding and dicing, the staff of Nanoelectronics Research Facility especially Steve Franz and Tom Lee for maintaining the cleanroom and for building the XeF_2 etcher. Many thanks also go to the EE department staff especially Jeannie Alt, Selene Baldenegro, Leticia Dominguez, Dorothy Tarkington, and Telly Vourakis.

I also feel privileged to have an opportunity to work with Dr. Bill Tang's MEMS group at JPL. I want to thank the different members of his group especially Dr. Howard Rockstad and Dr. Tony Tang for many insightful technical discussions and useful lessons in MEMS fabrication and for letting me characterize my devices with their Wyko white light interferometer.

I would like to thank the encouragement and prayers from many friends from CCF (Chinese Christian Fellowship), AACF (Asian American Christian Fellowship), and my church (Venice Santa-Monica Free Methodist Church). I know that

God has answered many of your (and my) prayers. In addition, many of you also allowed me to spend nights at your apartments, which I greatly appreciated. I don't think a long list of names is needed here because He already knows who you are.

I most certainly want to thank my family, especially my mom, who had made many sacrifices to put me through many years of education, and my aunt, who had provided many nourishing lunches and dinners so that I could survive these graduate years. I owe my family much thanks for their patience and encouragements while I struggled to graduate. And thank God, the end of my graduate career is here.

Finally, I would like to acknowledge God for His faithfulness during these years, always providing when I am in need, for His wisdom so I can see His great work in my life, and for His infinite love and mercy despite my short-comings. To Him belong all glory and honor. I especially thank God for answering my prayer in bringing hope, life and health back to a colleague and friend who was ill and living in despair. Again and again, God has shown me the power of His grace. And as I was coming near to finish my dissertation, He has reminded me that His love for me is not dependent of my experiment results, or the number of papers I published, or the highest degree I earned. Thank God! I know that His grace is sufficient for me (2Cor12:8), so I continue to look forward to walking with Him on this journey He has set out for me.

God bless y'all!

VITA

Patrick Breckow Chu

June 20, 1970	Born, Hong Kong, Hong Kong.
1992	B.S., Electrical Engineering, Massachusetts Institute of Technology, Cambridge, Massachusetts.
1993 – 1994	Teaching Assistant, University of California, Los Angeles, California.
Summer 1993	Summer Intern, Ford Motor Company (Electronics Division), Dearborn, Michigan.
1994	Allied Signal Foundation Fellowship
1994	M.S., Electrical Engineering, University of California, Los Angeles, California.
1994 – 1995	RAND Fellowship
1995 – 1998	Research Assistant, University of California, Los Angeles, California.
1995 – 1997	Intern, Jet Propulsion Laboratory, Pasadena, California.

PUBLICATIONS

J. T. Butler, V. M. Bright, P. B. Chu, R. J. Saia
Adapting Multichip Module Foundries for MEMS Packaging,
Proceedings of the International Conference and Exhibition on Multichip Modules and High Density Packaging (MCM), 106-111(April 1998).

F. I. Chang, R. Yeh, G. Lin, P. B. Chu, E. Hoffman, E. J. J. Kruglick, K. S. J. Pister, M. H. Hecht,
Gas-phase silicon micromachining with xenon difluoride,
Proceedings of the SPIE - The International Society for Optical Engineering, **2641**, 117-128(1995).

P. B. Chu, J. T. Chen, R. Yeh, G. Lin, J. Huang, B.A. Warneke, K. S. J. Pister
Controlled Pulse Etching with Xenon Difluoride,
Proceedings of the International Solid-State Sensors and Actuators Conference - TRANSDUCERS '97, **1**, 665-8(June 1997).

P. B. Chu, N. R. Lo, E. C. Berg. and K. S. J. Pister
Optical Communication Link Using Micromachined Corner Cuber Reflectors,
Proceedings of the SPIE - The International Society for Optical Engineering, **3008**, 190-201(Feb 1997).

P. B. Chu, N. R. Lo, E. C. Berg. and K. S. J. Pister
Optical Communication Using Micro Corner Cuber Reflectors,
Proceedings of IEEE Tenth International Workshop on Micro Electromechanical System, 350-5(Jan 1997).

P. B. Chu, P. R. Nelson, M. L. Tachiki, K. S. J. Pister
Dynamics of polysilicon parallel-plate electrostatic actuators,
Sensors and Actuators A (Physical), **A52**, (no.1-3):216-20(Mar-Apr 1996).

P. B. Chu, P. R. Nelson, M. L. Tachiki, K. S. J. Pister
Dynamics of polysilicon parallel-plate electrostatic actuators,
Proceedings of the International Solid-State Sensors and Actuators Conference - TRANSDUCERS '95, **2**, 356-9(June 1995).

P. B. Chu, K. S. J. Pister
Analysis of closed-loop control of parallel-plate electrostatic microgrippers,
Proceedings of the 1994 IEEE International Conference on Robotics and Automation, **1**, 820-5(May 1994).

P. R. Nelson, P. B. Chu, K. S. J. Pister
Optical methods for characterization of MEMS device motion,
Proceedings of the SPIE - The International Society for Optical Engineering, **2640**, 53-7(1995).

ABSTRACT OF THE DISSERTATION

Optical Communication With Micromachined Corner Cube Reflectors

by

Patrick Breckow Chu

Doctor of Philosophy in Electrical Engineering

University of California, Los Angeles, 1998

Professor Kristofer S. J. Pister, Chair

Micromachined corner cube reflectors (CCRs) were demonstrated to transmit digital data optically across 150 meters indoors. These micro CCRs, made of gold-coated hinged polysilicon plates with dimensions of about $300\mu m$, had two fixed mirrors and one electrostatically actuated mirrors so that the CCRs could modulate incident light. Actuation voltages ranged from $15V$ to $37V$, with bandwidth ranging from $500Hz$ to $3kHz$ and angular motions of up to 3 degrees. Largest (best) mirror radius of curvature was about $20mrad$. Excellent mirror alignments was achieved using novel designs including tie-downs, tenon, and mortise. Divergence of reflected beams from typical CCRs was about $20mrad$.

These micro CCRs were fabricated by a commercial foundry using a polysilicon surface micromachining process. All the working devices were manually assembled. Self-assembled CCRs using scratch-drive actuators were also investigated and demonstrated to be viable option for batch assembly of CCRs.

By reflecting incident light from a $4.2mW$ interrogating laser, CCRs devices successfully demonstrated data transmission across 150 meters at 4bps, consuming $16nW$ for mirror actuation. Low data rate was limited by our commercial off-the-shelf hardware. The experimental results not only support our CCR communication analysis but also strongly suggest that low-power long-range communication (greater than $1km$) is achievable with suitable improvement of the CCRs' performance and the receiver system. Communication with multiple CCRs was also demonstrated, which suggests that CCRs can be used in applications requiring multiple communication channels. Small hand-held CCR-based communication units were also demonstrated.

Fabrication of micro CCRs using a commercial standard CMOS process was also investigated. A novel etching process using xenon difluoride (XeF_2) was developed to create hinged mirrors made of oxide, aluminum, and polysilicon by selectively etching away the supporting bulk silicon. Static corner cubes with dimensions of 200 to $250\mu m$ were fabricated. With appropriate design modifications, CMOS micro CCRs with actuators and monolithic electronics should be possible.

1 Introduction

1.1 Background

Wireless communication offers many advantages including flexibility, mobility, and often low-cost. Many options are currently available for implementing wireless communication using a large range of frequencies, including radio frequencies and optical frequencies. Propagation of electromagnetic waves in free space can be classified into 3 main categories: ground-wave propagation (below 2MHz), sky-wave propagation (2 to 30MHz) and line-of-sight (LOS) propagation(above 30MHz). Other propagation modes also exist. For example, tropospheric scattering may propagate waves $40MHz$ to $4GHz$ within 10 miles above the earth surface. [18] These options often offer a large range of data rate and communication distances, and various degrees of reliability and security. Table 1.1 shows examples of a variety of communication applications using different frequency bands. Depending on the applications, one frequency band may be more advantageous than another.

Optical LOS communication systems have some unique advantages and disadvantages compared to radio frequency (RF) systems. [27, 54] With smaller wavelengths, optical beams have smaller beam divergences leading to better directional resolution, high security with low probability of intercept, and higher ratio of received power to transmitted power. Large transmitter and receiver apertures are also not necessary, while larger bandwidth or data rate may be achieved. Optical systems can also exploit a large part of electromagnetic spectrum which is largely unused.

On the other hand, optical systems are less suitable for broadcasting because of narrow optical beams. Accurate pointing and line of sight are also needed.

Furthermore, generation efficiency for optical carriers is typically low, 10 to 20% for high-power gas lasers and up to 50% for semiconductor lasers.

An example of an optical communication system which deals with many issues common to optical systems is the following. A communication link uses a modulated infrared laser ($\lambda = 820nm$) to establish a telephony, video, or LAN connection across a distance of up to 1200 meters at a baud rate of up to 155Mbps for office buildings and for disaster recovery or rapid deployment across arbitrary terrain. [1] To achieve two-way long-range data transmission between two units, each unit is equipped with a 15mWatt laser and an optical detector. Each unit is relatively small and portable (about $0.4 \times 0.2 \times 0.2m^3$ in size), thus may potentially be used in many scenarios where line-of-sight is possible. Accurate, although not precise, alignment of the two units must be achieved so that the 2 meter diameter beam spot from one unit must rest on the $20cm$ aperture of the other unit. Although physical interruption of the line-of-sight link from flying devices like a kite or bird is unlikely, weather conditions may affect the performance of the system. For example, the bit-error-rate (BER) of 10^{-9} would increase significantly if visibility falls below 90% of the communication distance due to fog or rain. Another disadvantage is that this system consumes high power (30W at $115V_{ac}$) because of the laser. Thus further miniaturization of the transmitter is difficult.

Optical systems including the one presented above and RF systems used in many applications in Table 1.1 are extremely advantageous and suitable for many different applications. However, one common disadvantage which these systems all share is that the transmitter must generate electromagnetic waves for the receiver

[1] The companies which sell such communication equipments include Laser Communications, Inc., PA, U.S.A; SilCom Manufacturing Technology Inc., Ontario, Canada; and KMH Communications Ltd., Kent, U.K.

Frequency Band	Designation	Typical Uses
3-30kHz	VLF	long-range navigation; submarine
30-300kHz	LF	long-range navigation; marine radio beacons
300-3000kHz	MF	maritime radio, emergency, AM broadcasting
3-30MHz	HF	amateur radio, international broadcast, aircraft and ship, telephone, telegraph, facsimile
30-300MHz	VHF	television, FM 2-way radio, AM aircraft, aircraft navigational aide
0.3-3GHz	UHF	television, nav. aids, radar, microwave links
3-30GHz	SHF	satellite, radar microwave links
30-300GHz	EHF	Radar, satellite, experimental
$10^3 - 10^7$GHz	infrared visible, uv	Optical communication

Table 1.1: Selected applications of different frequency bands[18].

to detect. This requirement can be implemented in many applications, although the maximum operating time and range are often traded off for the low power consumption and the size of the device. If the transmitter is required to be small in size ($\ll 1cm^3$) and to consume low power ($\ll 1mW$), then the design becomes challenging, if not impossible, using standard design approach. Instead, suppose the transmitter can reflect external power for transmission. The operating time for the transmitter may be increased dramatically. The size of the transmitter may also be reduced significantly.

1.2 Using a corner cuber reflector to transmit data

1.2.1 Communication strategy

The proposed transmitter will use a micro corner cube reflector (CCR) whose shape can be modulated such that when a light beam is shined at the reflector, the reflector may either reflect the light back to its source or deflect it to some

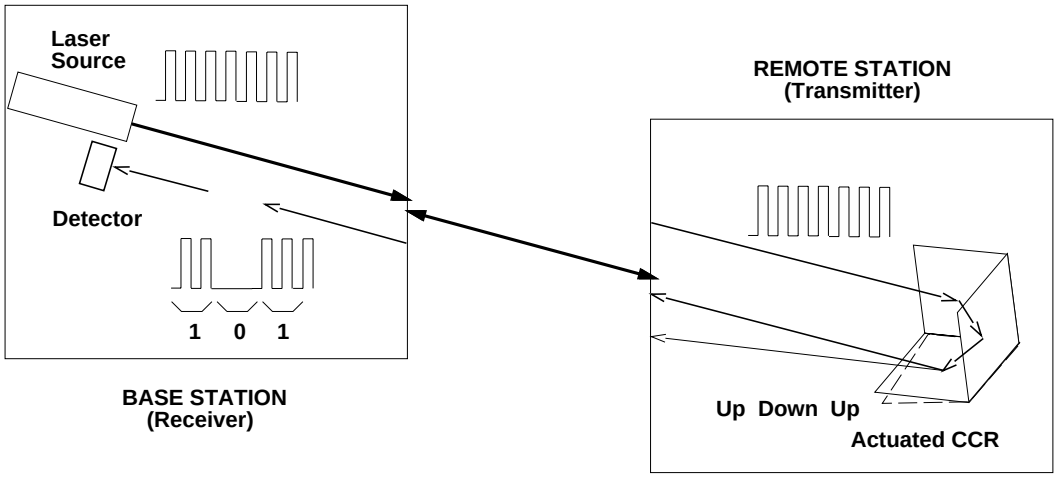

Figure 1.1: Schematic diagram of a uni-directional CCR communication link.

arbitrary direction. To communicate with a transmitter, a receiver will shine a laser at the corner cube reflector of the transmitter and detect the modulated laser from the reflector.

Fig. 1.1 shows a simple communication system which takes advantage of this communication strategy. A base station uses a laser to interrogate a remote station with a CCR transmitter and receives data from each remote station by detecting the modulated reflected light from the CCR. The base station may also receive data from other similar remote stations one after another or simultaneously depending on the detection scheme and the locations of the remote stations.

As shown in Fig. 1.1, the base station could only receive data from the remote station, and the remote station would transmit data to all interrogators. To exploit this "passive" communication strategy further, each remote station may be equipped with a photo detector as shown in Fig. 1.2. The interrogating laser may be modulated so that the remote station would transmit information only when

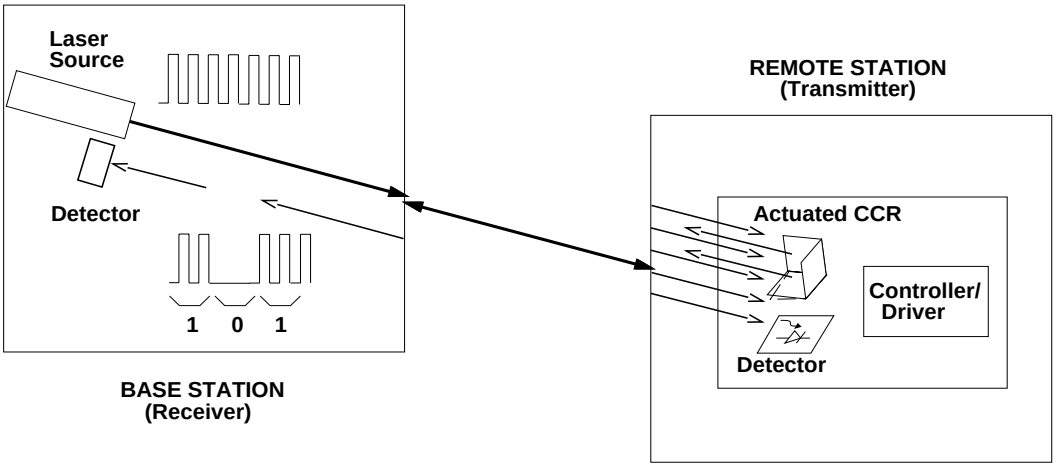

Figure 1.2: Schematic diagram of a bi-directional CCR communication link.

it is properly requested. With a detector at the remote station, two-way communication can be established between the remote stations and the base station, yet the high power burden still lies on the base station. In fact, it may be possible to power the remote station via the interrogating laser.

1.2.2 Benefits of using CCRs for communications

Using this transmission strategy, the remote stations will consume minimal power for data transmission: each remote station only needs to power the actuator which modulates the shape of the corner cube reflector. For small CCRs (less than a cubic millimeter), micro actuators with micro-Watt of power consumption will likely be sufficient. Obviously, the required size and number of the CCRs will depend on the percent of incident power to be reflected. Using MEMS technology, CCRs may be miniaturized and made in large volume, yielding low-power, small, and inexpensive transmitter devices. Tiny CCR devices may be added to many different remote systems with minimal or no degradation to their original functionalities.

On the other hand, even though the base station carries the disproportionally larger power burden compared to the remote stations, the requirements on the interrogating base station are not at all unreasonable. Optics, detectors, laser with high bandwidth, power, and efficiency are already commercially available. The base station may be reasonably simple and low-powered (proportional to the laser power consumption depending on the application) yet achieving low probability of interception and high spatial resolution using narrow laser beams. The short wavelengths of optical signals also allows the use of small transceiver aperture and components, yielding a portable interrogating system.

1.2.3 Applications and Implementation

Using macro-CCRs for low-orbit small satellite down-link has been proposed [44]. The use of macro-CCRs was also proposed for automobile communication and traffic control applications [94, 93]. While exploring Micro Electro-Mechanical Systems (MEMS) applications in military, Robert Zwirn and colleagues from RAND Corporation [7] proposed using micro CCRs for communication in a variety of applications. For example, distributed sensors on a battle field may use CCRs to transmit information of the environment conditions to an interrogating aircraft with a laser. CCRs may also be used for identification of friend or foe (IFF) where CCRs are mounted to surfaces of military vehicles or helmets of foot-soldiers to "broadcast" their identities to interrogating friends to prevent fratricide.

The proposed optical communication link may be implemented with many different technologies; however, MEMS technology is a suitable choice for several reasons. The overall size of the transmitter depends on the size of the corner cube reflectors and the size of the battery and power electronics required for the CCR

actuator. By reducing the size of the CCRs, the size of necessary battery and power electronics will also be reduced. In fact, with MEMS technology, it is possible to reduce the size of the whole transmitter unit to a volume of less than $1mm^3$, where other competing communication schemes cannot be easily implemented.

With batch-fabrication technology of MEMS, tens of thousands of CCRs could be fabricated on a single wafer so that the cost for each CCR transmitter may be dramatically reduced. Small and low-power CCRs would also allow simple system integration, using either macro or hybrid technology. In fact, monolithic systems with micro CCRs, MEMS sensors and battery may even be possible, thus creating a wireless, low-power, low-cost, and inconspicuous sensor and data network.

1.3 Issues to address

Many issues must be addressed in order to create a useful and reliable communication system based on corner cube reflectors. These issues can be divided into two areas: device and system.

The micro corner cube reflector must have good optical qualities such as high reflectivity and orthogonality so that high percentage of incident power will be returned. The method of optical modulation should have high bandwidth but low voltage and power requirements to yield high data rate and long operation duration. The device should be rugged and robust so that it would have wide application. At the same time, the mechanical design should be simple so that the device can be manufactured with a convenient process with high volume, high yield, and low cost.

Aside from device design and fabrication issues, we also need to consider system issues such as electronic integration and packaging of the devices, size, number, and

orientation of CCRs, selection of laser, signal detection method, and signal coding methods. The system design will affect the overall cost of implementation, communication distance, effectiveness, and reliability of the communication strategy. When these issues are properly addressed and test systems are thoroughly evaluated, we can then draw conclusions on viability of the proposed communication scheme.

1.4 Fabrication of micro structures through commercial foundries

Traditionally, fabrication of micro devices use customized processes since each design parameter must be carefully tailored to satisfy the necessary specification [76]. Unfortunately, in these situations, it is often difficult to transfer the designs to other people because not only the designs, but also the exact processes, must be imitated. Moreover, it is often difficult to integrate different designs together since each design has been made for a particular process.

On the other hand, standardized commercial fabrication processes allow simple technology transfer. In some cases, the electronics and mechanical devices may be fabricated in the same processes so that integration becomes automatic [73]. Standardized processes also have relatively low cost and reliable services. For example, MOSIS [2] and MCNC [3] are two brokerage services which respectively offer standardized complementary metal oxide semiconductor (CMOS) integrated circuit and polysilicon process services to the general public for a reasonable cost and turn-around time.

[2]MOSIS Foundry Service (www.mosis.org) is located in Marina DelRey, California.

[3]MCNC MEMS Technology Application Center (www.mcnc.org) is located in Research Triangle Park, North Carolina.

In general, post-processing of the chips from the commercial foundries is necessary to fabricate the final micro devices. Post processing steps may include wet or dry etching, such as oxide sacrificial etch with concentrated hydrofluoric acid (HF) [76] or HF vapor [59] for the MCNC polysilicon process and bulk silicon etch with ethylenediamine-pyrocatechol (EDP) [71], tetramethyl ammonium hydroxide (TMAH) [50], potassium hydroxide (KOH) [43], or xenon difluoride (XeF_2) [34, 10, 14] for standard CMOS processes. CMOS sacrificial oxide etching with buffered HF [33], reactive ion etch (RIE) [25], as well as sacrificial aluminum etching [75] has also been reported. Generally no masking step is needed for these post-process etches; however, in some cases, deposition and patterning of passivation layers may be necessary [43, 33]. An additional assembly process may also be necessary to form the final MEMS devices.

Standardized processes also have disadvantages. Many process parameters such as film thicknesses and stresses and minimum line width cannot be modified so that the design workspace is restricted, yielding designs which may not have optimal performance. For example, MOSIS's $2\mu m$ CMOS process via Orbit Semiconductor offers the possibility of monolithic integration of microstructures with electronics; however, fabrication of micro structures with fine features and low stress is rather difficult. On the other hand, MCNC's MUMPS (Multi-User MEMS Processes) with multiple polysilicon layers allows fabrication of complex mechanical structures and low-stress plates suitable for making optics; however, monolithic electronic integration is not possible. Analog Devices has developed an integrated surface-micromachining and CMOS process [17] which is now accessible through MCNC. The Integrated MEMS process (*i*MEMS) combines the Analog Devices' BICMOS IIe process with a single layer polysilicon MEMS process, allowing simple

fabrication of monolithic MEMS sensors. Unfortunately, a single layer of structural polysilicon is insufficient for our application. As a result, we could not take advantage of this combined process.

Our research focused on using the MCNC's MUMPS process which was modelled after a polysilicon surface micromachining process developed at University of California at Berkeley [37, 22]. The MUMPS process offers two layers of polysilicon for structural material and uses silicon dioxide as a sacrificial material. With only two structural layers, large out-of-plane structures with high aspect ratios can be created using plates hinged on the substrate via micro-hinges [77]. Several fixed and movable optical devices based on micro-hinges had been demonstrated including lenses [98, 63, 49], optical switches [58], and micro-optical bench [64]. The first development efforts of micro corner cube reflectors also used this standardized process [30, 31].

Numerous MEMS CMOS monolithic sensors have been demonstrated including vibration [53], thermal [6], pressure [74], infrared [60], muscle force [62] sensors. A monolithic sensor process is advantageous because it can reduce fabrication cost and avoid signal degradation due to packaging. Monolithic integration of some of these sensors with micro CCRs as low-power transmitters could be extremely useful for distributed sensing applications.

Although many integrated sensors were fabricated with the CMOS process [5], only a few CMOS-based MEMS optical devices with different designs of actuatable micro-mirrors had been reported. Various fabrication methods were used including unmasked EDP etching of the CMOS bulk silicon [70], unmasked XeF_2 etching followed by manual assembly [51], depositing and patterning polyimide

and aluminum followed by dry sacrificial etching of polyimide [89], and double-pass metalization of CMOS wafers followed by sacrificial etching of aluminum and oxide [8]. Although the latter two methods could yield high quality actuator and optics, substantial post-processing were necessary.

1.5 Previous work on micro corner cube reflectors

Previous micro CCRs based on the MUMPS surface micromachining technology had been reported [30, 31]. These CCRs used two hinged polysilicon plates and a horizontal plate supported by torsional beams to form an electrostatically modulated retroreflector. The 100 to 200μm sized CCRs could be actuated with as low as 5 volts with a bandwidth of as high as 11kHz and had 1 to 2% reflectivity. However, there are a number of critical issues which were not addressed.

Fabricated CCRs had poor orthogonality such that 6 reflections were observed from a CCR. In other words, the fabricated devices actually did not operate as retroreflectors because the devices could not change the incident light direction by 180 degrees as an ideal CCR would. Fabricated mirrors also had relatively low reflectivity (24%) with substantial diffraction patterns due to rough mirror surface profile. Mirror alignment and optical quality needed to be improved in order to use these micro CCRs for communication. These previous CCRs were also known to have low fabrication yield. Low fabrication yield was often due to stiction which caused the large suspended mirror to be stuck to the substrate. Requirement of manual assembly also affected the yield. Because of these various issues, the fabricated devices could not be use to demonstrate wireless micro CCR communication.

1.6 Overview of this research

In this work, we studied the feasibility of using micro corner cube reflectors for communication (Chapter 2). Based on a detector noise analysis, we showed that a carefully designed CCR-based communication link can achieved respectable SNR for a communication distance of a 1 kilometer and beyond.

We have successfully designed and fabricated micro corner cube reflectors using a standardized process of a commercial foundry, MCNC's MUMPS process (Chapter 3). These micro CCRs have dimensions of about $300\mu m$ and can modulate incident light with about $20V$ at kilo-Hertz of frequency. Manual as well as self-assembled CCRs were designed and fabricated.

We also demonstrated that corner cube reflectors can indeed serve as wireless optical transmitters by transmitting data with CCRs across a distance of 150 meters (Chapter 4). We designed a portable interrogating system which included a $4.2mW$ laser diode module, a small telescope, and a laptop computer with image processing capabilities to demonstrate simultaneous communication with multiple CCRs.

Finally, we also successfully fabricated static micro CCRs using a standard CMOS process (Orbit $2\mu m$) and a post-process dry etch with xenon difluoride, XeF_2 (Chapter 5).

2 Analysis of Corner Cube Reflectors

2.1 Operation of an ideal CCR

2.1.1 Basic operation of a CCR

An ideal corner cube reflector (CCR) has 3 perfectly reflective, mutually orthogonal planar surfaces, together forming a right angle concave corner. Because of its mirror configuration, a corner cube reflector has the unique ability to reflect any incident light ray back to its source, similar to a flat mirror reflecting a normal light ray to its source. While a flat mirror may reflect light from a hemisphere of directions, a CCR is only responsive to light coming from a quadrant of a hemisphere defined by the concave side of the CCR.

Given a Cartesian coordinate system, it can be shown that an incident ray with direction $\hat{a} = (-a_x, -a_y, -a_z)$,with $\|\hat{a}\| = 1$ and $a_x, a_y, a_z \geq 0$, will be reflected back to the direction -$\hat{a}$ after it hits three mirror surfaces of the CCR (Fig. 2.1) [79, 84]. The light ray may also return to its source after two bounces or even one bounce if the appropriate component of the incident direction is zero. In this application, we are most interested in the three bounce case because it is most likely that the incident light has a direction with non-zero a_i. In the following paragraphs, we will provide an intuitive explanation of how a CCR reflects light based on the law of reflection.

Suppose an incident ray with direction $\hat{a} = (-a_x, -a_y, -a_z)$ struck the x-y mirror at $p_1 = (x_1, y_1, 0)$, and then the x-z mirror and the y-z mirror at $p_2 = (x_2, 0, z_2)$ and $p_3 = (0, y_3, z_3)$ respectively (Fig. 2.1). Note that one of the three components of the direction of the incident ray changes sign after each reflection

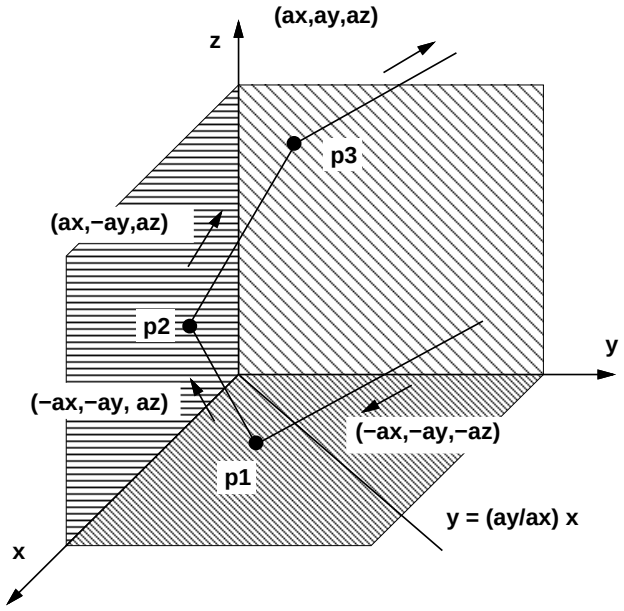

Figure 2.1: This figure shows how the direction of an incident ray changes after hitting each mirror. Note that three successive reflections are not always possible depending on $p1$ and a_i's.

so that after three reflections, the light ray has a direction equal to -$\hat{a}$. One way to understand the sign change is to consider the two dimensional case as shown in Fig. 2.2.

The law of reflection requires that the reflected ray must lie in the same plane (the plane of incidence) as the incident ray and the normal. Furthermore, the angle of incidence, θ_1, must be equal to the angle of reflection, θ_1'. In the 2-dimensional case where the y-axis is the mirror, the plane of incidence is the y-z plane. Intuitively, the first requirement of the law of reflection is immediately satisfied since the x-components of all the rays are always 0. Based on geometry, the second requirement of the law is satisfied as long as the y and z components of the incident ray remains constant in magnitude and the z-component changes sign.

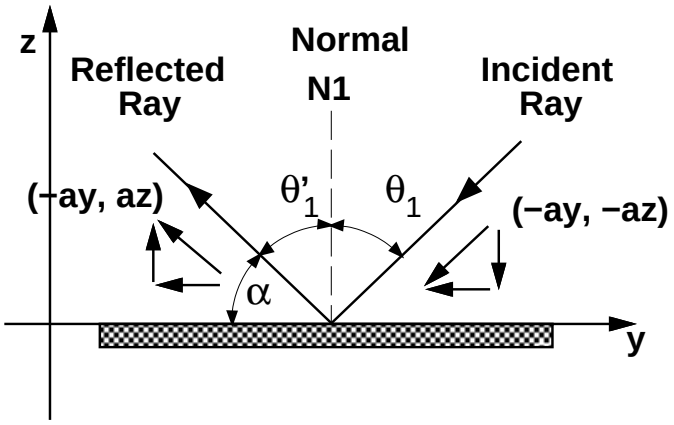

Figure 2.2: This illustration shows that for θ_1 and θ_1' to be equal, the incident and reflected rays must have the same direction components except for one sign difference.

In the 3-dimensional case where the x-y plane is the mirror, a non-zero x-component of the incident direction merely causes the plane of incidence to rotate from the y-z plane. Since the incident and reflected rays both lie in the same plane (the plane of incidence), the x and y components of the light ray must remain unchanged. Furthermore, the z-component must remain constant in magnitude and change in sign just the same as in the 2-dimensional case.

This argument can be applied to the cases where the x-z and y-z planes become the mirror surface. Each reflection will cause one component of the incident ray to change sign. As a result, after 3 reflections, the incident ray to the CCR with direction $-\hat{a}$ becomes $\hat{a}$ and is reflected back to its source. It is also important to note that if the incident beam is smaller than the dimension of the mirrors, an ideal CCR will only change the direction of the incident beam by 180^o but will have no effect on the amplitude or phase of the incident beam.

2.1.2 Estimation of effective area for CCRs

For an ideal macro corner cube which the cube size is much larger than the incident beam size, direction of the incident ray (or the orientation of the CCR) is generally not a concern because retro-reflection is easily achieved as long as the incident ray is aimed near the center of the CCR. After 3 reflections, 100% of the incident power is returned. On the other hand, for micro CCRs which are generally smaller in size than the incoming beam, the incident ray direction is important because it directly affects the size of the total effective area of the CCR, which, in turns, affects the power reflected by the CCR.

In the three dimensional illustration in Fig. 2.1, we have shown how three successive reflections may occur. Intuitively, we can see that if p_1 is close to the origin, so will p_2 and p_3 such that the incident ray will be reflected to its source. We can also imagine that three successive reflections are not always possible for all arbitrary incident rays. We would like to know where p_1 must lie in order to achieve a perfect reflection to the source. The result will clearly depend on the direction of the incident ray.

Suppose we require that p_2 and p_3 must lie on the shaded areas on the x-z and y-z planes respectively as shown in Fig. 2.1. The following conditions can be derived for p_1 in terms of a_i's for the case where $a_y/a_x \leq 1$:

$$0 < y_1 < \frac{a_y}{a_z} < 1 \text{ and } 0 < x_1 < \frac{a_x}{a_z} < 1 \tag{2.1}$$

and

$$0 < y_1 < \frac{a_y}{a_x} x_1 < 1 \tag{2.2}$$

for all $a_i > 0$. For $a_y/a_x > 1$, the following condition also applies:

$$0 < \frac{a_y}{a_x} x_1 - 1 < y_1 \tag{2.3}$$

Similar conditions can be derived for the case where the light ray first hits the x-y mirror, followed by the y-z mirror and then x-z mirror. Eq. 2.1 still holds true. Furthermore, if $a_y/a_x \geq 1$, then

$$0 < \frac{a_y}{a_x} x_1 < y_1 < 1 \tag{2.4}$$

If $a_y/a_x < 1$, the following condition also applies:

$$y_1 < (\frac{a_y}{a_x} x_1 + \frac{a_y}{a_x}) < 1 \tag{2.5}$$

From the analysis above, we see that an incident ray which strikes the x-y mirror would get 2 additional reflections only if it hits a specific region of the x-y mirror. The exact return path also depends on the starting location and direction of the incident ray. By considering the six different possible cases based on the variation of relative magnitudes of a_x, a_y, and a_z, we can construct six scenarios where only part of the x-y mirror is "reflective." Fig. 2.3 shows different areas for the six cases. The shaded area in the x-y mirror represents the area where the incident ray must hit to achieve 3 successive reflections.

Table 2.1 shows the expression for the area of each effective surface for the six cases. Since three of the shaded areas are actually just mirror reflections of the other three areas in Fig. 2.3, the six expressions only have three distinctly different forms. Note that the expressions assume that the CCR is a unit cube. If the cube has a length x, then the expression must be scaled by x^2.

To determine the overall effective reflective surfaces of cube, we apply the analysis to the other two mirrors of the corner cube. We find that there are basically two

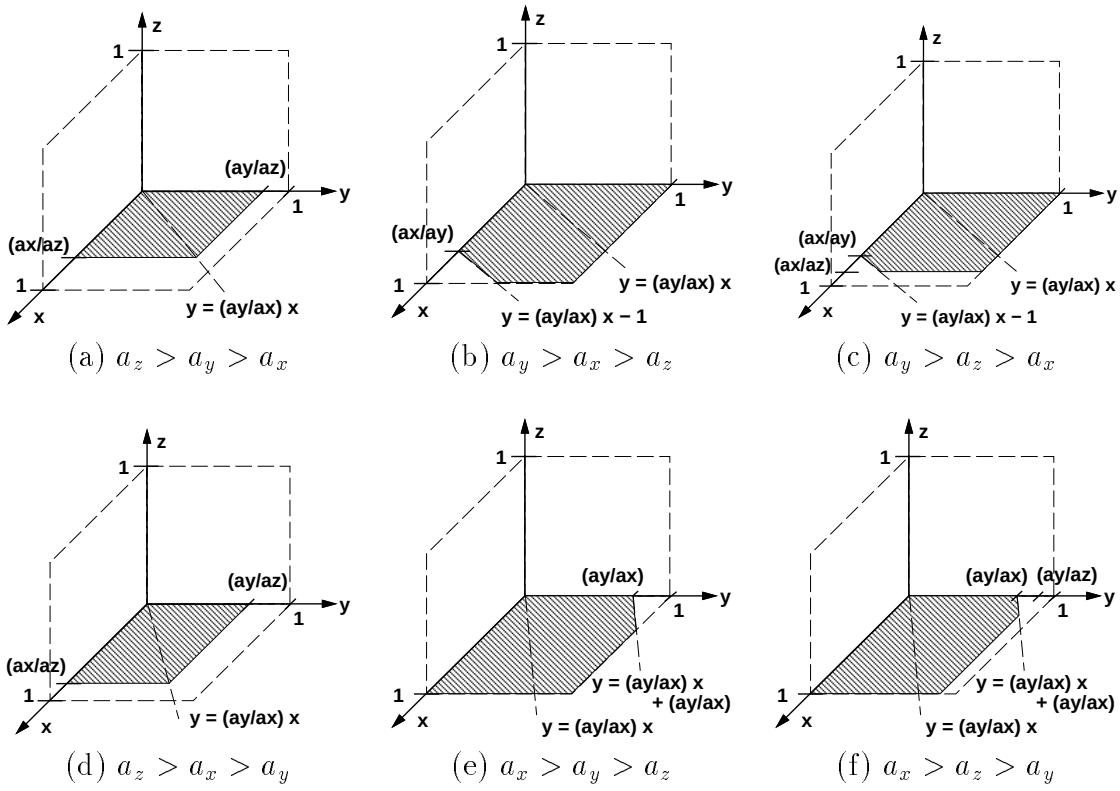

Figure 2.3: Given an incident ray with direction $\hat{a} = -(a_x, a_y, a_z)$, $\|\hat{a}\| = 1$ and $a_x, a_y, a_z > 0$. The shading represents the area of the x-y mirror where the light ray must first strike in order to be reflected to $-\hat{a}$.

distinct cases as shown in Fig. 2.4. Similar to the previous figures, the shaded areas in these figures represents the regions on the cube where the incident ray must first hit in order to achieve three reflections and be reflected to the source. Although Fig. 2.4 describes specifically the cases where $a_z > a_y > a_x$ and $a_z > a_x > a_y$, the other cases can also be visualized by rotating the coordinate system.

The area of the shaded area of each mirror, A_{ij}, can be calculated using the equations in Table 2.1 with a proper change of variables. The total effective area, A_{eff}, of the corner cube is the sum of the shaded "reflective" area of each mirror, A_{ij}, scaled by the corresponding direction cosine of the incident ray. A_{eff} is given

	Condition	Effective Mirror Surface (A_{xy})
A.	$a_z > a_y > a_x$	$\frac{a_x \cdot a_y}{{a_z}^2}$
B.	$a_y > a_x > a_z$	$1 - \frac{1}{2}(1 - \frac{a_x}{a_y})(\frac{a_y}{a_x} - 1)$
C.	$a_y > a_z > a_x$	$\frac{a_x}{a_z} - \frac{1}{2}(\frac{a_x}{a_z} - \frac{a_x}{a_y})(\frac{a_y}{a_z} - 1)$
D.	$a_z > a_x > a_y$	$\frac{a_x \cdot a_y}{{a_z}^2}$
E.	$a_x > a_y > a_z$	$1 - \frac{1}{2}(1 - \frac{a_y}{a_x})(\frac{a_x}{a_y} - 1)$
F.	$a_x > a_z > a_y$	$\frac{a_y}{a_z} - \frac{1}{2}(\frac{a_y}{a_z} - \frac{a_y}{a_x})(\frac{a_x}{a_z} - 1)$

Table 2.1: This table shows the expression of the effective area of the $x - y$ mirror of a unit CCR for an incident ray with direction $\hat{a} = (-a_x, -a_y, -a_z)$, $\|\hat{a}\| = 1$ and $a_x, a_y, a_z > 0$. The geometry of each area is shown in Fig. 2.3.

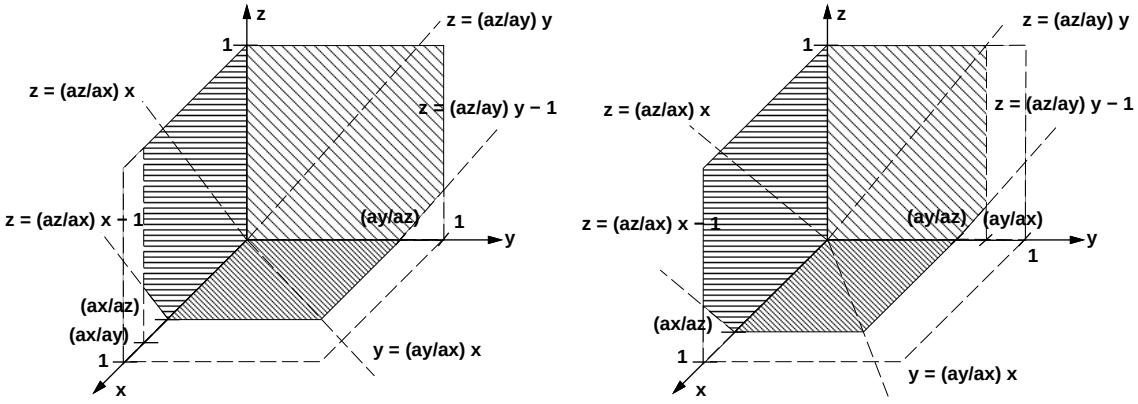

(a) $a_z > a_y > a_x$ (b) $a_z > a_x > a_y$

Figure 2.4: Effective surfaces of the CCR for an incident ray with direction $\hat{a} = (-a_x, -a_y, -a_z)$, $\|\hat{a}\| = 1$ and $a_x, a_y, a_z > 0$. The shading represents areas where the light ray must first strike in order to be reflected to $-\hat{a}$ where (a) $a_z > a_y > a_x$ and (b) $a_z > a_x > a_y$.

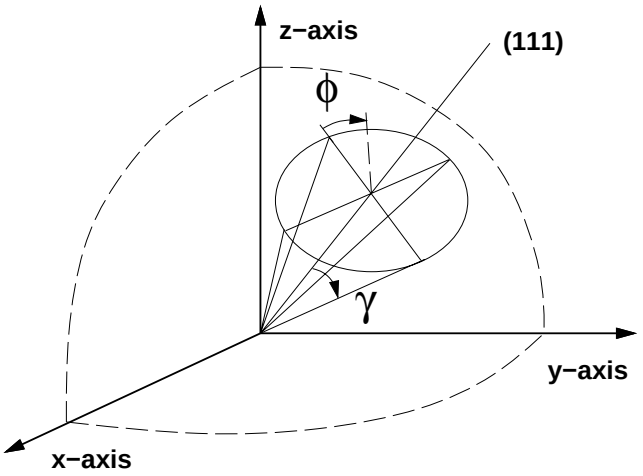

Figure 2.5: Several sets of incident rays were used for the CCR effective area simulation. For each set, γ is fixed and ϕ changes from 0 to 2π. Each set of incident rays forms a cone in space centered around the (111) axis.

by the following expression:

$$A_{eff} = [A_{xy}, A_{xz}, A_{yz}] \cdot \hat{a} \tag{2.6}$$

The maximum effective area for a unit corner cube, thus, is $\sqrt{3}$. The direction which yields the largest effective area is $-\frac{1}{\sqrt{3}}(1,1,1)$.

In order to better understand how the CCR effective area changes with respect to the directions of incident rays, we simulated the effective areas for incident rays which are deviated from the (1,1,1) direction by some fixed angles. For each angle, a set of incident rays traces a cone in space whose axis coincides with the line $(x,y,z) = t \cdot (1,1,1)$ as shown in Fig. 2.5.

For presentation purposes, we will describe the incident rays directions based on a spherical coordinate system using γ and ϕ as shown in Fig. 2.5. γ is defined to be the angle between the (1,1,1) direction and the incident ray, $\gamma \geq 0$. ϕ is used to describe where each of the set of incident rays lies on the cone in space, $0 \leq \phi \leq 2\pi$. The simulated effective areas as a function of γ and ϕ are plotted

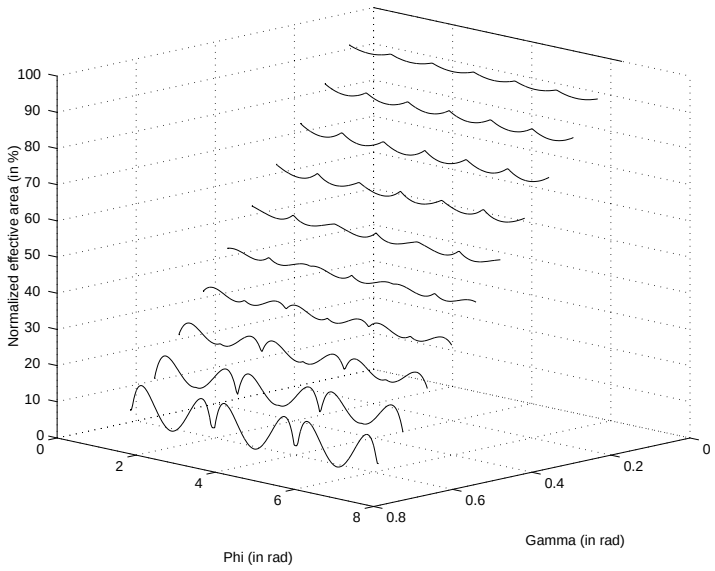

Figure 2.6: Effective surface area of a unit CCR for sets of incident rays where each set of rays are deviated from -(1,1,1) by a fixed angle γ as shown in Fig. 2.5. The value of each area is normalized by the maximum area of $\sqrt{3}$.

in Fig. 2.6, Fig. 2.7 and Fig. 2.8. Each area is presented as a percentage of the maximum area ($\sqrt{3}$).

Each curve in Fig. 2.6 and Fig. 2.7 corresponds to a set of incident rays with a fixed value of γ. Each curve is found to be periodic with a period of $2\pi/3$ due to the symmetry of the 3-mirror CCR. With incremental increase in angle deviation of about 0.0615 radian (3.5 degrees), the effective area is decreased by about 10% for each angle increase (Fig. 2.7). A CCR is most responsive to incident rays which are small deviation from -(1, 1, 1) direction. The effective area reduces to 50% of maximum when the angle deviation is increased to about 0.3rad and reduces to less than 10% when the angle deviation is about 0.6rad (Fig. 2.7).

The lowest curve in Fig. 2.6 and in Fig. 2.7 corresponds to a γ of about 0.615 radian (35 degrees). The simulation shows that for 3 rays, the effective area goes

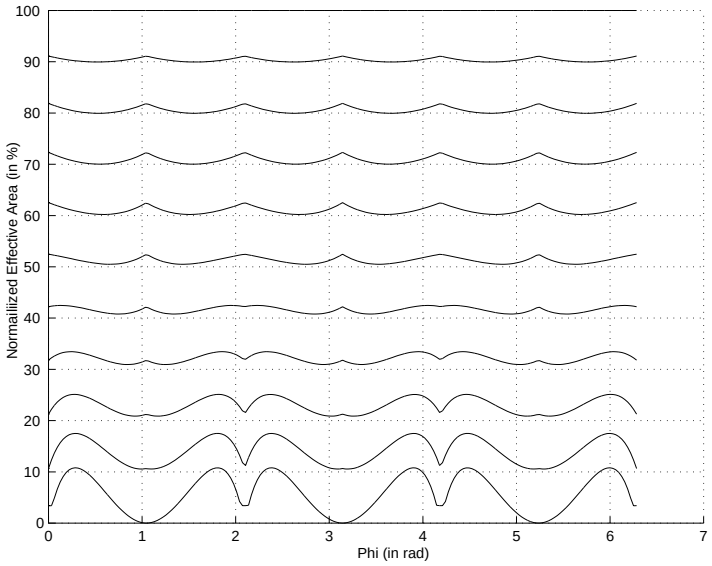

Figure 2.7: A 2-D plot of the simulated effective areas as a function of ϕ for fixed values γ vary from 0 to 0.615rad. The simulation shows that for every additional 3.5 degrees an incident ray is deviated from the -(1,1,1) direction, the effective area is decreased by about 10%.

to zero at $\phi = \pi/6$ or $\pi/2$ or $5\pi/6$. These 3 rays correspond to light rays which are parallel to the diagonal of one of the mirrors ($x = y$, $x = z$, or $y = z$) so that 3-bounce reflection is no longer possible. At this special angle, specifically $\arctan(1/\sqrt{2})$, the incident light, in reality, will be returned after 2 reflections, and the effective area becomes $\sqrt{2}$, instead of zero as shown in Fig. 2.7. 2-bounce reflections are ignored in our simulation.

The other 3 non-zero local minimum at $\phi = 0\pi/3$ or $2\pi/3$ corresponds to light rays whose directions are approaching the X, Y, and Z-axes. The effective area for these rays will eventually go to zero according to the 3-bounce analysis; however, the effective area will be equal to 1 at the limit when $\gamma = \arctan(\sqrt{2})$, where the light ray is reflected back after just 1 reflection. As we suggested earlier, these special cases (1 bounce or 2 bounces) are negligible subsets of the incident rays.

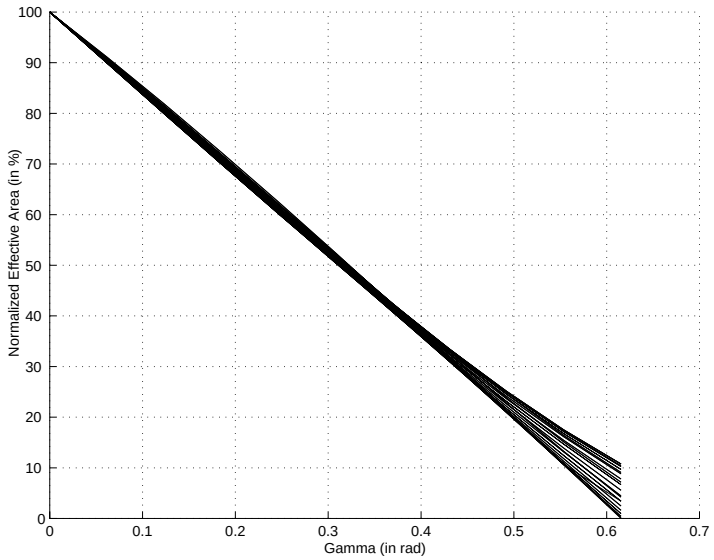

Figure 2.8: A 2-D plot of the simulated CCR effective areas as a function of the angle deviation from the (1,1,1) direction, γ, for various values of ϕ. The relationship between the area and γ is near linear.

In Fig. 2.8, the simulated CCR effective areas are plotted as a function of the angle deviation from the (1,1,1) direction, γ, for various values of ϕ. The simulated result shows that the effective area decreases nearly linearly as γ increases, although it is also clearly dependent on ϕ as shown in Fig. 2.6 and Fig. 2.7, especially when γ is large.

In conclusion, we have shown that the effective area of a CCR is strongly affected by the incident light direction. A CCR has the largest area for incident light from the -(1,1,1) direction, and the effective area graduately decreases (almost linearly) as the incident light moves away from the (-1,1,1) direction. The area is non-zero as long as the incident light is within a solid angle of $\arctan(1/\sqrt{2})$ radian (0.615 rad) from -(1,1,1).

These results are important because the percent of incident power reflected

by a CCR is directly proportional to the effective area of the CCR. In order to reflect sufficient power from interrogating light sources from arbitrary directions, multiple micro CCRs with various orientations will be necessary to build a robust communication system. A rough estimate suggests that about 15 CCRs with the proper orientations would guarantee that the reflected power for an interrogating beam from any arbitrary direction in a hemisphere will be as least 50% of the maximum reflected power of a single CCR. The exact required number of CCRs would depend on the exact coverage and response requirements of communication unit.

2.2 Operation of a non-ideal CCR

A fabricated macro or micro CCR are likely to operate differently from an ideal CCR as described in the previous section. Inaccurate mirror alignment and mirror curvature would certainly affect the operation of a CCR. Mirror material, surface defect, and aperture effects would further complicate the analysis of the optical response of a CCR. In this section, we will briefly address some of these non-ideality.

2.2.1 A misaligned CCR

Consider the case where a CCR has optically perfect mirrors, but only two of the mirrors are orthogonal and one of the mirrors is misaligned. Fig. 2.9 shows a corner cube whose x-y mirror is rotated away from the x-y plane about the x-axis by an angle δ. We would like to know how the misalignment affects the direction of the reflected light ray.

We will first consider the two dimensional case as shown in Fig. 2.10, which is

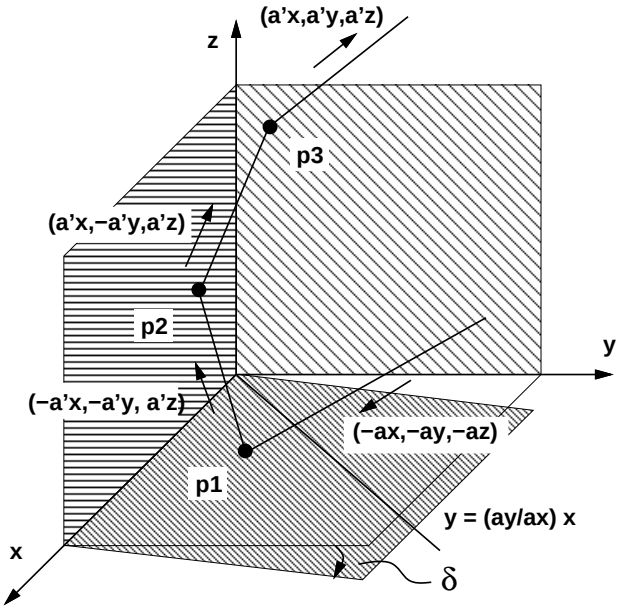

Figure 2.9: This figure shows how the direction of an incident ray changes after hitting the 3 mirrors of a CCR whose based mirror is tilted by an angle δ.

similar to Fig. 2.2 but has a the tilted mirror. N_2, instead of N_1, is the normal of the tilted mirror. As a result, the angles of incidence and reflection become θ_2 and θ_2' respectively. Since θ_2 and θ_2' are equal, it can be shown that the angle between the reflected ray and the y-axis becomes $\alpha + 2\delta$ instead of just α. In other words, the reflected light ray from a tilted mirror compared to that from a straight mirror differs in direction by twice the angle of the tilt.

By geometry, we can also see that the direction of the incident ray, $(-a_y, -a_z)$, and that of the reflected ray, (-a_y', a_z'), are not just different by a simple sign as in the case of Fig. 2.2. The components of the direction of the reflected ray is defined by the following:

$$\begin{bmatrix} a_y' \\ a_z' \end{bmatrix} = \begin{bmatrix} \cos(2\delta) & -\sin(2\delta) \\ \sin(2\delta) & \cos(2\delta) \end{bmatrix} \begin{bmatrix} a_y \\ a_z \end{bmatrix} \tag{2.7}$$

Therefore, for small δ, the relationship between the incident and reflected rays

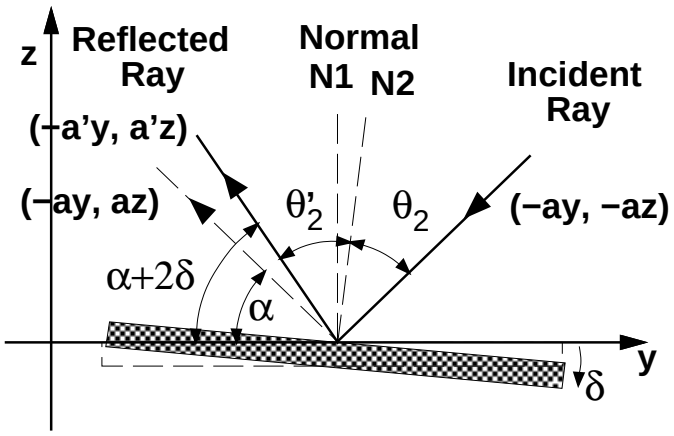

Figure 2.10: This illustration shows that in 2-D, the reflected ray from the tilted mirror deviates from the reflected ray from a non-tilted mirror by twice the tilt angle.

becomes

$$\begin{aligned} a'_y &= a_y - 2\delta a_z \\ a'_z &= a_z + 2\delta a_y \end{aligned} \tag{2.8}$$

Now consider the three-dimensional case as shown in Fig. 2.9. Given an incident ray hitting the x-y mirror with a direction $\hat{a} = -(a_x, a_y, a_z)$ where $\|\hat{a}\| = 1$ and $a_x, a_y, a_z > 0$, we define the direction of the ray reflected by the tilted x-y mirror as $(-a'_x, -a'_y, a'_z)$. The magnitude of direction cosines for this ray is given by the following:

$$\begin{bmatrix} a'_x \\ a'_y \\ a'_z \end{bmatrix} = \begin{bmatrix} 1 & 0 & 0 \\ 0 & \cos(2\delta) & -\sin(2\delta) \\ 0 & \sin(2\delta) & \cos(2\delta) \end{bmatrix} \begin{bmatrix} a_x \\ a_y \\ a_z \end{bmatrix} \tag{2.9}$$

Since the x-z mirror and the y-z mirror are orthogonal and are aligned to the coordinate system, the subsequent reflections will only change the sign of direction cosine as described in Sect. 2.1.1. The final direction for the incident ray $-(a_x, a_y, a_z)$

after three reflections is (a'_x, a'_y, a'_z) following the path shown in Fig. 2.9 and is also defined by Eq. 2.9. For small δ, the reflected ray will have a direction of $(a_x, a_y - 2\delta a_z, a_z + 2\delta a_y)$. However, unlike the 2-dimensional case in Fig. 2.10, the reflected light ray from the misaligned CCR compared to that from a perfect CCR does not differ in direction by exactly twice the tilt angle. The exact angle deviation, γ, can be calculated by using the dot product relationship:

$$(a_x, a_y, a_z) \bullet (a'_x, a'_y, a'_z) = \cos(\gamma) \tag{2.10}$$

The result is the following:

$$\gamma = \cos^{-1}\left({a_x}^2 + ({a_y}^2 + {a_z}^2)\cos(2\delta)\right) \tag{2.11}$$

Similar results can be obtained for cases where the incident ray travels a different path as the one shown in Fig. 2.9, such as a path which starts at the x-z or the y-z mirror instead of the x-y mirror. For the 6 different possible paths, there are actually only 2 different possible directions for the incident ray after 3 reflections. In other words, if one of the 3 mirrors is misaligned as in the case of Fig. 2.9, one large incident beam which covers the whole CCR will generate two different reflected beams. Both of these beams will be deviated from the source direction by γ defined in Eq. 2.11. One of the possible reflected beam directions was also given in Eq. 2.9. The second possible direction is given by the following:

$$\begin{bmatrix} a'_x \\ a'_y \\ a'_z \end{bmatrix} = \begin{bmatrix} 1 & 0 & 0 \\ 0 & \cos(2\delta) & \sin(2\delta) \\ 0 & -\sin(2\delta) & \cos(2\delta) \end{bmatrix} \begin{bmatrix} a_x \\ a_y \\ a_z \end{bmatrix} \tag{2.12}$$

The two direction expressions in Eq. 2.9 and Eq. 2.12 are different only in the signs of the sine terms in the matrices. (Reflected beams from a single or double mirror

reflections are not taken into considerations here; however, the same analysis may be used to determine the directions of these beams.)

Using this analysis, we can also show that the CCR will reflect 6 different beams if none of its mirrors are aligned (orthogonal) to each other. The exact expression for each reflected beam as a function of tilt angles and incident ray direction may be obtained by first identifying the transformation matrix for each tilted mirror and then multiplying the incident ray direction by the 3 transformation matrices. The cumbersome result is omitted here since it is not too informative.

From the analysis above, we can conclude that only one mirror alignment is sufficient to cause a CCR not to reflect light properly. This optical property of CCRs implies that precise mirror alignment is a critical requirement for fabricating CCRs. Fortunately, since a reflected light beam will have a measurable divergence θ_{CCR}, some amount of light will be reflected to its source as long as the tilted angle δ is small enough. Shown in Fig. 2.11 are illustrations of light beams reflecting from an illuminated CCR.

We assume that the interrogating light is located at the detector as shown. If the CCR alignment is perfect, the reflected beam will have an axis centered along the direction of the incident interrogating light (Fig 2.11(a)). If the CCR mirrors has a small misalignment, where $\gamma < \theta_{CCR}$, only a fraction of the light will (Fig 2.11(b)). For $\gamma > \gamma^* = \theta_{CCR}$, which corresponds to tilt angles $\delta > \delta^*$ according to Eq. 2.11, no light will be reflected along the same axis as the incident interrogating light (Fig. 2.11(c)).

Because γ^* is a function of the direction cosines of the incident ray (Eq. 2.11), it is hard to get a meaningful value for δ^*. Nevertheless, suppose the direction of the incident ray is -(1,1,1) and the half-angle divergence of the CCR, θ_{CCR}, is

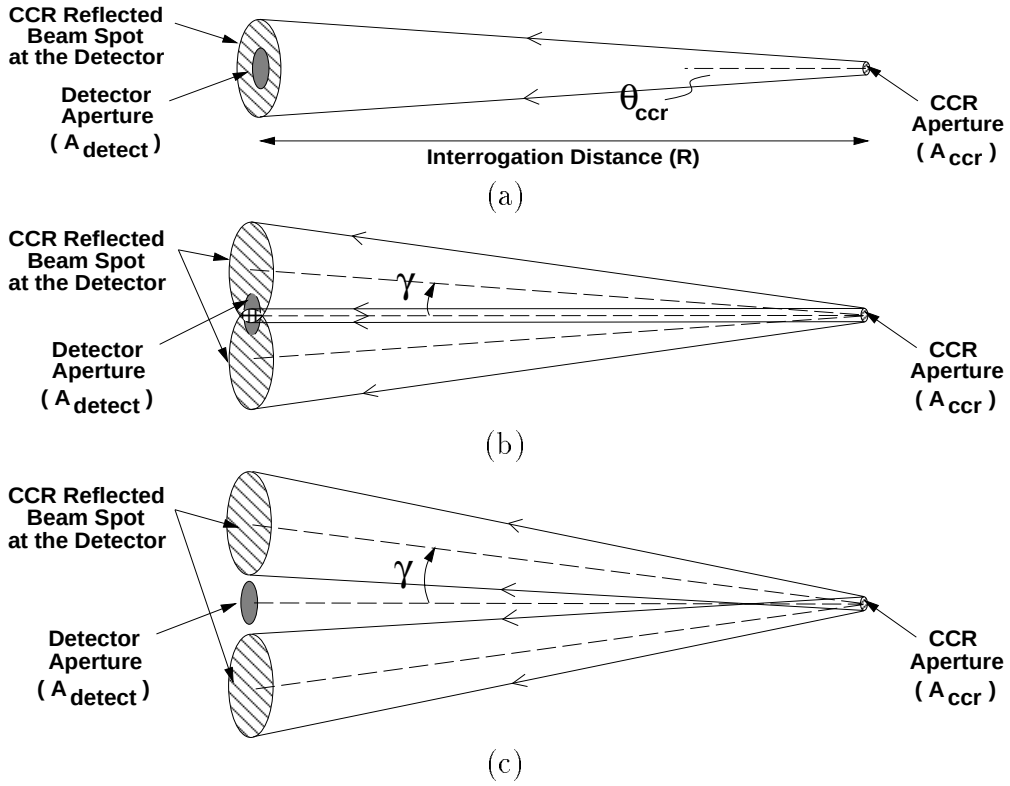

Figure 2.11: Illustrations of CCR reflected beams for different CCR mirror alignments are shown. We assume that the CCR is interrogated by a laser at the detector. In (a), the CCR has perfect alignment and it reflects the incident light to the detector as a narrow beam. In (b), the misalignment is small so that some light is still returned to the direction of the interrogator. In (c), the CCR has poor alignment and it reflects the incident light as two beams, but both are missing the detector.

$5mrad$, then δ^* is about $3.06mrad$. On the other hand, if θ_{CCR} is $20mrad$, then δ^* is about $12.2mrad$.

Although Fig. 2.11 shows that a CCR having a misalignment of $\gamma < \gamma^*$ (or $\delta < \delta^*$) still could reflect light to the direction of the incident interrogating light, it is important to realize that the CCR is not necessarily functional for our communication application. The reason is that the returned power may simply be too low for the application required. As shown in Fig. 2.11, only a small fraction of

the light beam shown in Fig. 2.11(b) will actually reach the original light source, where the detector is located. Good alignment is particularly important if θ_{CCR} is large because the signal-to-noise of the reflected signal is inversely proportional to the square of θ_{CCR} as shown in the following section.

We can also take advantage of this optical alignment property of the CCR. We can use a CCR to modulate the incident light by simply making one of the mirrors of the CCR to become misaligned by a small angle. Suppose a CCR is illuminated by a light source at a distance R and a detector with an aperture radius R_{detect} at the light source is used to detect the modulated light from the CCR (Fig. 2.11). For the detector to see maximum optical modulation from the CCR, the CCR must tilt its mirror enough so that the reflected beams would completely miss the detector aperture. The minimum tilted angle, δ^*, will depend on the size of the detector aperture at the interrogating light source, the interrogating distance, as well as the divergence of the reflected light beam. δ^* should be selected such that

$$\gamma^* = \frac{R_{detect}}{R} + \theta_{CCR}. \tag{2.13}$$

The relationship between δ^* and γ are defined by Eq. 2.11. Suppose the direction of the incident ray is -(1,1,1), R is $100m$, R_{detect} is $10cm$, and θ_{CCR} is $5mrad$, then δ^* is about $3.67mrad$. On the other hand, if θ_{CCR} is $20mrad$, then δ^* is about $12.9mrad$. These δ^* values are slightly larger than the δ^* values we computed earlier when we neglected the detector aperture size. For $R >> R_{detect}$, setting γ^* equal to θ_{CCR} would give a fair approximation for δ^*.

2.2.2 Real mirrors

There are many physical phenomena which make a fabricated mirror behave differently from an ideal mirror. For example, surface roughness and coating of a real

mirror would certainly affect the mirror's optical response and thus the overall response of the CCR. Mirror curvature and mirror size would further complicate the response of the CCR. In this section, we will briefly describe these issues.

Reflectivity is generally used to describe the ratio of the reflected to the incident intensity of light striking a perfectly smooth and flat surface between two homogenous media. Since a fabricated mirror would contain imperfections, we are interested in the *reflectance* of the mirror, an equivalent measure which describes the ratio for less idealized materials.

Reflectance may be separated into diffused and specular components. A perfectly diffuse plane reflector would reflect light in all directions (of a hemisphere) regardless of the angle of incidence but follow the Lambert's law,

$$I_d(\theta) = I_0 \cos\theta, \tag{2.14}$$

where I_0 is the total amount of light reflected per unit area normal to the plane and I_d is the reflected light per unit area at angle θ to the normal. The reflectance of a mirror would be mostly diffused if the mirror roughness is in the order of a wavelength or more. On the other hand, if the roughness is small compared to the wavelength, the reflection would be specular, where the angle of incidence and the angle of reflection are equal. We have made this assumption for the analysis in the previous sections of this chapter.

To fabricate a corner cube reflector, we would obviously need to use mirrors with high specular reflections. The specular reflectance of a mirror is found to be sensitive to the ratio of surface irregularity and wavelength. Specular reflectance, R_s, is defined in the following equation:

$$R_s = R_0 \; e^{(-4\pi h/\lambda)^2} \tag{2.15}$$

when R_0 is the total reflectance of the surface, h the rms height of the mirror surface, and λ the wavelength. The reflectance of a mirror obviously also depends on the mirror coating material.

For bare polysilicon plates, the reported reflectance is 24% for 0.67μm wavelength [31]. Unfortunately, the effective reflectance of a CCR with 3 mirrors would only be to ($24\%^3$) or 1.28%. Gold was reported to have an ideal reflectance of 0.99 for $\lambda = 1.3\mu$m and 0.97 for $\lambda = 0.67\mu$m [20]. Gold is also known to resist oxidation. Therefore, coating the mirror with gold would be desirable. For gold coated polysilicon plates, the reported reflectance is 0.93 for 1.3μm wavelength [57]. The difference between the ideal and measured values may be due to contaminations on the mirror surface such as surface roughness and photoresist residue from processing. Although the measured reflectance does not differ greatly from the ideal value, the effective reflectance of the CCR would become only about 0.8 after 3 mirror reflections. Minimizing optical loss at each mirror is certainly desirable.

Non-ideal CCR mirrors with surface finish and coating nonuniformity may be characterized using a complex reflectivity for the different polarization states as a function of the reflectivity amplitude, phase, and angle of incidence. Then it can be shown that the CCR would conjugate not only the direction, but also the electric field of the incident beam. [84] Furthermore, the mirror curvature can further change an incident waveform. For example, a CCR with a single or multiple spherical mirrors can create circular or elliptical wave-fronts from an incident plane wave depending on the incident angle. [68]

An additional non-ideality of micro CCRs is diffractive spreading due to their small, finite size. Diffractive spreading determines the fundamental limit of the

maximum range of a micro CCR-based communication system. A simple approximation can be made by modelling a micro CCR as a circular aperture with a diameter equal to the dimension of the CCR, where the spreading of the reflected beam due to diffraction is Fraunhofer [29]. Then the half-angle divergence, θ_{CCR}, is defined by the following expression:

$$\theta_{CCR} \approx 1.2 \ sin^{-1}(\frac{\lambda}{d_{CCR}}) \approx 1.2 \ \frac{\lambda}{d_{CCR}} \tag{2.16}$$

where λ is the wavelength of the incident light, and d_{CCR} is the diameter of the CCR aperture. Based on this estimate, a CCR with dimensions of $250\mu m$ will have θ_{ccr} of about $3.26mrad$ for a wavelength of $670nm$. Finite-element analysis of a CCR which took into consideration of the mirror curvature and far-field diffraction effects showed that the differential scattering cross-section of a CCR with a mirror curvature of 0.3m is 451000m (near flat) [38]. In other words, the amount of reflected optical power by a CCR will decrease for increasing mirror curvature. In fact, the simulation shows that beam spreading will also increase for curved CCRs. It had also been proposed that slightly curved mirrors may be used in CCRs to correct velocity aberration in space application [68]. Clearly, controlling the curvature of the CCR mirrors would also be extremely important.

2.3 Micro CCRs for communication

Suppose we have CCRs with two distinct, reflective and non-reflective, states. We can then consider the effectiveness of using these CCRs for optical communication as described in Section 1.2. Suppose an interrogating light source is directed at a CCR and the reflected light is collected with an aperture as shown in Fig. 2.12. We would like to compare the reflected power from the CCR to the various noise

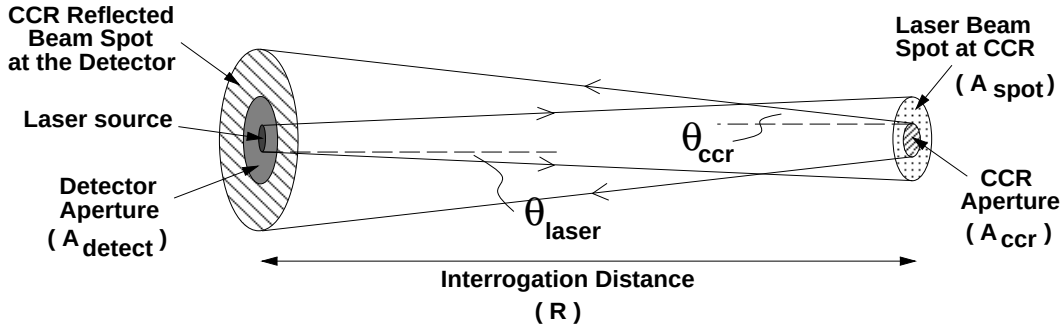

Figure 2.12: This figure shows a simple model of a CCR communication link for estimating signal-to-noise ratio based on the angle divergences of emitted and reflected beams.

sources in the communication link. The two noise sources which we will focus on are detector noise and background reflection. We will also briefly discuss other environmental noise sources.

2.3.1 Estimation of signal strength from an interrogated micro CCR

We are basically interested in knowing if the reflected signal from the CCR is detectable by the detector which is located at the light source as shown in Fig. 2.12. We will begin this analysis by estimating the amount of power which is reflected by the CCR and then received at the detector.

Suppose the interrogating light source emits a beam with power P_{laser} and a half-angle beam spread of θ_{laser}. Then the incident beam spot size at the CCR, A_{spot}, is given by

$$A_{spot} = \pi \times (\theta_{laser} R)^2 \tag{2.17}$$

where R is the interrogation distance. If a wide and near-columated laser is used, then A_{spot} should take on the appropriate expression based on the cross-section of the columated beam. Furthermore, we will assume that power loss due to

atmospheric effects and other optical losses are negligible. We will address these issues in a later discussion.

The irradiance (in W/m^2), I_{laser}, at the CCR and its surrounding, is the following:

$$I_{laser} = P_{laser} \times \frac{1}{A_{spot}}. \tag{2.18}$$

Let us define the effective area of the CCR as A_{CCR}. A_{CCR} is a function of the CCR's size and orientation and may be estimated using the methods described in Section 2.1.2. For simplicity, we will define A_{CCR} in terms of an effective CCR dimension d_{CCR}:

$$A_{CCR} = d_{CCR}^2 \tag{2.19}$$

The reflected power by the CCR, P_{CCR}, is simply the product of the incident irradiance I_{laser}, the CCR aperture A_{CCR}, and the CCR's reflectivity R_{CCR}, given by the following equation:

$$P_{CCR} = I_{laser} \times A_{CCR} \times R_{CCR} \tag{2.20}$$

The reflected power is proportional to the ratio of the effective size of the CCR and the laser spot because a larger CCR will capture and reflect more power than a smaller one. The reflected power is also directly proportional to laser power and the reflectivity of the mirrors, R_{CCR}. R_{CCR} is equal to the product of the reflectivity of each of the three mirrors. This reflectivity is determined by the fabrication process.

Although the reflected light beam from the CCR is highly directional (directed toward the interrogating light source), this beam will also have a measurable divergence, which we will called θ_{CCR}. Note that this divergence does not depend

on θ_{laser} because the actual rays which hit the micro CCR are nearly parallel due to the small size of the CCR. Instead, θ_{CCR} depends on the curvature of the micro mirrors and the diffraction effect of the CCR as discussed in Section 2.2.2. Now, for simplicity, we will assume that the curvature of the micro mirrors is negligible. We will also assume that the spreading of the reflected beam due to diffraction, θ_{CCR}, is proportional to the ratio of wavelength and the CCR dimension as shown in Eq. 2.16. Therefore, the incident irradiance from the CCR at the detector aperture (located at the interrogating laser distance R away), which we will call I_{CCR}, is given by:

$$I_{CCR} = P_{CCR} \times \frac{1}{\pi(\theta_{CCR}R)^2} \tag{2.21}$$

Let us assume that our receiver aperture has an area of A_{recr} which can only capture part of the reflected beam. This will generally be true because of beam spreading, especially for long range interrogation ($> 1km$). Let us also assume that power loss through the detector optics including filters, mirrors, and lens is negligible. Then the CCR incident power at the detector, $P_{CCR-inc}$, is the product of the CCR irradiance and the detector aperture area:

$$P_{CCR-inc} = I_{CCR} \times A_{recr} = P_{laser} \times \frac{A_{CCR} \times A_{recr}}{\pi^2 \theta_{laser}^2 \theta_{CCR}^2 R^4} \times R_{CCR} \tag{2.22}$$

From the equation above, we can conclude the CCR signal power has a strong dependent in R, the interrogating distance. We can further expand this equation by expressing A_{CCR} in terms of the effective CCR dimension (Eq. 2.19) and by expressing θ_{CCR} in terms of wavelength and CCR dimension (Eq. 2.16). The incident CCR power to the detector becomes the following:

$$P_{CCR-inc} = P_{laser} \times \frac{d_{CCR}^4}{(1.22\pi\theta_{laser}\lambda)^2 R^4} \times A_{recr} \times R_{CCR} \tag{2.23}$$

The above expression suggests that for a diffraction limited CCR, the size of the CCR has an extremely strong effect on the power returned by the CCR.

Suppose we use a 5mW, 670nm laser with θ_{laser} of 1.5mrad to illuminate a perfectly reflective CCR with d_{CCR} of $250\mu m$ located 100 meter away and we use a $10cm$ diameter aperture to collect the reflected light, only $51.7pW$ will reach the detector. This is an estimate of the "peak" power from the corner cube, where the CCR is turned on constantly. For a modulated CCR, we may consider the average power instead. Suppose the CCR emits an on-off-keyed signal with equiprobable ones and zeros, the average incident power, $P_{CCR-inc-avg}$, is simply $P_{CCR-inc}/2$. In Section 4.4.8, we will show that a pico-Watt CCR signal is well within detectable range.

Note that the analysis above could be carried out in terms of effective transmit antenna gain, free space range loss, receive antenna gain, and so forth, which are commonly used in analysis of RF and optical links [15, 54]. However, the same results will be reached. Our approach is chosen to provide an intuitive understanding based on the diagram in Fig. 2.12. Now, having estimated the amount of power reflected from the CCR, we will proceed to compare the received signal to the different noise sources.

2.3.2 Estimation of reflected light from the CCR background

Ambient light which is incident upon the receiver is undesirable for two reasons. The first reason is that it reduces the dynamic range of the actual signal which the detector could detect. If the intensity is too high, it could cause the detector to saturate so that no real signal can be detected. The second reason is that the ambient light creates a shot noise in the detector which is proportional to the

intensity of the ambient light (Section 2.3.3).

Two significant components of ambient light which reaches the receiver are the reflected interrogating laser from the CCR background and the general ambient light such as sunlight which also illuminates the CCR background. Before performing a SNR estimate for our receiver, we will first estimate the reflected interrogating power from the CCR background using a similar analysis as that in the previous section. We will also estimate the general ambient optical power which will reach our detector.

The interrogating laser has power P_{laser} and lights up an area of A_{spot} surrounding the CCR, so that the incidence irradiance is I_{laser} (Eq. 2.18). Suppose the background has an average reflectivity of R_{bg}. Then the reflected power from the background, P_{bg} is given by the following:

$$P_{bg-laser} = I_{laser} \times (A_{spot} - A_{CCR}) \times R_{bg} \tag{2.24}$$

Since $A_{spot} \gg A_{CCR}$, then P_{bg} becomes the following:

$$P_{bg-laser} = P_{laser} \times R_{bg} \tag{2.25}$$

Assume that the reflection from the background is Lambertian and the power is evenly reflected over the hemisphere. Incident irradiance from the background at the detector, I_{bg-inc}, will be the following:

$$I_{bg-laser-inc} = P_{bg} \times \frac{1}{2\pi R^2} \tag{2.26}$$

Therefore, the background incident power, P_{bg-inc}, at the detector is the following:

$$P_{bg-laser-inc} = I_{bg-inc} \times A_{recr} = P_{laser} \times \frac{A_{recr}}{2\pi^2\ \theta_{laser}^2 R^4} \times R_{bg} \tag{2.27}$$

Again, suppose we use a 5mW, 670nm laser with θ_{laser} of 1.5mrad to illuminate a micro CCR located 100 meter away and we use a $10cm$ diameter aperture to collect the reflected light. We will also assume that the background is highly reflective with R_{bg} of 0.5. Then $4.42nW$ of background reflection will be collected by the receiver. This background power estimate is almost 85 times greater than the CCR signal power estimate from Section 2.3.1.

Note that even though this estimate based on Eq. 2.27 is a reasonable one, the actual background reflection is highly dependent on the CCR background composition as well as the incident angle of the interrogating laser. For example, at one particular angle, a small piece of metal in the background might reflect like a perfect mirror. Yet the metal reflection might completely disappear at a later moment, when the interrogator (or the remote unit) has slightly moved, changing the incident angle. The most accurate background power estimate for a particular application scenario is to perform statistical power measurements of some realistic scenes. Nevertheless, we will use P_{bg-inc} as a estimate of the "average" incident power from the CCR background.

Besides the interrogating laser, the CCR background is also illuminated by other sources such as the sun, the moon, the planets and other stars. Street, building, or car lights may also have important effects. We will focus on the sun which is the highest energy source in our environment.

The sun has a wavelength dependent spectral distribution which is well approximated by a black body at $T = 5900K$. The spectrum is given by the Planck radiation law [20]:

$$p(\lambda, T) = \frac{2\pi hc^2}{\lambda^5(e^{\frac{hc}{\lambda kT}} - 1)} \tag{2.28}$$

For wavelength between 0.6 to $1\mu m$, the solar irradiance at sea level is between

1.3 to $0.5W/(m^2\ nm)$. For simplicity, we can approximate it to be $1W/(m^2\ nm)$. Suppose we put a bandpass optical filter in front of our detector with a bandwidth $\delta\lambda$ of 5nm. Then the solar irradiance of our concern, I_{solar}, is about $5W/(m^2)$, assuming that our receiver is aimed at directly at the sun.

Our optical communication link is unlikely to work if the sun is in fact behind the remote unit with the CCRs because of the sun's intense brightness. Fortunately, in any realistic practical applications, the sun will be illuminating the CCR background, and only the reflected solar light will reach the receiver.

To estimate the solar power incident at the receiver, we can assume that the reflection of the background is Lambertian and the background has a reflectivity of R_{bg}. We will also assume that the receiver has a field of view of θ_{recr} and that only objects inside the field will reflect solar light to our receiver. Then that solar power incident at our receiver, $P_{bg-solar-inc}$, may be approximated by the following expression:

$$P_{bg-solar-inc} = I_{solar} \times \frac{\pi(\theta_{recr}R)^2}{2\pi R^2} \times A_{recr} \times R_{bg} = \frac{1}{2} I_{solar} \theta_{recr}^2 A_{recr} R_{bg} \quad (2.29)$$

Suppose θ_{recr} is 35mrad (2 deg) and R_{bg} is 0.5, then $P_{bg-solar-inc}$ is about 0.24mW. This power estimate is actually more than 40,000 times greater than the power estimate from a CCR illuminated by a 5mW laser. However, similar to the background reflected interrogating laser estimate, this solar power estimate is also a reasonable yet rough estimate. The total ambient light incident at the receiver, $P_{amb-inc}$, is the sum of these two power:

$$P_{amb-inc} = P_{bg-laser-inc} + P_{bg-solar-inc}. \quad (2.30)$$

Large $P_{amb-inc}$

2.3.3 Performance analysis for a receiver with a single detector

The performance for a communication link using a CCR obviously would depend on the receiver design and the signaling method. In this section, we will make some assumptions of a receiver and estimate the signal-to-noise ratio (SNR) and bit-error probability (P_e) associating with a CCR based communication link.

Suppose the CCR of the remote unit is modulated using unipolar modulation or on-off keying (OOK) [18]. Consider a receiver using direct detection (or incoherent detection), where the incident light at the receiver is directly converted into current such that the power of the light is proportional to current. This method of detection assumes that the incoming signal is amplitude modulated, and its phase carries no information [65, 54].

We will also assume that all the light collected by the receiver aperture is directed to a single detector. Commonly used optical detectors for communication include p-intrinsic-n (PIN) photodiodes and avalanche photodiodes [82, 65, 27]. Avalanche photodiodes are similar to PIN diodes, but they offer an internal electric gain given a high reverse bias. This internal gain may be used to overcome preamplifier thermal noise if ambient-induced shot noise is low. However, it may actually decrease the net SNR when ambient-induced shot noise is high [47]. Since high ambient noise is present in our application, photodiodes are prefered. Therefore, we will carry out analysis for PIN photodiodes.

The current by a photodiode, I_{ph}, generated by an input optical power P_{in} is given by this:

$$I_{ph} = \eta(\lambda)\frac{q}{hc}P_{in} = R_{det}(\lambda)P_{in} \tag{2.31}$$

where η is the detector quantum efficiency, h is the Planck's constant, c is the

speed of light, λ is the wavelength, and q is the electronic quantum charge. R_{det} is the responsivity of the detector. Typical silicon PIN detector responds to light with λ between 0.6 to $1\mu m$, where R_{det} peaks at about $0.9W/A$ for λ of about $850nm$. Other Ge, InGaAs, and InGaAsP PIN detector may have ranges beyond $1.7\mu m$ and maximum R_{det} near 0.8.[54]

The average received photocurrent from a modulated CCR, i_{CCR}, is given by Eq. 2.31 which P_{in} is substituted by $P_{ccr-inc-avg}$ defined in Section 2.3.1.

$$i_{CCR} = R_{det} \times P_{ccr-inc-avg} \tag{2.32}$$

Similarly, a photocurrent will be generated from the incident optical power from ambient light P_{amb}, including P_{bg-inc} (Eq. 2.27), the background reflection of the interrogating light, and other ambient light sources. This current is defined by

$$i_{amb} = R_{det} \times P_{amb-inc} \tag{2.33}$$

Another current which the detector outputs is commonly known as the dark current, i_d, which may include the reverse bias current [65] and carriers which are generated in the depletion layer and those which diffuse into the depletion layer from the p^+ or n^+ regions [27]. The magnitude of i_d depends on the geometry and property of the photodetector. It is generally related to the area and the operating temperature of the detector. The dark current for typical commerical silicon PIN detectors with small areas ($13mm^2$) is about $10^{-12}A$ ($10^{-14}A/\sqrt{Hz} \times \sqrt{10kHz}$).

All these different currents induce a white, Gaussian, shot noise with a one-sided power spectral density $S_{shot}(f)$ [47, 78], given by

$$S_{shot}(f) = 2q(i_{CCR} + i_{amb} + i_d) \tag{2.34}$$

From the estimates in Section 2.3.1 and Section 2.3.2, we know that i_{amb} is about 50 times greater than i_{CCR}. i_{amb} in general will also be many times larger than i_d.

Therefore,

$$S_{shot}(f) \approx 2q(i_{amb}) \tag{2.35}$$

Beside shot noise, thermal noise in the preamplifer will also degrade the performance of the receiver [54, 47]. This noise generally is also a white Gaussian noise, whose spectral density is $4kT/R$ plus other terms depending on the exact preamp circuit. k is the Boltzmann constant; T is the temperature; and R is the feedback resistor. We assume that shot noise is the dominating noise source in our application; therefore, we will neglect thermal noise in this analysis.

Therefore, the simplified receiver noise has a variance σ^2_{total} equals to σ^2_{shot} given by the following:

$$\sigma^2_{total} = \sigma^2_{shot} = 2q(i_{CCR} + i_{amb} + i_d)B \tag{2.36}$$

where B is the data bit rate. The signal-to-noise ratio for the receiver is given by the following:

$$SNR = \frac{(i_{CCR})^2}{\sigma^2_{total}} = \frac{(i_{CCR})^2}{2q(i_{CCR} + i_{amb} + i_d)B} \tag{2.37}$$

The bit error rate, BER, is given by the following:

$$BER = Q(\sqrt{SNR}) \tag{2.38}$$

where $Q(x)$ is Gaussian function given by

$$Q(x) = \frac{1}{\sqrt{2\pi}} \int_x^\infty e^{-\frac{y^2}{2}} dy. \tag{2.39}$$

As an example, to achieve $BER = 10^{-6}$, an SNR of about $13.5dB$ is required.

In order to understand better how the different design parameters may affect the system performance, we will derive the SNR based on the following assumptions. We will assume that all environmental light sources such as the sun is absent

such that i_{amb} is only contributed by the background reflected interrogating light. We will also assume that the noise current induced by the background-reflected interrogating light is much larger than i_{ccr} and i_d, i.e. $i_{amb} \gg i_{ccr} + i_d$. Then SNR is equal to the following:

$$SNR = P_{laser} \frac{A_{CCR}^2 A_{recr}}{2\pi^2 q B \theta_{laser}^2 \theta_{CCR}^4 R^4} \frac{R_{CCR}^2}{R_{bg}} R_{det} \tag{2.40}$$

From this SNR expression, we can more clearly see the effects of the different design parameters. For example, the interrogating range R is shown to have a significant effect on the SNR. When R is doubled, SNR is reduced by 16 times. Similarly, small CCR divergence is also shown to be very important because the CCR reflection will better "stand out" against the dispersed background reflection. Large CCR or arrays of CCRs would also be beneficial, where SNR has a quadratic dependence on A_{CCR}. Using higher power laser or larger receiver aperture could also help, but SNR would only increase proportionally to these parameters.

2.3.4 Performance analysis for a receiver with multiple detectors

Shot noise due to ambient light in photo-detector systems generally may be reduced by operating the system at night or using appropriate optical filters to remove undesirable wavelengths. Unfortunately, as shown in the previous section, even when solar radiation is ignored, substantial shot noise is induced by the system's own interrogating laser reflected from the background. One method of improving our receiver performance is to use multiple detectors instead of a single detector as discussed in the previous section.

In the single-detector case, all the undesirable ambient light as well as the CCR reflection is directed to the detector. Therefore, the CCR signal must compete with

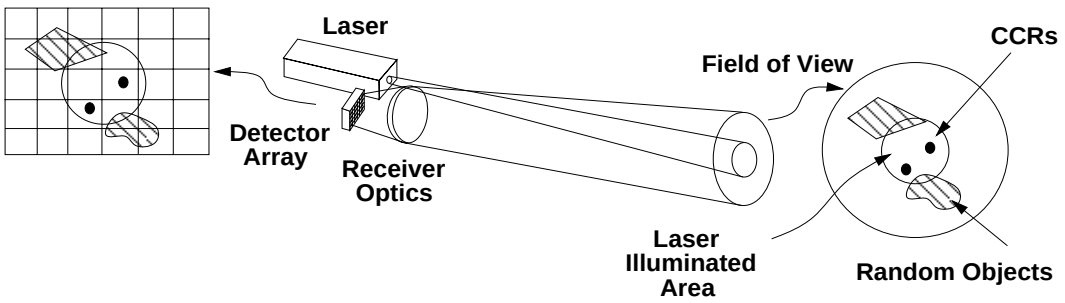

Figure 2.13: This figure shows an optical receiver using a detector array. The image in the field of view is mapped into an array of pixels so that each pixel only sees a small fraction of the field of view.

all the ambient light and the associated shot noise. In the multiple-detector case, each detector only looks at a small portion of the background, thus having corresponding less noise depending on the total number of detectors used (Fig. 2.13). The CCR reflection may rest on only a single detector or possibly a few detectors, but the signal-to-noise ratio for the detectors with the CCR reflection is substantially increased from the single-detector case. In essence, the background image is "spatially-filtered" to yield an increased SNR.

2 by 2 detector arrays known as quadrant detectors are most commonly used in optical detection system [54]. Charge-coupled devices (CCD) or arrays of or PIN devices can also be used for our application. Furthermore, CMOS-based active-pixel cameras would also be a suitable candidate for this application. [26] An important concern for detector arrays is to minimize the dead zone present between the adjacent pixels or detectors so the CCR reflection would not be ignored or missed [54, 38]. With detector arrays, the receiver may also require more data storage and processing speed and intelligence.

Analysis of this system would be similar to the single-detector system. Consider the best case where all the CCR reflection rest on a single detector (or pixel). The

current induced from a CCR reflection, i_{CCR}, is given by Eq. 2.32. The current induced by ambient light, i_{amb}, is given by the following:

$$i_{amb} = \frac{R_{det} \times P_{amb}}{N_{det}} \tag{2.41}$$

where N_{det} denotes the total number of detectors or pixels used. For simplicity, we assume that all the ambient light is evenly distributed to all the different detectors. The best case SNR has the same expression as the SNR given by Eq. 2.37:

$$SNR = \frac{(i_{CCR})^2}{\sigma^2_{total}} = \frac{(i_{CCR})^2}{2q(i_{CCR} + i_{amb} + i_d)B} \tag{2.42}$$

However, since the i_{amb} here has a factor of N_{det} smaller than the i_{amb} for the single-detector case, SNR in this case is N_{det} times larger than the SNR for the previous case. BER may be estimated using Eq. 2.38.

Suppose the CCR reflection rests on multiple (N_{CCR}) pixels instead of just one pixel. Depending on the technique used to process the signals, such as using maximal-ratio combining (MRC) or selecting a single best from N_{CCR} pixels, SNR may be reduced by a factor of either N_{CCR} or N^2_{CCR}[38]. Therefore, the minimum net SNR gain of using a detector array is N_{det}/N^2_{CCR}.

2.3.5 SNR analysis for several CCR systems

Table 2.2 shows a list of design parameters and a set of plausible values for these parameters to achieve reasonable values of SNR and BER for a communication link based on a diffraction- limited CCR. Assumed values for several environmental variables are also listed. Table 2.3 shows the SNR and BER results for several CCR system designs, where most of the system variables are held constant except for interrogating laser power, P_{laser}, number of detectors used, N_{det}, and number

Symbol	Description	Value	
P_{laser}	Interrogating laser power	$0.005 - 10$	W
θ_{laser}	laser half-angle divergence	1.5	$mrad$
λ_{laser}	laser wavelength	670	nm
$\delta\lambda$	optical filter bandwidth	5	nm
d_{CCR}	effective CCR diameter	250	μm
R_{CCR}	effective CCR reflectivity	0.80	W/W
d_{recr}	receiver diameter	10	cm
θ_{recr}	receiver field of view	35	$mrad$
R_{det}	detector responsivity	0.8	A/W
N_{det}	number of detectors	$1 - 10^5$	-
N_{CCR}	number of detectors with CCR reflection	$1 - 4$	-
R	communication range	$1 - 10^3$	m
B	data bit rate	10^4	bps
R_{bg}	background reflectivity	0.4	W/W
I_{solar}	solar irradiance	1	W/m^2nm
i_d	dark current in each detector	10^{-12}	A

Table 2.2: Design parameters for a CCR communication link

of detectors on which the CCR reflection rests, N_{CCR}. Note that N_{CCR} is actually not a controllable design parameter and is used here to create different scenarios.

The SNR and BER estimates in Table 2.3 are based on the expressions derived in the previous sections. The results suggest that by simplying changing P_{laser} and N_{det}, communication across up to $1km$ with a CCR can be achieved with reasonable SNR and BER. The presence of sunlight is shown to have a significant effect on the system requirements. Without sunlight, a given system can establish communication across a much larger range. Furthermore, because of the SNR's strong dependence on the range R, whenever R is doubled, either P_{laser}, N_{det}, or both must be significantly increased to maintain the same SNR.

Atmospheric effects such as absorption, scintillation [69], beam spreading, scattering, and beam bending could complicate the proposed optical communication

$R(m)$	$P_{laser}(W)$	N_{det}	N_{CCR}	Sun	SNR	BER
50	0.005	1	1	Y	11.3	7.8×10^{-4}
100	0.005	1	1	N	119	0
100	0.1	1	1	Y	17.6	2.7×10^{-5}
200	0.2	64	1	Y	27.7	2.5×10^{-5}
500	0.2	4	1	N	28.9	7.6×10^{-8}
500	5.0	1600	4	Y	11.3 *45.0	7.7×10^{-4} *1.8×10^{-11}
1000	10.0	90000	4	Y	9.68 *38.0	1.9×10^{-3} *7.0×10^{-10}

Table 2.3: SNR analysis results for different CCR systems. Results with asterisks assumes maximal-ratio combining (MRC) is used.

strategy for large communication distances [44]. The non-ideality of a fabricated CCR such as mirror curvature and poor orthogonality could also increase the divergence of the returned light, thus decreasing SNR. If the communication distance is very large, arrays of CCRs and high power lasers may become necessary. Nevertheless, this analysis suggests that a careful selection of CCR, laser, and detector could achieve an SNR which may satisfy a variety of applications.

3 Polysilicon Micro Corner Cube Reflectors

3.1 Mechanical design of CCR

We have designed and fabricated many surface micromachined micro CCRs for the MUMPS multiple layer polysilicon process offered by MCNC. The goal was to create a CCR with good optical quality, good orthogonality, reasonable bandwidth, low voltage and power requirement, and ease of assembly. The designs of the different CCR components including the mirrors, hinges, locking mechanism, and actuator are presented in the following sections.

3.1.1 Micromachining with MCNC's MUMPS process

MCNC's MUMPS (Multi-User MEMS Processes) is a surface micromachining process which offers four conducting layers (3 polysilicon layer and 1 gold), and 3 insulating layers (2 oxide and 1 nitride). Fig. 3.1 shows a cross-section of all the layers stacked on a substrate. The silicon nitride layer is used an electrical isolation layer between the substrate and the polysilicon structures on the substrate. The two oxide layers ($Ox1$ and $Ox2$) made of phosphosilicate glass (PSG) are generally removed in a post-process etch so that the $Ply1$ and $Ply2$ layers become free. $Ox1$ and $Ox2$ are known as the sacrificial layers, and $Ply1$ and $Ply2$ are known as the structural layers which form the microstructures. Unlike the other poly layers, the $Ply0$ layer adheres to the substrate. It can be used to provide electrical connection between different $Ply1$ and $Ply2$ structures.

All the conducting layers can be patterned to a specified geometry according to the layout submitted to MCNC as long as a set of design rules are obeyed. In general, the minimum line width and spacing are either 2 or $3\mu m$. The oxide

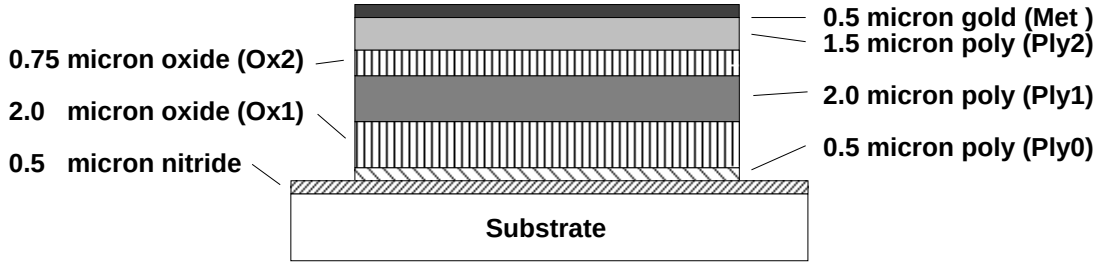

Figure 3.1: Cross-sectional view of the layer structure for the $2\mu m$ MCNC MUMPS process is shown.

layers (and well as the nitride layer) can also be patterned using the different contact layers, which create holes in the oxide layers. By appropriately defining holes in the oxide layers, the poly layers can be interconnected to each other and to the substrate. The sacrificial oxide is usually removed using a hydrofluoric acid (HF) wet bath. More details related to the HF release etch will be discussed in Section 3.3.1.

A variety of microstructures can be fabricated using this sacrificial etching surfacing micromachining process with one or two layers of polysilicon as structural material. Fabricated structures include beams [37], spring, pin-joints, gears [24], resonators [91], and micromotors [23]. Development of microhinges [77] allowed large plates to rotate up from the substrate to form micro mirrors and lenses [63, 98]. In the following sections, we will describe how to use this surfacing micromachining technology to fabricate micro corner cube reflectors.

3.1.2 Micro mirrors

$2\mu m$ thick polysilicon plate was previously reported to have a reflectivity of 24% [31]. Since the incident light hits three mirror surfaces of the CCR before it is reflected back, the net reflectivity of a CCR with polysilicon mirrors would be $(24\%)^3$, or

about 1.4%. In other words, using polysilicon as the reflecting surface will not yield a highly reflective CCR.

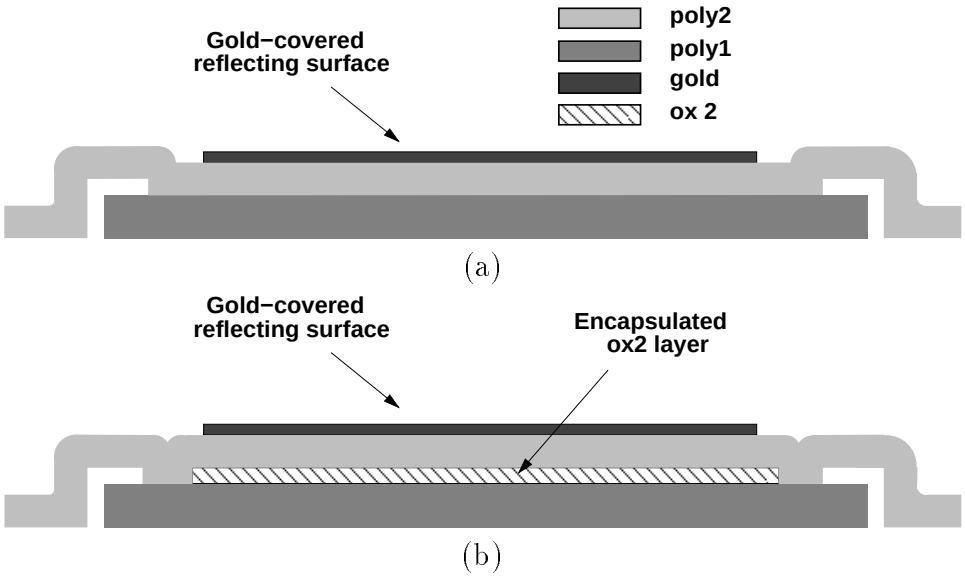

Figure 3.2: The cross-section of a polysilicon mirror with gold is shown in (a). The ox2 layer is added to the mirror stack in order to decrease the curvature of the mirror.

To create CCRs with high reflectivity, we tried to make mirrors by putting gold on polysilicon plates because gold films typically have reflectance of at least 95% for wavelength greater than $500nm$ [20]. The MCNC's MUMPS process offers a $0.5\mu m$ gold metal layer which may be deposited on $ply2$, the second structural polysilicon layer. To minimize post-processing, we tried to take advantage on this metal layer to make mirrors.

Fabricated mirror plates typically have linear dimensions of 250 to 300μm. No etch holes are put in the plates in order to create smooth mirror surfaces. Fabricated mirrors were found to have various degrees of curvature depending on the layer stack of the mirror. The curvature was caused by the stress in the tensile metal layers, 0.5μm Au on top of 300$\mathring{A}$ Cr which is used to help the gold layer to

Layer stack	Radius of Curvature (in mm)
$ply1$, $ply2$	90
$ply1$, $ox2$, $ply2$	16.8
$ply2$, gold	1.67
$ply1$, $ply2$, gold	9.58
$ply1$, $ox2$, $ply2$, gold	21.4

Table 3.1: Measured curvature results of mirrors with different layer stacks.

adhere to the polysilicon layer. The reported values of stress in the metal films from various runs ranged from 50 to 60MPa (for MUMPS Run 11, 12, and 14). The stress in the Au layer was reported to be quite low, only 3 to 5MPa, while much of the tensile stress was from the Cr layer. In contrast with the polysilicon layers with a typical compressive stress of -10MPa, the metal films had 6 times higher stresses.

For a cantilever beam composed of two materials with different residual stresses, σ_1 and σ_2, elastic moduli, E_1 and E_2, and thicknesses, h_1 and h_2. At static equilibrium, the radius of curvature of the beam, ρ, can be readily estimated using the following expression [46]:

$$\frac{1}{\rho} = \frac{6(m\sigma_2 - \sigma_1)}{E_2(h_1+h_2)(3m + \frac{K}{n(1+n)^2})} \tag{3.43}$$

where

$$K = 1 + 4mn + 6mn^2 + 4mn^3 + m^2n^4 \tag{3.44}$$

and m and n are defined as the ratios of material properties and thicknesses:

$$m = \frac{E_1}{E_2} \tag{3.45}$$

$$n = \frac{h_1}{h_2}. \tag{3.46}$$

ρ is shown to have a complex relationship with the stresses, elastic moduli, and material thicknesses. For a rectangular plate composed of different materials, the plate curvature cannot be accurately described using a single variable. The radius of curvature estimate of a beam may be used as a first order estimate.

Table 3.1 shows measured curvature results for mirrors with different layer stacks to demonstrate the effect of the tensile metal layer. The curvature was measured using a Wyko white-light interferometer across the center cross-section of the rectangular mirrors with widths of $300\mu m$. All the measurements generally seemed reasonable and consistent. The measured curvature values for the "bi-layered" mirrors were found to be smaller than the theoretical estimates using Eq. 3.43 (by 35% to 50%). Since only rough estimates of stresses and elastic moduli are known, the theoretical estimates are indeed reasonable closed to the measured values.

Mirrors made of the $ply2$ layer with gold were found to be unusable for our CCR designs because of their extreme curvature. Double-poly-layer mirrors created by stacking the $ply1$ and $ply2$ layers via a large $ply2$-to-$ply1$ contact showed significantly less curvature. Fig. 3.2(a) shows the cross-section of the mirror. The fabricated mirrors have measured radius of curvature ranging from 7 to $9.8mm$, which would give a reflected light ray an estimated divergence of 15 to $20mrad$. Functional CCRs were made using these mirrors [12].

The latest mirror designs were modified from the double-poly-layer mirrors so that the $0.75\mu m$ $ox2$ layer was "sandwiched" between the $ply1$ and $ply2$ layers (Fig. 3.2(b)). Measured radius of curvature of these mirrors ranges from 18 to $20mm$; therefore, the increase in stack thickness and compressive stress in the stack has lowered the radius of curvature by at least 50%.

Ideally, the curvature of these plates may be further reduced by increasing the thicknesses of the polysilicon or oxide layers, decreasing the metal layer thickness, particularly the Cr layer, or using even different metals. Unfortunately, we lack this option since these process parameters are fixed by the foundry. Better curvature results may also be achieved by depositing metal on the MCNC chips as a post-processing step so that the metal thicknesses may be fine tuned. Post-processing metal deposition may take place before or after the release etch. If the reflective metal layer such as Au is deposited before the release etch, it may be patterned very easily; however, a sufficiently thick adhesion layer must be used (such as Cr) in order to prevent the metal layer to come off during the HF etch. As a result, the metal film stress may or may not be reduced adequately. On the other hand, if the metal layer is deposited after the release etch, no adhesion layer may be needed; however, since patterning the metal layer may not be possible, other means must be used to prevent electrical shorting of the die surface.

Even though these post-processing options will likely be successful in reducing the mirror curvature, we did not attempt to reduce the mirror curvatures further, mostly because the fabricated CCRs offered satisfactory performance for our demonstration.

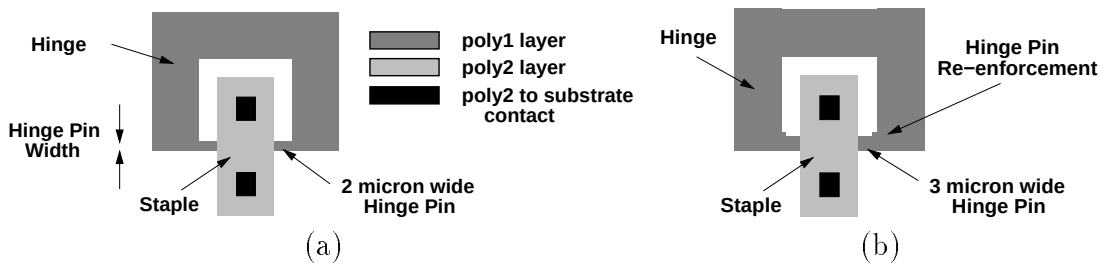

Figure 3.3: The layout of a typical polysilicon hinge is shown in (a). The hinge was strengthened in (b) by increasing the hinge pin width and by adding re-enforcement at the hinge pin ends.

3.1.3 Mechanical alignment

To form the two of the three reflective surfaces of the CCR, the polysilicon mirrors described in Section 3.1.2 are rotated to a position normal to the substrate using microhinges [77]. Fig. 3.3 shows layouts of two microhinges, where $Ply1$ forms a hinge with a thin hinge pin and $Ply2$ forms a staple which pins the hinge to the substrate.

In earlier designs, $2\mu m$ width hinge pins were used (Fig. 3.3 (a)). These hinge pins were found to break easily during the release etch or during assembly. The width were then increased to $3\mu m$. The stiffness of the pin is proportional to EI where E is the modulus of elasticity and I is the moment of inertia of a beam cross-section. For a rectangular beam, I is given by

$$I = \frac{1}{12}a^3 b \tag{3.47}$$

where a and b are the dimension of the beam cross-section. Therefore, by increasing the pin width by 50%, the pin would become 50% to 335.7% stiffer depending on the direction of an applied force.

To strength the hinge further, the ends of the hinge pins were also re-enforced by adding a $1\mu m$ square at the inside corners of the rectangular hinges (Fig. 3.3 (b)). Fig. 3.4 (a) and (b) show SEMs of fabricated hinges based on the designs in Fig. 3.3. The inside corners of both designs actually appeared rounded; however, the radius of curvature is clearly larger in the re-enforced hinge. Therefore, the factor of stress concentration, which is a function of the ratio of the radius of curvature and the width of the hinge pin, is likely to be 10% or more less than that of the previous design (estimated based on a square corner in tension [100]). In general, the redesigned hinges were found to be extremely robust and reliable.

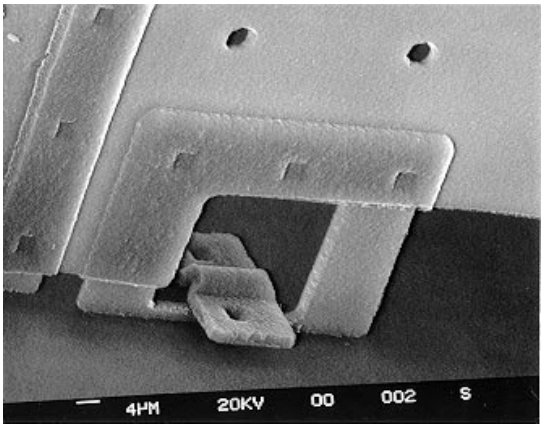

(a)

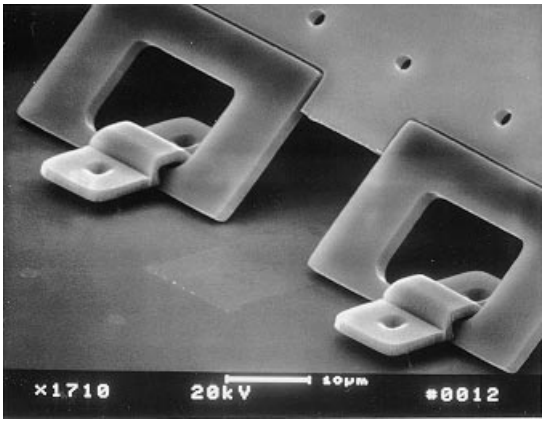

(b)

Figure 3.4: (a) A polysilicon micro-hinge based on the earlier design shown in Fig. 3.3(a). (b) Two micro-hinges with increased hinge pin width and re-enforced hinge pin ends.

As a result, no further modification was made.

The hinge pin design not only affects the yield of the device by also the alignment of the mirrors. For example, from Fig. 3.3, we can see that the hinge pin is made longer than the width of the staple. In fact, the hinge pin must be made longer than the staple width by at least 2 times the minimal line-width spacing between $Ply1$ and $Ply2$. Therefore, the hinge may translate $\pm 2\mu m$ in the direction parallel to the length of the hinge pin, potentially causing the hinged structures to misalign. These micro hinges may also have additional translations and rotations.

Fig. 3.5 shows the cross-section drawing of the polysilicon hinge in Fig. 3.3(b). After the sacrificial $Ox1$ and $Ox2$ layers are removed, the hinge pin has an excess of free space to translate and rotate. From the cross-section drawing in Fig. 3.5, we can see that the hinge pin lies in a channel underneath the staple which has a $4.5\mu m \times 4.25\mu m$ cross-section. The $4.25\mu m$ height is defined by the layer thickness of $Ox1$, $Ply1$, and $Ox2$. The $4.5\mu m$ width is defined by 2 times the $Ox2$ thickness

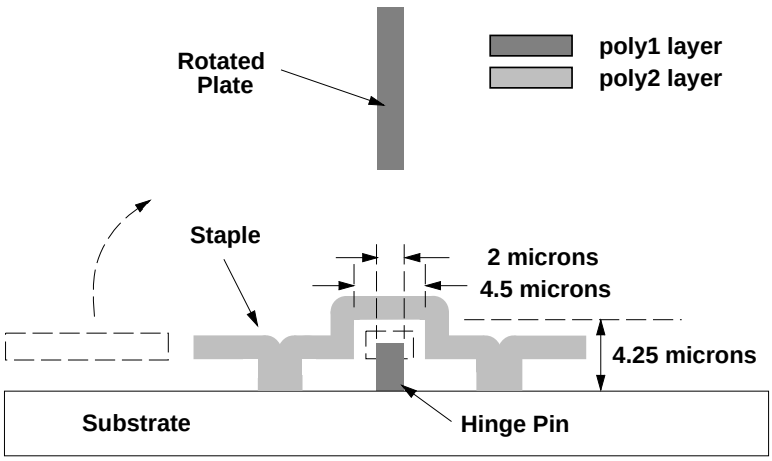

Figure 3.5: The cross-section of the polysilicon hinge in Fig. 3.3(b) shows the excess of free space around the hinge pin which can cause misalignment problems.

($0.75\mu m$) and the hinge pin width ($3\mu m$). If the hinge pin width is set to the minimum line width of $2\mu m$, the channel width is reduced to $3.5\mu m$. In any case, an excess of free space is still present in a micro hinge. This play in the hinges can easily cause a hinged plate to be misaligned due to lateral displacement or rotation of the hinge pin.

To overcome the play in the hinges, long tie-downs are added to the base corners of each rotated plate whenever possible. Typically a tie-down is composed of a thin folded beam which connects a plate to the substrate via a small contact (Fig. 3.6(a)). Tie-downs are usually used to prevent large plates of a structure from moving during the wet release process, and the connecting beams are broken manually prior to the actual assembly of the structure. In our case, the short folded connecting beam in the tie-down is replaced by a long straight beam and the tie-down is connected to a hinged plate such that rotation is possible, but translation is minimized (Fig. 3.6(b)).

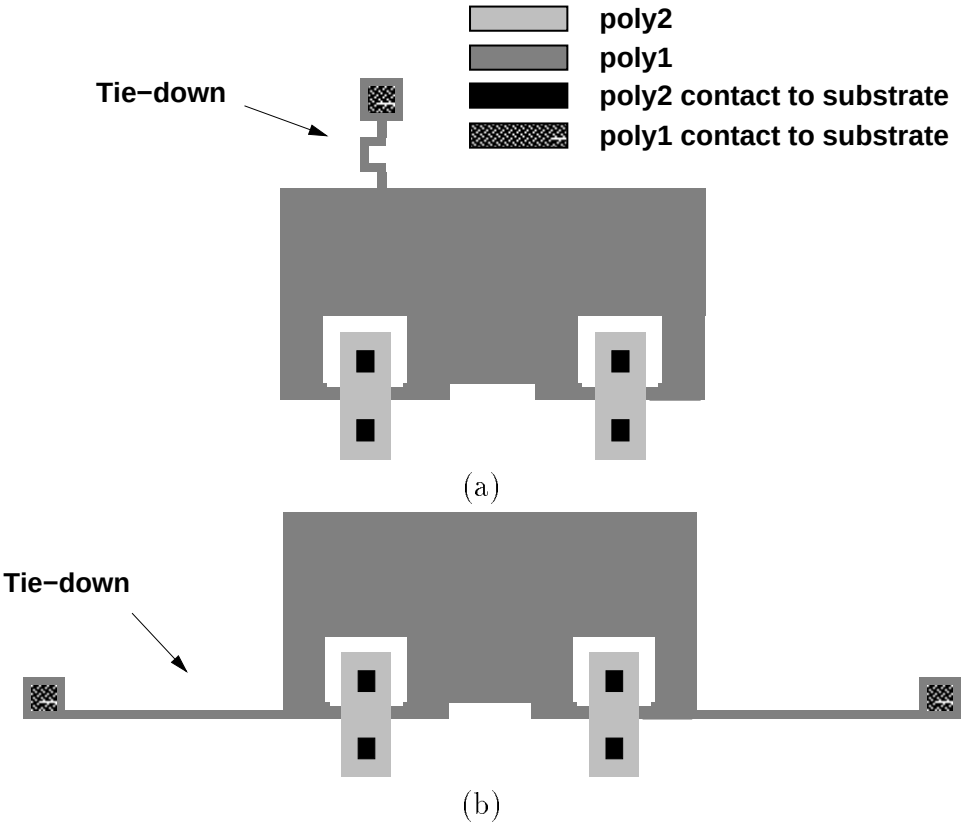

Figure 3.6: The layout of a hinged plate connected to a typical polysilicon tie-down is shown in (a). A hinged plate with long tie-downs is shown in (b).

The connecting beams have lengths ranging from 90 to $250\mu m$ with a width of $2\mu m$, which is the minimum line width. The precise length and width are not critical as long as the beams can tolerate the desired rotation, i.e. the maximum shear strain from the rotation is less than the shear strain limit for polysilicon. For a rectangular beam with length L and cross-section dimensions a and b where $a > b$, the maximum shear strain occurs along the centerline of the wider sides of the beam, and is given by

$$\gamma_{max} = k\frac{b}{L}\phi \tag{3.48}$$

where ϕ is the angle of rotation in radians. k is a dimensionless constant depending

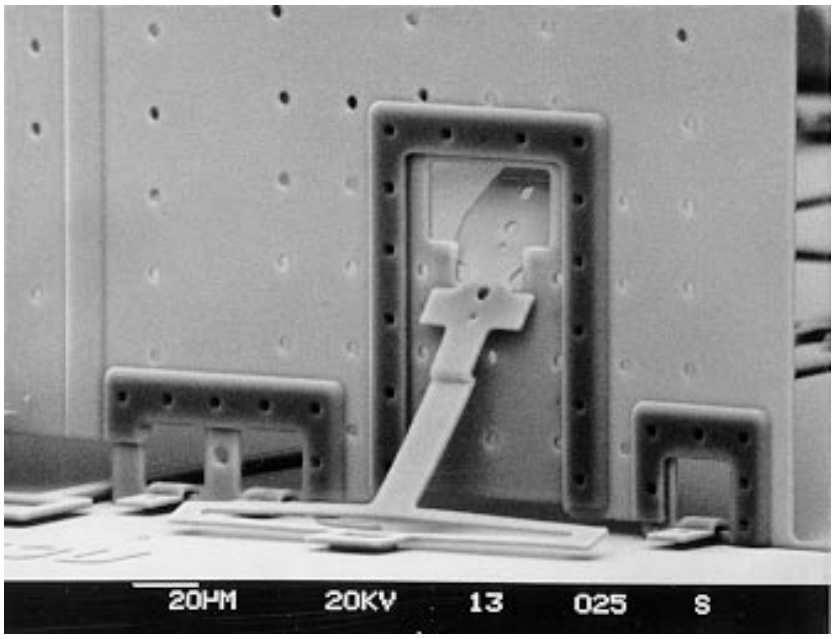

Figure 3.7: This SEM photo shows a polysilicon torsional lock keeping a polysilicon plate in a vertical position.

only on a and b [100]. For $a/b = 1.5$, k is computed to be 0.848.

For polysilicon, various values of the modulus of elasticity, Poisson's ratio, tensile strength and fracture tensile strain had been reported [90, 41, 85]. A study based on several MUMPS runs reported $169GPa$, 0.22, and $1.20GPa$ for the three values respectively [85], suggesting a tensile strain limit of 0.71% and a modulus of rigidity of $69GPa$. Unfortunately, no reported shear strain limit for polysilicon was found. As a rough estimate, assume that the shear strain limit is twice the tensile strain limit. Then, in order to rotate a tie-down 90 degrees without fracturing, a $2\mu m$ $Ply1$ beam with a length of $100\mu m$ or more should be adequate. From fabricated structures, tie-downs with length less than $100\mu m$ were indeed found to break frequently during assembly.

Once the mirror plates are rotated upright, they are usually locked in place with

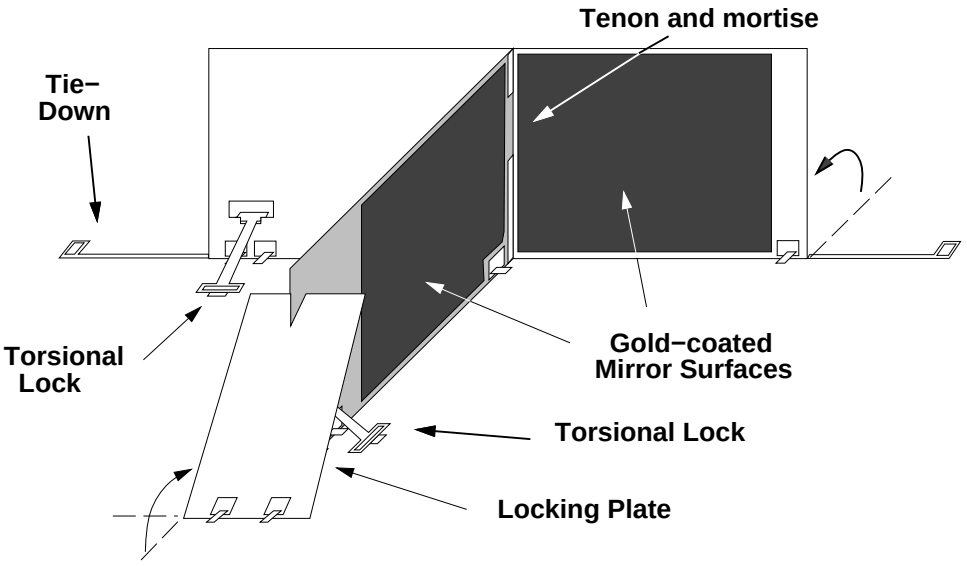

Figure 3.8: This drawing shows how the different locking mechanisms are used to form two orthogonal mirrors for the corner cube reflector. The substrate may act as the third orthogonal mirror. Note that this CCR cannot modulate incident light.

torsional spring locks. Fig. 3.7 shows a torsional spring lock which is composed of a spear-shaped beam connected to a torsional spring on the substrate. When the plate is being rotated upright, the spear-shaped beam goes through a hole on the plate and eventually catches a slot on the plate. To further ensure the orthogonality of the vertical plates, we also used tenons, mortises, and additional plates with slits for alignment and support (Fig. 3.8).

Fig. 3.9 shows an assembled CCR with the various alignment and locking mechanisms built in. This CCR has a movable substrate mirror which was not shown in the design in Fig. 3.8. The design of actuated mirrors will be discussed in greater details in the following section. Excellent alignment between the vertical mirrors is evident from the close-up view of the edges of the mirrors where the tenon and mortise meet (Fig. 3.10). The tenon is made of a $2\mu m$ slit on the right mirror

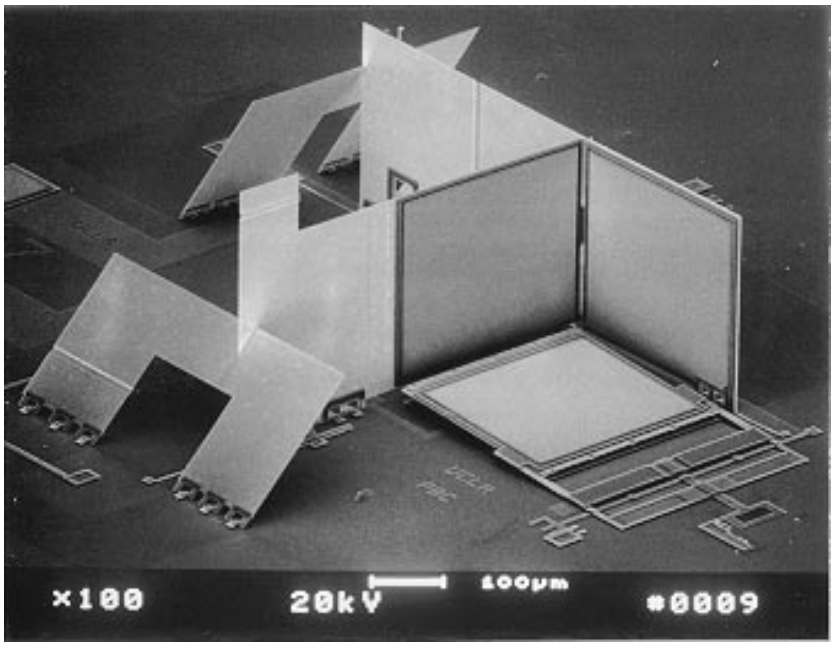

Figure 3.9: A micro CCR with various locking mechanisms showing excellent alignments for the vertical mirrors. This CCR also has an electrostatic base mirror which is currently rested at an angled position.

plate. The mortise is made of a $Ply1$ stub which is also $2\mu m$ thick, forming a perfect fit with the slit. Fig. 3.11 shows how the mortise protrudes through the mirror plate with the slit. Although this design yielded good results, the drawback of using $2\mu m$ slit for a $2\mu m$ stub was that assembling the two parts together was often difficult.

The locking plates which are folded over the mirror plates to improve the alignment were found to be necessary with the current torsional lock design. Fig. 3.12 shows the same CCR as in Fig. 3.9 without the locking plates assembled. It is apparent from the SEM that the two vertical plates are not perfectly aligned. Eliminating the locking plates is desirable for simplifying the assembly process and for minimizing the chip area needed for each CCR. With an improved torsional

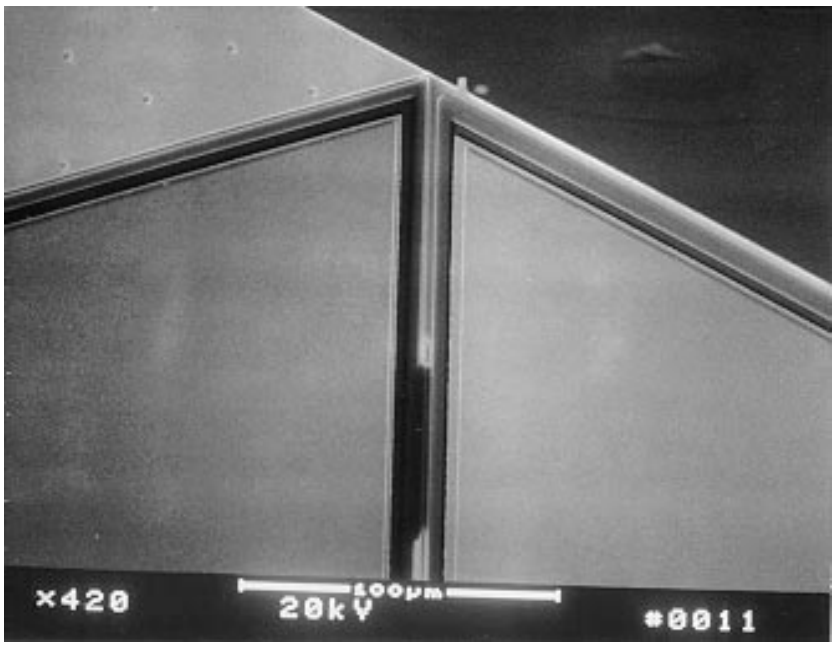

Figure 3.10: A close-up view of the micro CCR in Fig. 3.9 shows that the edge of one mirror appears to be perfectly aligned with the other mirror plate.

lock design or other lock designs, CCRs without locking plates should be possible.

3.1.4 Actuated micro mirrors for CCRs

To use a micro CCR for communication, we require that the CCR must be able to modulate the incident light. If just one of its three mirrors becomes misaligned, the CCR will deflect the incident light away from its source, thus modulating the light. Therefore, we decided to add a movable base mirror to the CCR in Fig. 3.8 and to keep the vertical mirrors stationary because it seems more simple to modulate the base mirror than one of the vertical mirrors.

We also designed an actuated mirror such that in its idle state (with no actuation voltage applied), the CCR will not be orthogonal. The benefit of this design is

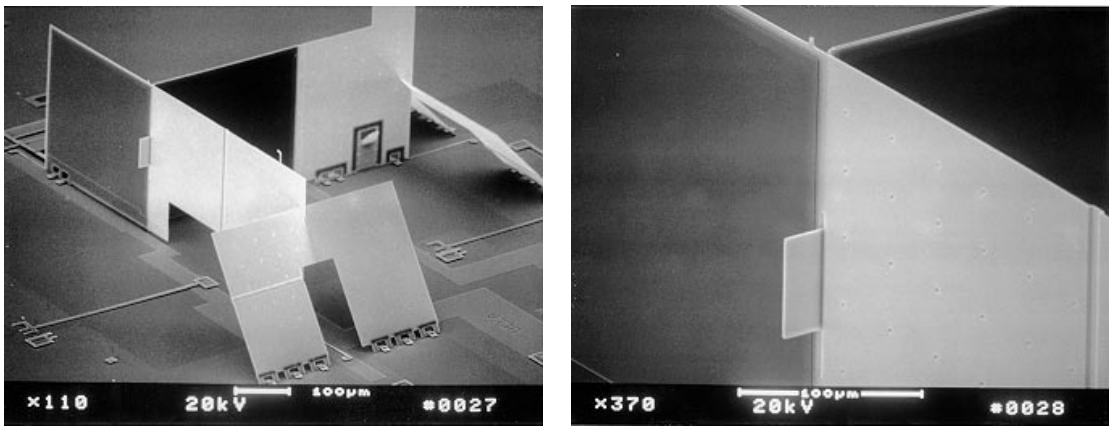

(a) (b)

Figure 3.11: Rear view of the CCR in Fig. 3.9 shows the mortise protruding through one of the mirror plates (a). The close-up view of the mortise and tenon are shown in (b).

that the CCR will be reflective only when it is actively transmitting data. When it is not transmitting data, it would rest passively in the background without being detected or being a noise source to other transmitting CCRs. This design goal may not be necessarily in all applications. Nevertheless, we included this requirement to make our CCR design more generally applicable.

We chose to use electrostatics for actuation for several reasons. Electrostatics offer large forces for short range of motions. With the MCNC process, electrostatic actuation is one of the most commonly used method of actuator. Thermal actuation can also be easily implemented with this process [16]; however, thermal actuators typically consume milli Watt of power, several order of magnitude higher compared to electrostatics. Magnetic[2, 28, 67, 45], piezo-electric, and other actuation methods may not necessarily consume high power but are clearly more difficult to implement with this process. Therefore, we focused our effort on designing electrostatic actuators.

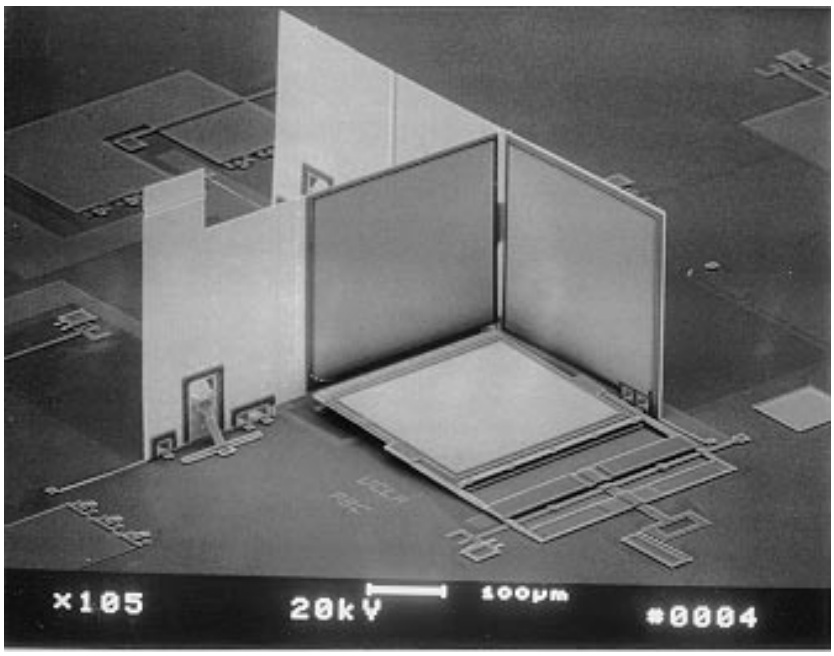

Figure 3.12: A micro CCR without the support of locking plates was shown to have worse alignment compared to the identical CCR in Fig. 3.9 which is fully supported.

Fig. 3.13 shows a design of an electrostatic CCR. This design is identical as the CCR shown in Fig. 3.8 with the addition of a movable base mirror. The movable mirror of the CCR in Fig. 3.13(a) is not yet assembled. To assemble the movable base mirror, the hinge mirror on the substrate is rotated about its microhinges by almost 180 to a position just a couple degrees from being parallel to the substrate. A metal contact on the lower part of the rotated plate comes in contact with another metal contact on the substrate such that a voltage can be applied to the rotated plate.

When a sufficiently large voltage is applied across the tilted mirror and the electrode which is located on the substrate just below the tilted mirror, the tilted mirror moves toward the substrate by bending the support beams and eventually

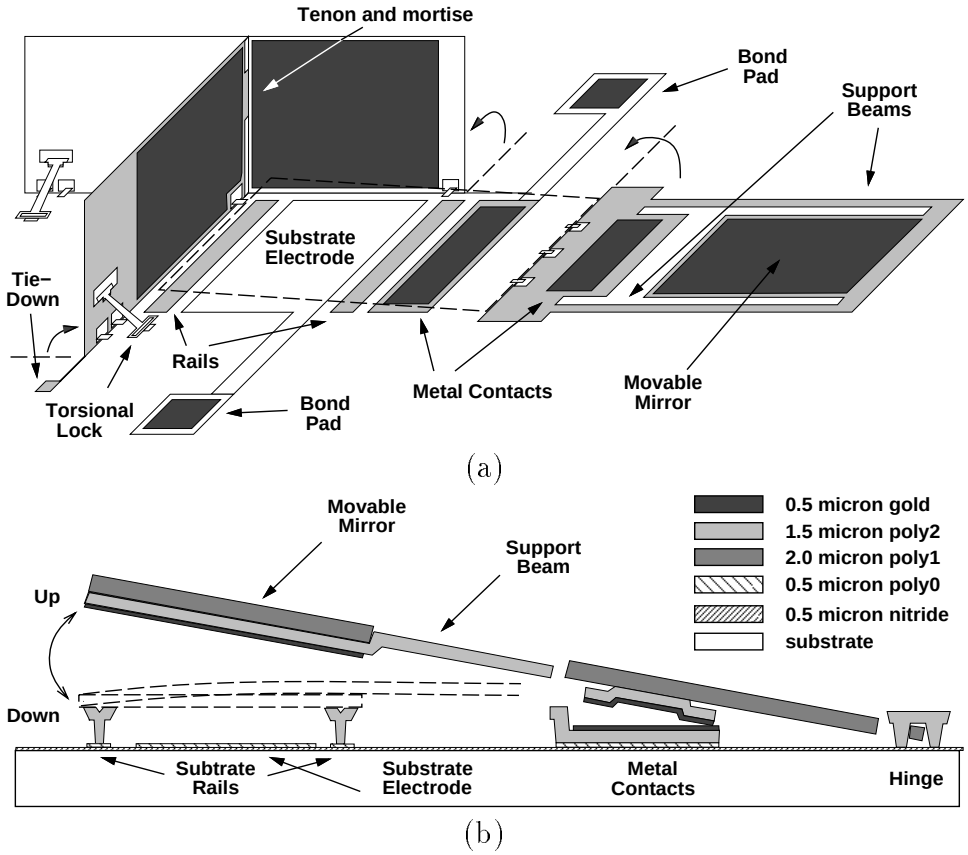

Figure 3.13: One design of an electrostatically actuated corner cube for MCNC's polysilicon process. (a)The base mirror of this CCR is formed by rotating a mirror plate to a tilted position above a substrate electrode. (b) The cross-section of the actuator shows how two rails on the substrate are used to help level the pulled-down mirror and to prevent short-circuiting across the actuator.

rests against two rails on the substrate. The substrate rails not only help leveling the pulled-down mirror but also prevent shorting between the conductive mirror and the substrate electrode. The cross-section drawing in Fig. 3.13(b) shows an assembled actuator moving the mirror from the angled to the horizontal "pulled-down" position.

A fabricated electrostatic CCR is shown in Fig. 3.14. To prevent the assembled mirror from coming apart, beams are added to clamp the mirror in place (Fig. 3.15).

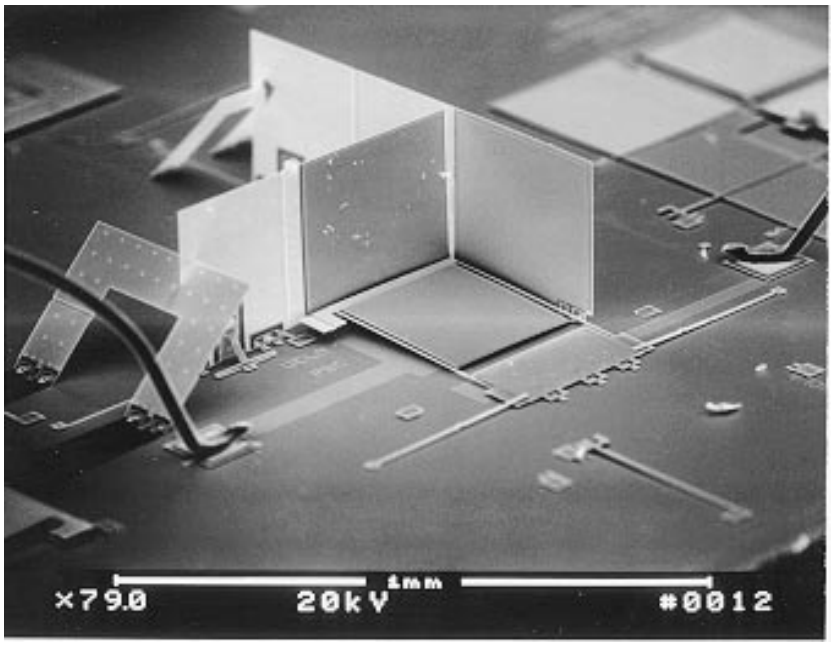

Figure 3.14: An electrostatically actuated polysilicon CCR with a $250\mu m$ corner. The motion of the bottom plate modulates the reflection from the corner. The plate as shown is in an "up" position (the CCR is off).

The locking beam must first be lifted up or pushed toward one side because the mirror plate should be rotated to the angled position. After the mirror plate is in place, the locking beam can then be released.

The flip-over actuated mirror design is functional but not ideal in several ways. The flip-over mirror has a polysilicon reflecting front surface instead of a metal surface. Even when a gold layer is placed on the unrotated plate (so that the rotated mirror would have a gold back surface) as shown in Fig. 3.13(a), significant optical power is lost in the polysilicon layer. Another problem with this design was that the mirrors were found to be difficult to assemble because of the 180 rotation requirement and the locking beam design. Therefore, the yield of these devices was low.

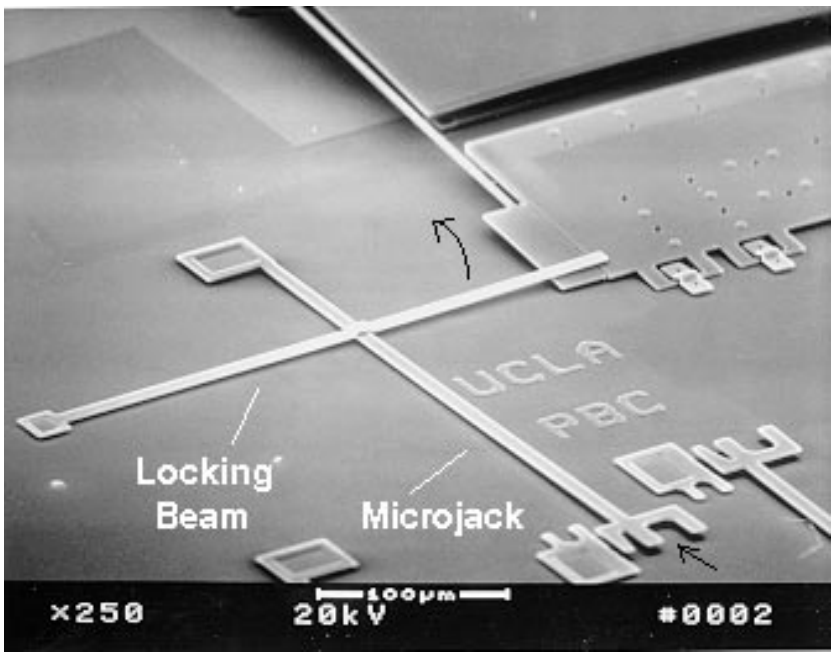

Figure 3.15: Bent beams are used to prevent the rotated mirror from being disassembled. To assemble the tilted mirror, a probe applies an axial force to buckle the microjack, lifting the locking beam, the mirror is then rotated into position (Fig. 3.13), and the locking beam is lowered.

Fig. 3.16 (a) shows an actuated mirror design with a gold reflective surface. It is formed by a suspended plate which is pried up to an angled position with a sliding plate. The cross-section diagram of the actuator in Fig. 3.16 (b) shows how the angle of the tilted mirror is determined by the thickness and position of the sliding plate. The sliding plate may be set against a fixed stopper so that the mirror is tilted to a precise angle. When the mirror is electrostatically attracted toward the substrate, it encounters and rests on two rails on the substrate to become orthogonal to the two vertical stationary mirrors.

Fig. 3.17 shows a fabricated actuator. It takes 3 steps to assemble this actuator: 1) pushing on a microjack which raises the mirror plate to an angle (details about microjacks are presented in Section 3.3.2; 2) setting the sliding plate underneath

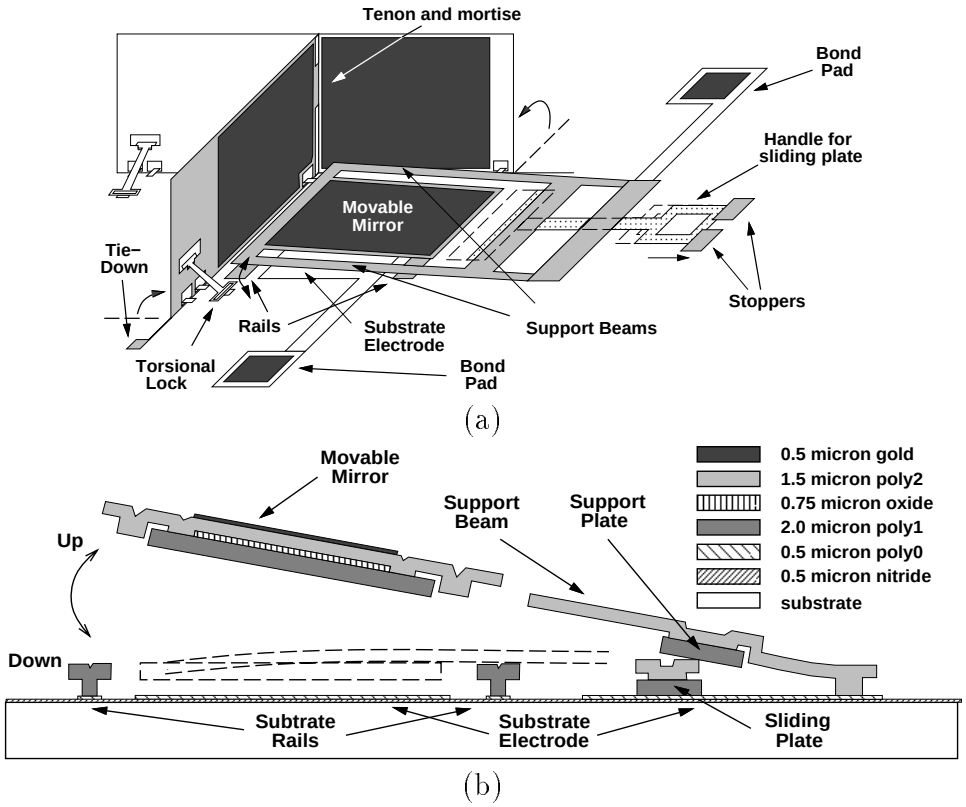

Figure 3.16: (a) The base mirror of this CCR, which has a gold front surface, is formed by a mirror plate which is pried up to an angled position. (b) The angle of the pried-up mirror is determined by the thickness and position of the sliding plate.

the base support plate of the mirror; and 3) releasing the microjack. This assemble process is indeed more simple than that of the other design since it only involves pushing and pulling, instead of lifting and rotating. Actuators with several support beam design variations were also fabricated as shown in Fig. 3.17 to achieve different actuation voltage and bandwidth.

The actuated mirror takes advantage of the nonlinearity and instability found in a typical spring-mass-electrostatic system such that the mirror can be pulled down with relatively low voltages. Typically, an actuation voltage of 10 to 20 volts

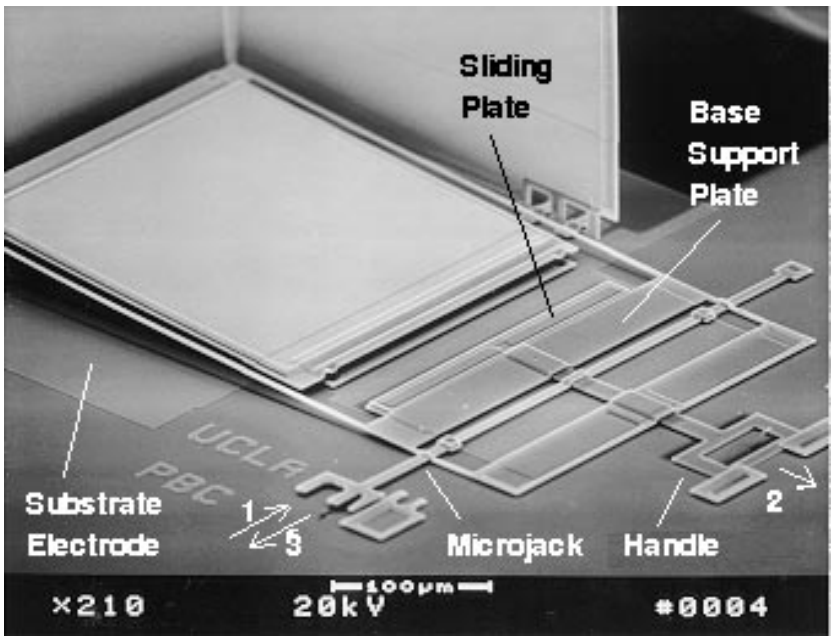

Figure 3.17: A movable mirror with a gold front surface is assembled by 1) pushing on the microjack, 2) pulling on the handle to move the sliding plate underneath the base support plate of the mirror, and 3) releasing the microjack. The tilted mirror is then actuated like the design in Fig. 3.13.

is adequate to move the tilted mirror (at about 2-3 degrees) to a flat position. Estimated capacitance of the electrostatic actuator is less than $0.3pF$. When the CCR is driven with 20 V and 10 kHz voltage input, the estimated power consumption of the actuator is therefore less than 0.6μW.

3.2 Analysis of Electrostatic Actuator

3.2.1 Modeling of the non-parallel plate actuator

In order to predict the behavior of the nonlinear mirror actuator shown in Fig. 3.13 and Fig. 3.16, a lumped-element model has been used to simulate the system (Fig. 3.19). This model assumes that the mirror is a rectangular rigid body with

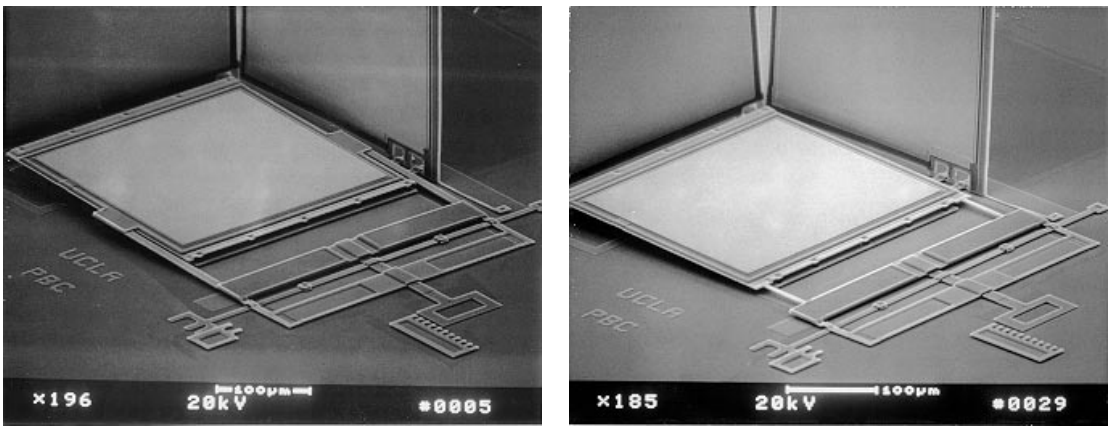

(a) (b)

Figure 3.18: Tilted movable mirrors with support beams attached (a) on opposite sides of the mirror and (b) at one end of the mirror.

width W, length L, thickness t, mass M_p and moment of inertia I_p given by

$$I_p = \frac{M_p}{12}(L^2 + t^2) + M_p(L - L_0)^2 \tag{3.49}$$

where L_0 is the distance between the axis of rotation and one edge of the plate to plate defined in Fig. 3.19. The axis of the rotation is defined by the support beam attachment points to the mirror. Note that the t^2 term in Eq. 3.49 is negligible because the mirror is a thin plate.

The support beams are modeled as fixed-end elastic straight beams, each with length l, width w, height h, and moment of inertia of beam cross-section I_b given by

$$I_b = \frac{w^3 h}{12}. \tag{3.50}$$

The forces and moments acting on the mirrors are generated by the electrostatic attraction between the mirror and the substrate electrode, the elastic beam supports, and squeeze-film damping.

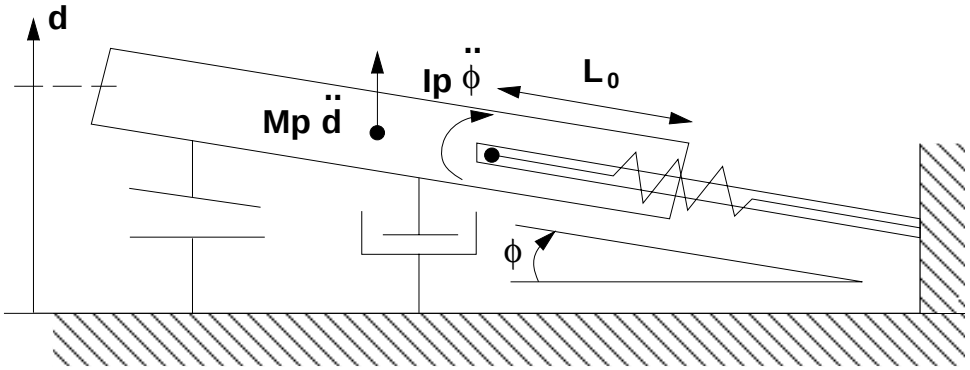

Figure 3.19: Lumped-element model for the electrostatic actuator.

Based on these assumptions, the system equation for the actuator in Fig. 3.14 is the following:

$$\begin{aligned}\begin{bmatrix} M_p\ddot{d} \\ I_p\ddot{\phi} \end{bmatrix} &= \frac{V^2}{2}\frac{\epsilon W}{|\phi|}\begin{bmatrix} -\frac{L}{\delta}\left(\frac{2\sin\frac{|\phi|}{2}}{\delta-2L\sin\frac{|\phi|}{2}}\right) \\ \frac{1}{2\sin\frac{|\phi|}{2}}\left(\ln\left(\frac{\delta}{\delta-2L\sin\frac{|\phi|}{2}}\right)-\frac{2L\sin\frac{|\phi|}{2}}{\delta-2L\sin\frac{|\phi|}{2}}\right)\end{bmatrix} \\ &+ \frac{EI}{l}\begin{bmatrix} \frac{12}{l^2} & -\frac{6}{l} \\ -\frac{6}{l} & 4 \end{bmatrix}\begin{bmatrix} d_0-d \\ \phi_0-\phi \end{bmatrix} \\ &- (1-0.6\frac{W}{L})(\frac{\mu W^3 L}{d^3})\begin{bmatrix} \dot{d} \\ (\frac{L}{2})^2\dot{\phi} \end{bmatrix} \end{aligned} \tag{3.51}$$

where for $\phi \geq 0$,

$$\delta = d \tag{3.52}$$

and for $\phi < 0$,

$$\delta = d + 2L\sin\frac{|\phi|}{2} \tag{3.53}$$

E, ϵ, and μ represent Young's modulus of polysilicon, permittivity of free space, and viscosity of air. Other variables are explained in Table 3.2. We will further explain the derivation of the equation in the rest of this section.

M_p	mass of mirror plate	1.25	μg
I_p	moment of inertia of mirror plate	3.26×10^{-17}	kgm^2
W	width of mirror plate	250	μm
L	length of mirror plate	280	μm
I_b	moment of area of beams	2.25×10^{-24}	m^4
l	length of support beams	370	μm
V	applied voltage	0-20	V
d	gap distance (at the beams attachment)	–	μm
ϕ	angle between the plate and the substrate	–	deg
d_0	initial gap distance	20-30	μm
ϕ_0	initial plate angle	2-4	deg

Table 3.2: Explanation of variables for the system equation

The electrostatic actuator is modeled as a non-parallel capacitor (Fig. 3.20). First, the electric field, E, is found by solving Laplace's equation in polar coordinates as a function of the radial distance, neglecting the effect of fringing field.

$$V = \int E \cdot ds = \int_0^{\phi} E(r)\, r\, d\theta \tag{3.54}$$

$$\Longrightarrow \quad E(r) = \frac{V}{\phi\, r}, \quad r_0 < r < r_0 + L; \tag{3.55}$$

The capacitance, C, is calculated using Gauss' law for electricity (Eq. 3.56.

$$q = \varepsilon_0 \oint E \cdot dA = \varepsilon_0 \int_{r_0}^{r_0+L} \int_0^{W} E(r)\, dz\, dr \tag{3.56}$$

$$\Longrightarrow \quad q = \frac{\varepsilon_0\, W}{\phi} \ln \frac{r_0 + L}{r_0}\, V \tag{3.57}$$

$$q = C\, V \quad \Longrightarrow \quad C = \frac{\varepsilon_0\, W}{\phi} \ln \frac{r_0 + L}{r_0} \tag{3.58}$$

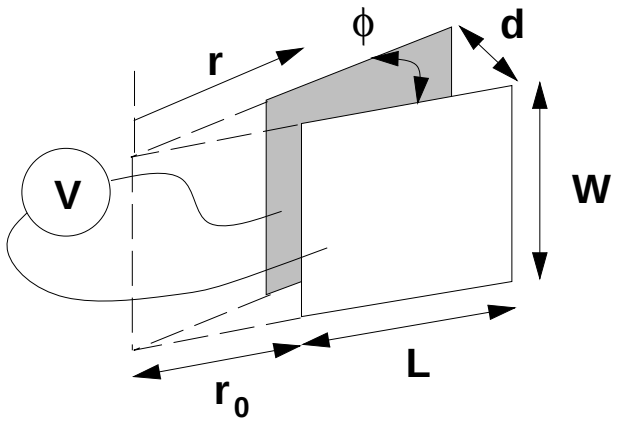

Figure 3.20: Illustration of a non-parallel plate capacitor.

C may be represented in terms of the displacement d (as defined by Fig. 3.20) by substituting r_0 in Eq. 3.58 with

$$r_0 = \frac{d}{2\sin\frac{\phi}{2}} - L. \tag{3.59}$$

It can be shown that the capacitance, C, for the non-parallel plates is equal to that for a parallel plates as ϕ goes to zero.

$$\lim_{\phi \to 0} C = \frac{\varepsilon_0 W L}{d} \tag{3.60}$$

The total energy, U, for the non-parallel plate capacitor is then calculated using Eq. 3.61.

$$U = \frac{1}{2} C V^2 \tag{3.61}$$

The force, F_e, applied to the support beams by the charged plates is calculated by taking a partial derivative of the total energy U with respect to the vertical separation.

$$F_e = \frac{\partial U}{\partial d} = \frac{1}{2}\frac{\partial C}{\partial d} V^2 \tag{3.62}$$

Therefore, F_e as a function of d, ϕ, and the plate dimensions is given by the following express:

$$F_e = -\frac{1}{2}\ V^2\ \frac{\varepsilon_0 W L}{d\ \phi}\left(\frac{2sin\frac{\phi}{2}}{d - 2Lsin\frac{\phi}{2}}\right) \tag{3.63}$$

It can be shown that the electrostatic force for the non-parallel plates is equal to that for the parallel plates as ϕ goes to zero.

$$\lim_{\phi \to 0} F_e = -\frac{1}{2}\ V^2 \frac{\varepsilon_0\, W\, L}{d^2} \tag{3.64}$$

We assume that this electrostatic force, F_e, is directly applied to the tips of the support beams.

The electrostatic moment, M_e, applied to the support beams by the actuated mirror is more critically dependent on the location where the beams and the mirror are connected. At this location lies the axis of rotation for the mirror. This moment can be calculated by summing the product of the electrostatic force due to a differential area, F_e', and the corresponding distances from the areas to the axis of rotation.

The electrostatic force due to a differential area, F_e', is defined by

$$F_e = \int_{r_0}^{r_0+L} F_e'(r)dr. \tag{3.65}$$

r is defined in Fig. 3.20. By expressing F_e in terms of r_0 instead of d in Eq. 3.63, we can define F_e' as the following:

$$F_e'(r)dr = \lim_{\delta L \to 0, r_0 \to r} F_e(r_0, L) \tag{3.66}$$

Therefore, the electrostatic moment generated by the plate, M_e, as a function of the beam attachment location characterized by L_0 (Fig. 3.19) is defined by the

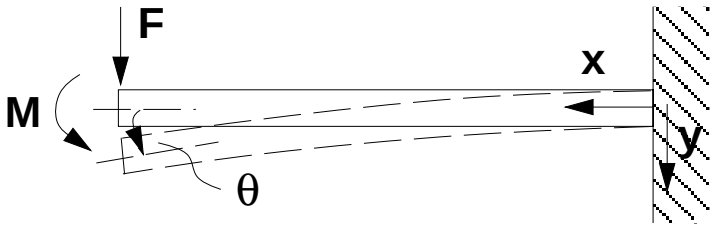

Figure 3.21: Illustration of an elastic beam with one fixed end and one free end.

following integral:

$$M_e = \int_{r_0}^{r_0+L} (L_0 + r_0 - r) F_e'(r) dr \tag{3.67}$$

Therefore, M_e is given by

$$M_e = -\frac{1}{2}\, V^2\, \frac{\varepsilon_0 W}{2\phi \sin\frac{\phi}{2}} \left(\ln\left(\frac{r_0 + L}{r_0}\right) - \frac{L(r_0 + L_0)}{r_0(r_0 + L)} \right) \tag{3.68}$$

L_0 is equal to L, $L/3$, and 0 for the design in Fig. 3.17, Fig. 3.18(a), and Fig. 3.18(b) respectively. The expression for r_0 (Eq. 3.59) can be substituted in Eq. 3.68 to represent M_e in terms of d and ϕ. The complete expressions of the electrostatic force and moment for $L_0 = L$ are shown as the first terms on the right side of the system equation (Eq. 3.51).

The two support beams of the actuated mirror are modeled as ideal linear rectangular beams with one free-end and one fixed-end (Fig. 3.21). The elastic curve of the beam is defined by

$$EI\frac{d^2y}{dx^2} = M(x) \tag{3.69}$$

where M(x) is bending moment along the beam [100]. With a force F and moment M load at the tip of the free end, the slope θ and the deflection y at the tip are defined by the following expressions:

$$\theta = \frac{l}{EI}M + \frac{l^2}{2EI}F \tag{3.70}$$

$$y = \frac{l^2}{2EI}M + \frac{l^3}{3EI}F \tag{3.71}$$

Since the support beams and the mirror are connected, θ and y are coupled to the position and angle of the mirror. When the mirror moves, the beams become bent and in return exert a force and moment onto the mirror. The spring force and moment expressions, derived from Eq. 3.70 and Eq. 3.71, are shown as the second term on the right side of the system equation for the case where $L_0 = L$ (Eq. 3.51). The original θ and y of the beams are represented in d and ϕ based on the coordinate system of the mirror (Fig. 3.19).

The damping force in the system is approximated by squeeze-film damping for parallel-plates [88, 4], and the damping moment is calculated by multiplying the damping force by the distance from the center of the mirror to the axis of rotation. The damping expressions are shown as the last term of the right side of the system equation.

The system equation in Eq. 3.51 describes the mirror's motion only when the mirror is not in contact with any rails on the substrate. Ideally, the mirror will contact both rails at the same time and then come to a full stop at the rails very quickly. We would like to design such a movable mirror. On the other hand, if the mirror happens to collide with one of the rails before the other one, the subsequent motion of the mirror would require a more complex model. For example, the mirror must no longer be modeled as a simple point mass. The compliance of the mirror and the rails also need to be taken into account. Nevertheless, this simple model is still useful for estimating the static positions, pull-down and release dynamics of a near-ideal actuated mirror.

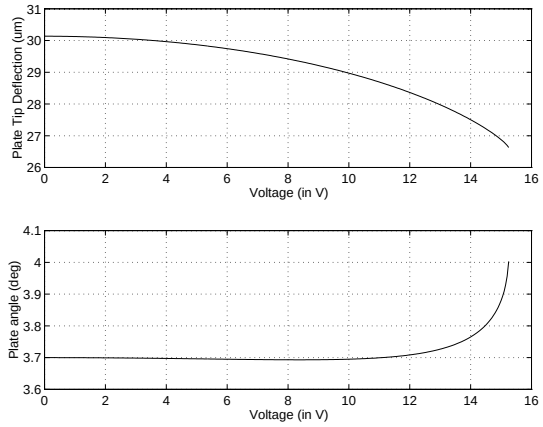

Figure 3.22: Simulated deflection and angle of the actuated mirror in Fig. 3.13 as a function of input voltages is shown. Simulated pull-in voltage is $15.3V$.

3.2.2 Simulation of the actuator

The system equation, Eq. 3.51, is simulated with Matlab using Simulink and the Runge-Kutta fifth order method.

The model predicts a voltage at which the electrostatic force will overcome the spring force, as seen in parallel-plate electrostatic systems [13]. Fig. 3.22 shows the simulated equilibrium positions of an actuator with voltage input from 0 to the predicted pull-in voltage of 15.3 V. The predicted voltage agrees well with experimentally observed pull-in voltages for this actuator, which cluster around 15 V. The increase in plate angle when the applied voltage approaches 15V suggests that the unsupported mirror edge will first collide with a rail during a pull-down. This effect has also been observed.

Fig. 3.23 shows the simulated motion of the plate from a "pull-down" position to an idle position with no applied voltage. The natural frequency of the actuator is simulated to be 550Hz.

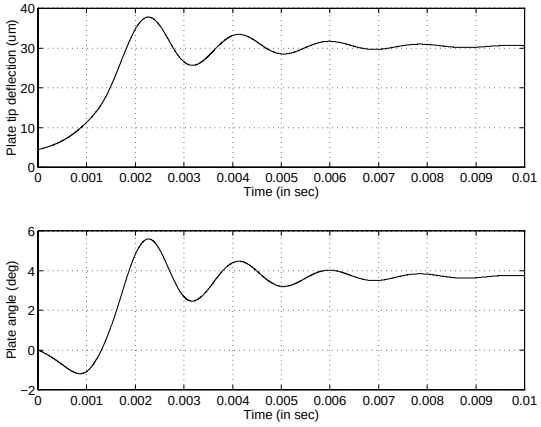

Figure 3.23: Simulated positions of the actuated mirror in Fig. 3.13 as it goes from the "down" position to the "up" position.

3.3 Fabrication of micro CCRs

Layout of the CCR designs are electronically submitted to MCNC for fabrication. Generally, MCNC will fabricate and deliver the 15 chips within about 3 months. MCNC offers services of release etching, packaging, and bonding. To take advantage of these services, the design must follow strict etch hole design rules so that the chips may be properly released. In our case, our CCR designs have large plates (with dimensions of $300\mu m$) which do not have etch holes (Section 3.1.2). Since these designs do not follow the etch hole design rules, we do not request MCNC's etching or bonding services. Instead, we requested un-post-processed chips from MCNC. These chips are coated with protective photoresist and the polysilicon layers are still encased in the sacrificial oxide layers. To create CCRs, these chips must be further processed including wet etching and micro-assembly.

3.3.1 Post-processing of MCNC chips

The MCNC chips were first soaked in acetone in order to remove the protective photoresist layer. Generally a 15 minute soak in acetone and then a quick rinse in isopropanol would adequately remove the photoresist layer for a successful sacrificial release etch. All the rinses were done at room temperature. Unfortunately, small spots of photoresist scum or residue were often found on the gold surfaces and the chips tended to exhibit stiction. Best results were found by extending the 15 minute soak to 30 minutes and soaking the chips in an ultra-sonic bath, followed by a 5 minute isopropanol dip. The chips were then transfered to a fresh bath of isopropanol before the sacrificial oxide etch.

In order to release the structural polysilicon layers, the chips must be etched in hydrofluoric acid (HF) to remove the sacrificial oxide layers. MCNC uses phosphosilicate glass (PSG) deposited by LPCVD as the sacrificial oxide. The etch rate of the MCNC MUMPS' PSG in room temperature 49% HF is about $10\mu m/min$. Since our designs had large plates with no etch hole, the acid must undercut distances of up to $150\mu m$ of PSG in some areas. Therefore, we etched our MCNC chips in room temperature 49% HF for up to 15 minutes in order to release for all the polysilicon plates. The chips were etched with essentially no agitation to avoid damaging any released or partially released plates. 49% HF is reported to show near zero etch rate for polysilicon and slow etch rate for low-stress nitride [97]. The 15min long etch generally did not cause any observable effect on the gold or polysilicon layers.

Following the HF etch, the chips were carefully taken out the HF bath and immediately placed in DI water for a 5 minute rinse, followed by an isopropanol rinse for another 5 to 10 minutes. Again, minimal agitation was applied to prevent

damage to the released structures. Finally, the chips were either dried on a 105^o hot plate for 2 minutes or baked in a 120^o oven for 20 minutes.

Using isopropanol as a final rinse chemical is beneficial because its low surface-tension reduces the capillary force which often causes beams or plates to become adhered to the substrate during drying. Although there are many other release procedures such as supercritical-liquid carbon dioxide drying [72], self-assembled monolayer (SAM) anti-stiction film coatings [36, 87], and vapor-phase HF etching [59] which were shown to provide better release results in terms of minimizing stiction [48], we found that the simple alcohol release method which we used was able to provide adequate results for our designs.

Depending on the method of packaging, the $1cm^2$ may be diced into several dozen diced pieces. Dicing must be carried out before the wet release process because the debris generated during the dicing process could easily damage the released MEMS structures. The chips were diced at the UCLA Center of High Frequency Electronics, and all the wet processing was conducted at the UCLA Nanoelectronics Research Facility. The $1cm^2$ chips were generally easy to handle; however the small $3mm^2$ diced pieces required special attention since it was easy to scratch the chips with the tweezers. The small chips could also easily turn upside down and damage the poly structures.

3.3.2 Manual assembly of micro CCRs

All the polysilicon CCRs presented in Section 3.1 are manually assembled using micro-manipulators at a probe station with a microscope. A microscope with a total magnification of about 100 is generally adequate for assembly; however, long distance objectives are necessary to allow the probe tips to reach the structures

on the chip. Probe tips with tip diameters of $12\mu m$ were found to be best since they are sharp but not too fragile. Probe tips which are too sharp could actually cause problems such as getting caught by the etch holes on the plates or piercing holes through the plates. In general, two micro manipulators are sufficient for assembling the designs presented in this work.

The assembly process of a micro corner cube like the ones in Fig. 3.9 and 3.14 includes assembling the movable base mirror and lifting and rotating four plates – two plates which form the two vertical mirrors and two which serve as additional alignment aides. Assembling the different designs of movable base mirrors was already briefly discussed in Section 3.1.4. For example, the assembly procedure for the movable mirror in Fig. 3.17 was relatively straight forward – only pushing and sliding are involved. The probe tip must be lowered to the surface of the substrate and then moved along the substrate. To assemble the movable mirror in Fig. 3.14 or the other vertical mirrors, released plates must be lift up and rotated about their hinges. The required steps are more difficult to carry out.

To lift and rotate a plate about some hinges, one must place a probe tip underneath the plate. Once the probe tip is underneath a plate, it must be raised up from the substrate while keeping in contact with the plate until the plate is latched up by a lock or is resting on other structures. Depending on the design of the hinged plate, the edge of the plate may lie flat on substrate or have a gap of up to $2.75\mu m$ above the substrate. Sliding a sharp probe tip underneath the plate may be relatively easy. Unfortunately, in some cases, friction between the probe tip and the plate may cause the free plate to slit on the substrate such that hinge pins are pushed against the staple and break. In other cases, stiction or adhesion between the released plate and the substrate may cause the plate to

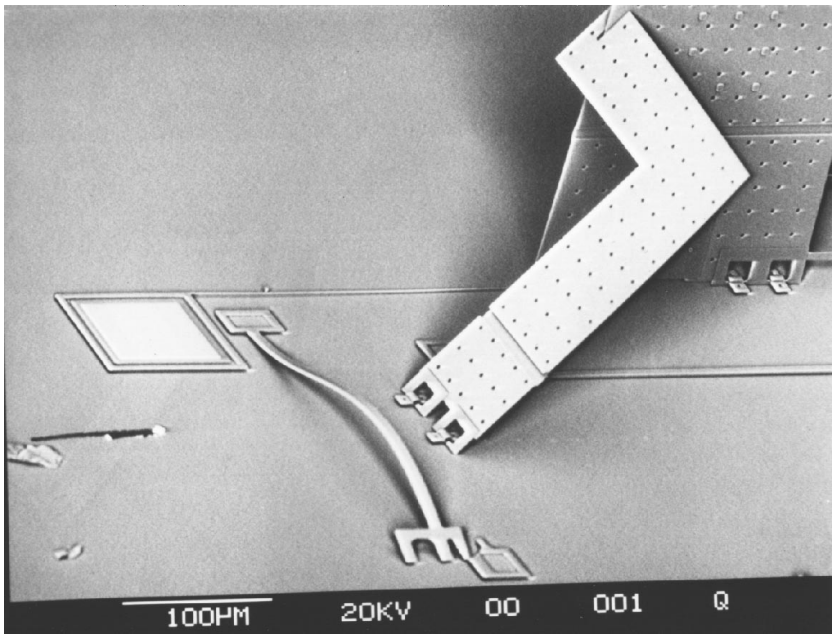

Figure 3.24: A micro jack is resting on the substrate in a buckled shape. Microjacks can be used to raise up a hinge plate slightly so that sliding a probe tip underneath the plate becomes much easier.

become "stuck" to the substrate such that it becomes extremely difficult to slide a probe tip underneath the plate.

In order to facilitate micro assembly, particularly in situations described above, microjacks are used to raise the released plates so that probe tips can easily be placed underneath the plates [13]. Microjacks, usually made of $Ply1$, are long beams with one free end and one fixed end. When compressed axially from the free end, the microjack will buckle (Fig. 3.24). When a microjack is placed underneath a $Ply2$ plate, it may be used to raise the edge of the plate by ten's of microns so that placing a probe tip underneath the plate becomes trivial. With the aid of a microjack, lifting and locking a hinged plate may take as little as a few seconds.

For the CCRs designed in this work, the different mirror plates and locking plates must be assembled in a specific sequence: the mirror plate with the mortise

or alignment stub must be locked into position before the other vertical mirror plates. The two locking plates can be rotated to their final position as long as the corresponding mirror plates are already in place. The movable mirror may be assembled before or after the assembly of the vertical mirrors.

The ease and yield of manually assembled micro CCRs largely depends on the release-etch process. If the chip is properly released and rinsed such that the substrate is free from scum and minimal stiction is present, assembly of a CCR may take 3 to 4 minutes with a yield of at least 90%. When stiction is present, more care is required to assemble a CCR. As a result, the assembly process takes 10 to 15 minutes. The yield may be reduced to 50% when a lot of stiction is present. In these cases, the microjack may break while trying to pry up the plate which is stuck to the substrate. Subsequently, only careful manipulation of the probe tips can lift up the plate. Therefore, a reliable release-etch process such as the one described earlier is crucial for the realization of these microstructures.

3.3.3 Self-assembled micro CCRs

The micro CCRs which have been presented have been designed for manual assembly. For mass production, automation of the assembly process would likely lead to lower cost and higher yield. Since a well-defined sequence of steps is needed to assemble a micro CCR, in principle, they can also be automatically assembled using programmable micro-manipulators. A micro-manipulator could be programmed to push against a microjack, then another manipulator would lift up the raised-up plate and move it to a known position where the plate will become locked. Although such automation would not be too difficult to implement, an assembly system with complex hardware may be required. Furthermore, each design

variation with plate size or beam stiffness may require a unique program unless sophisticated force feedback and image processing are used. In a more ideally situation, CCRs should be designed to self-assemble when some external energy is applied.

Hinged structures have been demonstrated to self-assemble in water where the motion of agitated water pushes the released hinged plates with integrated locks and causes them to become locked [9]. Since our CCR designs require a sequence of assembly steps, assembly by random water motion is very difficult. A number of microstructures with integrated micro actuators for self-assembly were reported. Actuators which may be used for assembly include linear stepper motors or inch worm motors [99, 92], vibromotors [19], thermal actuator arrays [16], and scratch-drive actuator arrays [3, 55]. In this work, we have also attempted to integrate micro actuators with CCRs so that the CCRs may self-assemble when they are supplied with the appropriate voltage signals.

We chose the scratch drive actuator (SDA) for its large force output (up to 100's of μN), its ability to achieve long range of motion (100's of μm of distance), and most importantly, its simple design (simple to layout). Like many MEMS actuators, large voltage (60 to $120V$) is required to actuate SDAs . However, this is not a significant concern since this micro-assembly needs to be performed only once and the voltage requirement does not affect the actual performance of the devices during normal operation. Cost of supplying large voltage for the one-time-only assembly process is also negligible.

Fig. 3.25 shows an array of 6 SDAs which has rotated up a plate through some mechanical couplings. These structures also fabricated by MCNC. Each scratch drive actuator in the array is a small rectangular plate (50 to $100\mu m$ in length)

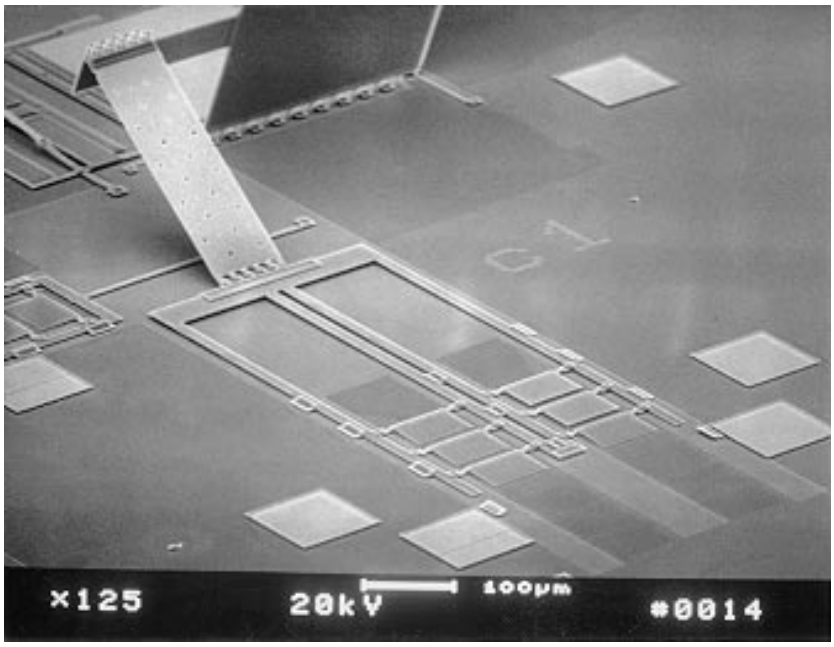

Figure 3.25: An array of 6 SDAs have rotated up a plate (near the top) using mechanical couplings including plates and scissor-hinges (Fig. 3.27).

and a bushing at one end, forming an L-shaped cross-section. Fig. 3.26 shows a close-up drawing of one of the SDAs in the array. The actuators are connected to several movable but guided rails on a conductive plane. The guided rails provide mechanical linkage for the actuators so that the forces generated by the actuators are summed. The rails also serve as electrical connection from the conductive plane to the actuators.

When a positive square waveform is applied between the conductive rails and the substrate, the actuator becomes attracted to the substrate and experiences a cycle of deformation and motion: the plate is pulled toward the insulating plane, becomes elastically deformed, then slides forward in the direction of the bushing as it is released for the substrate, and finally returns to its initial shape (Fig. 3.26). In each cycle, the actuator moves forward only a fraction of a micron (about

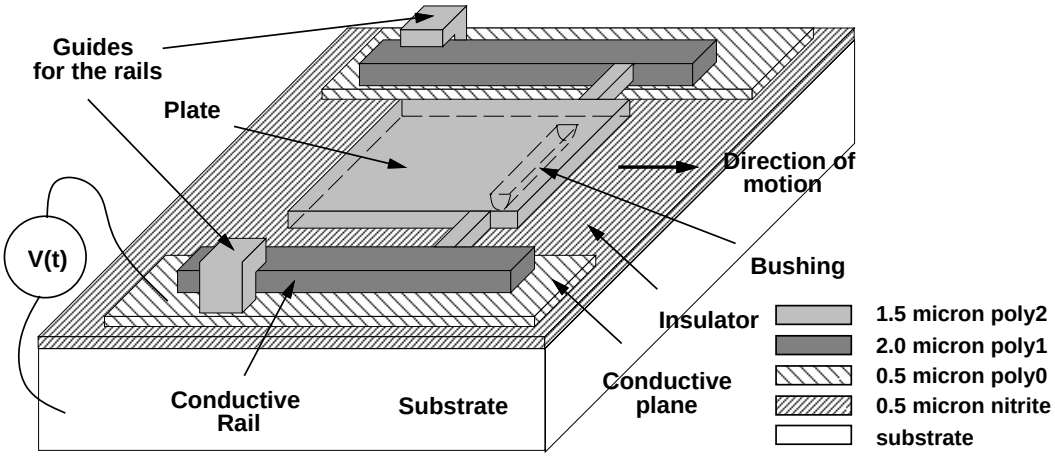

Figure 3.26: A close-up drawing of a scratch drive actuator in the actuator arrays in Fig. 3.25).

$0.01\mu m$[64]); however, with a bandwidth in the tens of kilo-Hertz range, the actuators can travel hundred of microns in a few seconds depending on the input voltage frequency.

In MCNC MUMPS process, the rectangular plate may be made of the $Ply1$ layer, and the bushing may be created with the dimple layer, which is a 0.5 micron partial etch on the Ox-1 layer. The $0.5\mu m$ nitride layer forms the insulating layer while the $Ply0$ forms the conductive plane on which the conductive rails rest. MCNC does not offer the option to pattern the nitride layer. Therefore, to create electrical contact to the substrate, one may stack the holes layers of $Ox1$ and $Ox2$ (known as $Anchor1$ and $Anchor2$) together such that the over-etch would etch through the nitride layer. As a result, the $Ply2$ and gold layers may be electrically connected to the substrate.

The SDA array in Fig. 3.25 is mechanically coupled to a hinged plate using plates and scissor hinges so that the linear motion of the array is translated into rotation of the hinged plate. Scissor hinges are made of interconnected fingers of

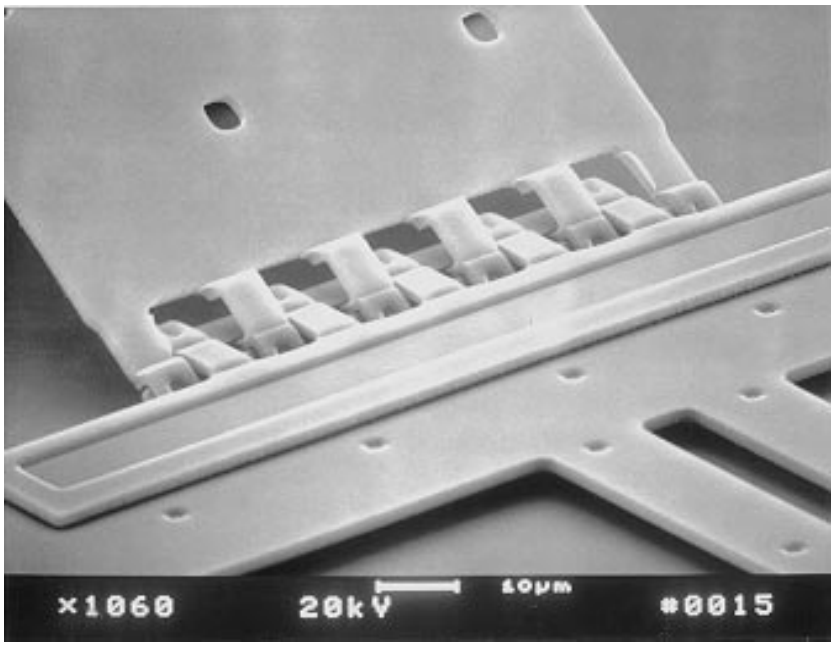

Figure 3.27: A close-up view of the scissor-hinges which connects the horizontal sliding plate to the angled plate.

polysilicon which allows plates to rotate with respect to each other [99]. Fig. 3.27 shows the scissor hinge joint which connects the horizontal sliding plate to the angled plate in Fig. 3.25.

A mechanical stopper can be integrated into the conductive rails so that the SDA array will travel a precise distance and then stop. The SDA array in Fig. 3.25 has traveled a distance of about $200\mu m$. The close-up view of the actuator array in Fig. 3.28(a) reveals that the array can no long move forward because its integrated stopper is already pushing against on the center rail guider. In contrast, the actuator array in Fig. 3.28(b) whose stopper has been physically removed was able move further forward as shown. The stopping position is then dependent on when the input voltage is turned off. With the stopper, the stopping position of the array is well defined; therefore, the hinged plate can also be rotated to a precise

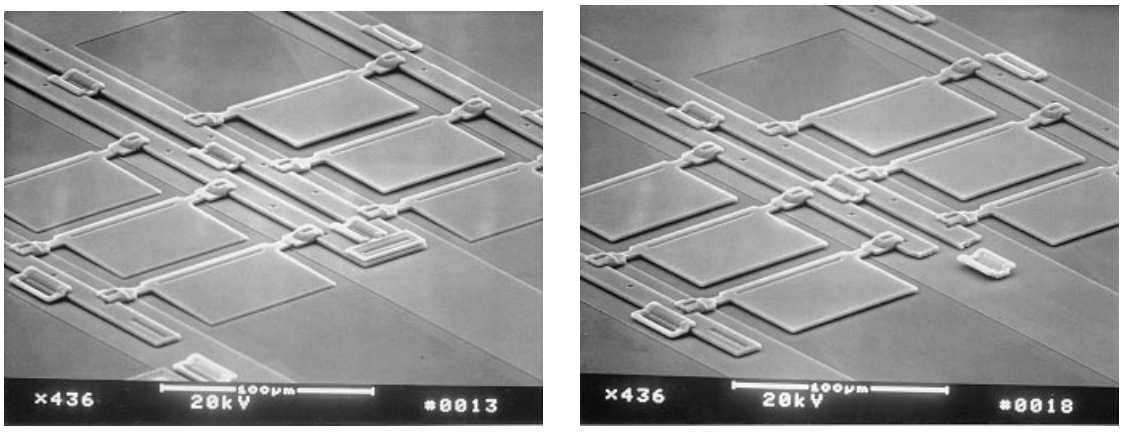

(a) (b)

Figure 3.28: Close-up views of the SDA array from Fig. 3.25 are shown in (a) with a mechanical stopper and (b) with the mechanical stopper removed. The array in (b) has moved about $60\mu m$ further than the one in (a).

angle.

Fig. 3.29 shows a self-assembled CCR with integrated SDA. The structure also has integrated tie-downs, mortise, and tenon for alignment like the manually assembled CCRs. Unfortunately, the CCR as shown was not fully assembled because the stoppers were placed at the incorrect position so that the SDA array's travel was limited. Although the mirrors of this particular CCR were rotated up by the SDAs, many other mirrors require an initial lift with a probe tip. The reason is that the mirrors, which have the same voltage potential as the SDA, become attracted to the substrate just like the SDAs. This problem, however, can be completely eliminated by adding a $Ply0$ plane underneath each mirror, similar to the conductive $Ply0$ plane underneath the movable rails.

The stoppers which limit the travel of the SDA arrays in Fig. 3.29 were carefully removed with a probe tip, the CCR was able to assemble completely, as shown in Fig. 3.30. The two mirror plates and the locking plate are assembled in sequence,

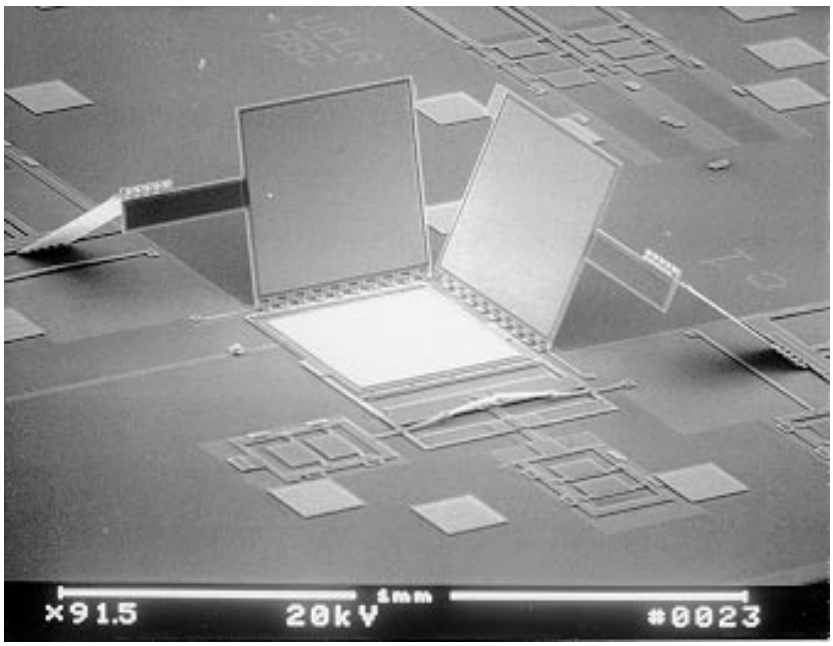

Figure 3.29: A CCR which was not able to self-assemble completely because of incorrectly designed stoppers.

just like the manually-assembled CCRs. This structure, however, was found to have come apart during the SEM process as shown in Fig. 3.31, suggesting that additional locking mechanism is needed.

Fig. 3.32 shows the rear views of two CCRs, one with an unassembled locking plate which is resting on the substrate, and one with an assembled locking plate which is pushing against one of the vertical mirror plates. The design of the mechanical coupling for the locking plate is slightly different from that for the mirror plates because the locking plate must rotate for more than 90 degrees. The locking plate successfully to the desired angle; however, one of the coupling plate was found to be too short so that the conductive rails began to curve up as the actuator moved forward. This problem can be corrected by increasing the length of the coupling plate.

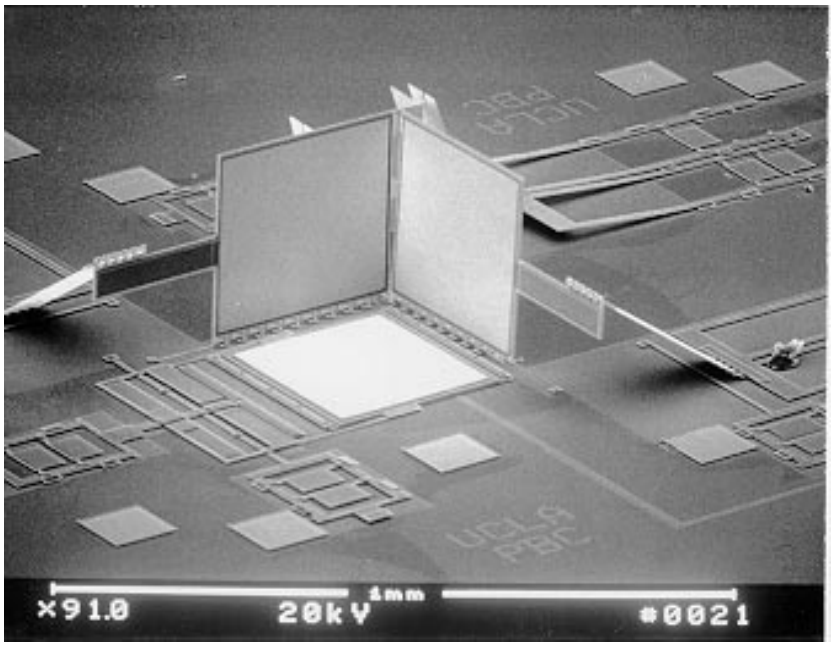

Figure 3.30: A CCR which was not able to self-assemble completely because of incorrectly designed stoppers.

Auto-assembly of the actuator was not successful for the fabricated designs. As shown in Fig. 3.29, the SDA array connected to a microjack was able to cause the microjack to arch – this microjack remained in this position probably due to fraction. In practice, when the SDA were driven, the microjack would even arch more dramatically. Unfortunately, the microjack could not raise up the base mirror. The reason is that parts of the movable mirror such as the support beams and the edges of the mirror were not resting on the conducting $Ply0$ plane. Therefore, the mirror was strongly attracted to the substrate when the SDA were driven, preventing the assembly of the structure. This problem can also be corrected by properly designing the $Ply0$ conductive plane.

The fabricated self-assembled CCR test structures had numerous problems due

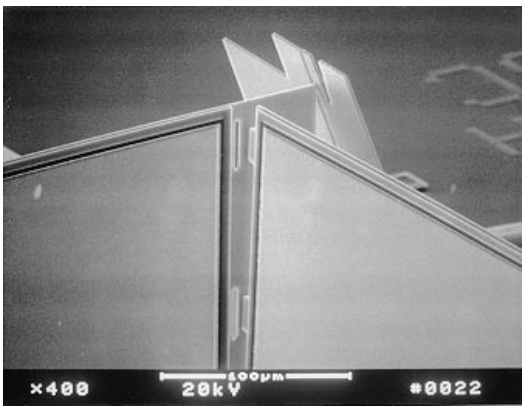

Figure 3.31: A close-up view of the CCR shows that the CCR came apart during the SEM process. Tenons and mortises were integrated for alignment, although they were not properly engaged in this case.

to design errors. Nevertheless, it is evident from the results from these test structures that fully self-assembled CCRs are realizable. Scratch-drive actuators were found to be suitable for self-assembly, although the required die area for these designs was doubled compared to that of self-assembled one. The challenge, therefore, is to design self-assembled CCRs which are compact in size with high yield so that the cost per CCR may be minimized.

3.3.4 Packaging of micro CCRs

The devices may be assembled before or after the chips were packaged and bonded. All the bonding was either carried out in the UCLA Center of High Frequency Electronics or the UCLA EE115AL Laboratory. In the earlier development stage, the devices were usually assembled before bonding because the assembly yield was low. Unfortunately, the bonding process often destroyed the assembled device due to poor handling of the chips. Otherwise, the exact sequence of assembly and bonding were not critical. Unbonded devices were occasionally tested by applying

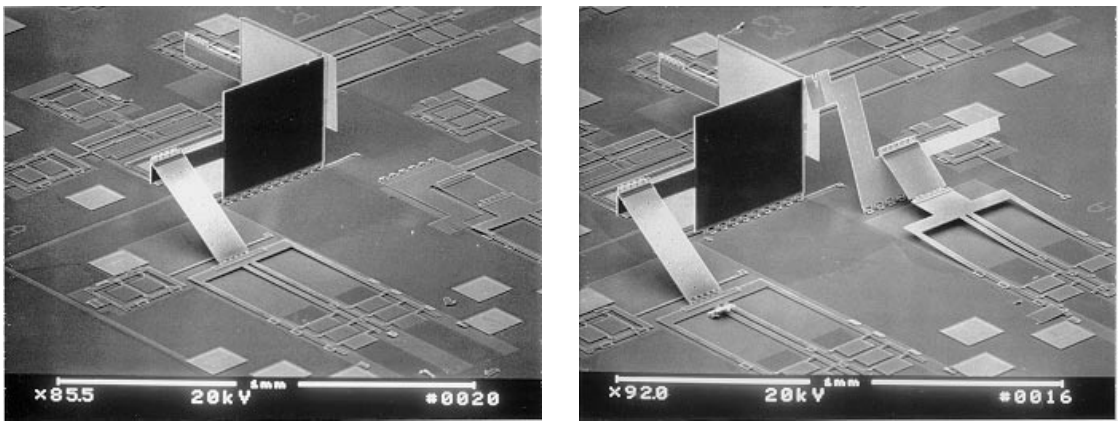

(a) (b)

Figure 3.32: Rear view of a self-assembled CCR (a) with an unassembled locking plate on the substrate and (b) with an assembled locking plate.

electrical signals to the devices through the micro-manipulators and observing the motion of the mirrors through the microscope. More robust testing, however, required the chips to be bonded.

For the undiced $1cm^2$ chips, each chip was attached to a custom-made glass substrate with copper pads. These small substrates were made from copper plated PC boards etched in sulfuric acid which were cut into small squares. In order to keep the microstructures safe and clean, each substrate was housed in a transparent plastic case. An example of a packaged chip is shown in Fig. 3.33(a). Depending on the application or test, the lid may be opened to improve the reflectivity of the device. For the full size chips, standard IC packages were available. However, these packages were generally too large for mounting on the optical mounts in our test bench and therefore not used.

Some of the MCNC chips were diced into small pieces with only one CCR per piece. In this case, standard 8-pin dip-packages were used instead of the custom-made glass substrates. Since the dip packages were easier to handle, they may

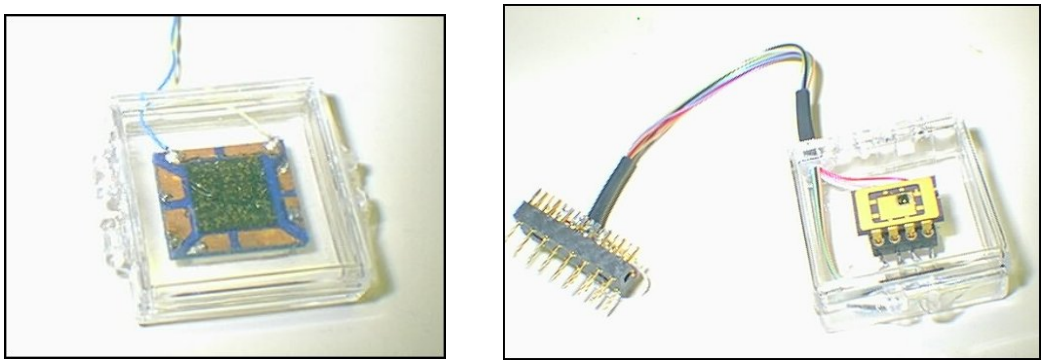

(a) (b)

Figure 3.33: (a) A bonded MCNC chip on a glass substrate inside a plastic case. (b) A single CCR in a 8-pin dip package inside a plastic case.

be directly plugged into a breadboard or socket for testing. Nevertheless, these packages usually were also housed inside a plastic case as shown in Fig. 3.33(b). We had also made cover lids for these dip packages using $150\mu m$ thick microscope glass covers. Because of the thickness of the glass covers, it was easy to cut the glass covers into the appropriate sizes with a sharp blade. The glass lid is either glued or taped onto the dip package.

Although the plastic cases and glass lids prevented general physical damages to the devices, they were not ideal solutions for various reasons. For example, a plastic lid has a transmittance of about 86% (at 45 degree incident angle) but the transmitted light beam is often distorted. The glass lid has an equal value of transmittance without causing distortion. However, since the interrogating light must pass through a lid twice before reaching the detector, the lid causes a net 26% decrease in received power. Aside from poor optical qualities, these packages were definitely not robust enough for harsh climate or environment. Further work is required to develop a packaging scheme which minimizes optical distortion and prevents the devices from physical damages due to debris, gust, and moisture.

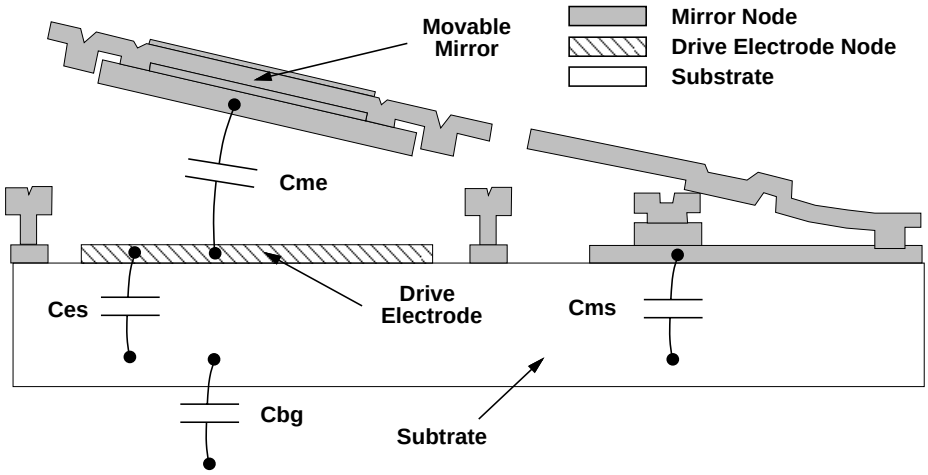

Figure 3.34: Drawing of the different capacitances associated with a micro CCR.

3.3.5 Capacitance testing of packaged CCRs

Four main capacitances are associated with a CCR actuator. Shown in Fig. 3.34 is a block diagram which explains these capacitances. The four capacitances are C_{es}, the capacitance between the drive electrode and the substrate, C_{ms}, the capacitance between the movable mirror and the substrate, C_{me}, the capacitance between the movable mirror and the electrode, and finally C_{bg}, the capacitance between the substrate and the environment. The substrate includes the silicon chip substrate as well as the package to which the substrate may be electrically connected.

In order to determine the values of the capacitances, we used an oscillation circuit whose frequency output is a function of an input capacitor (Fig. 3.35). A simple oscillation circuit was built using a 555 chip, whose frequency output is given by:

$$freq = \frac{K_0}{K_1 + C_{test}} \tag{3.72}$$

To estimate the circuit constants K_0 and K_1, 35 5% capacitors with values ranging from $0.22\mu F$ to $0.1\mu F$ were connected to the oscillation circuit. The measure

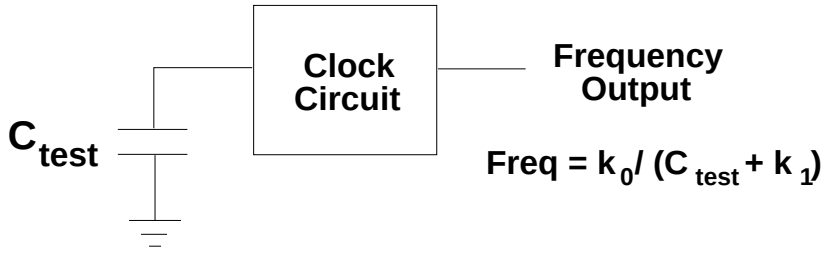

Figure 3.35: Block diagram of the capacitance test setup.

C_{in}	GND	C_{test}
Substrate	Mirror, Drive electrode	$C_{test_1} = C_{es} + C_{ms} + C_{bg}$
Mirror	Substrate, Drive electrode	$C_{test_2} = C_{me} + C_{ms} + C_{bg}$
Drive electrode	Substrate, Mirror	$C_{test_3} = C_{me} + C_{es} + C_{bg}$
All 3 nodes	(Not connected)	$C_{test_4} = C_{bg}$

Table 3.3: Explanations for the measured CCR capacitances using an oscillation circuit.

output frequencies and the corresponding known capacitor values were then used to compute the best fit values of K_0 and K_1.

After the circuit was well characterized, different CCRs were connected to the circuit and tested as capacitors. 4 different frequency measurements were taken for each CCR by grounding different combinations of the three CCR nodes. For example, by electrically connecting the substrate to the circuit and grounding the drive electrode and the mirror nodes, C_{test} would equal to the sum of C_{es}, C_{ms}, and C_{bg}. The four different possible "test" capacitances corresponding to the 4 different measured frequencies are given in Table 3.3.

The four measured frequencies for each CCR were used to determine the four "test" capacitances, which were then used to solve for the four unknown capacitances C_{es}, C_{ms}, C_{me}, and C_{bg}. Theoretical estimates based on the layout geometries are compared with the experimental results in Table 3.4 for a CCR. For C_{es} and C_{ms}, theoretical estimates assume that $C = \epsilon A/d$ where d is the nitride

	C_{es}	C_{ms}	C_{me}	C_{bg}
Theoretical Value (pF)	19.29	26.67	0.0646 (up) 0.308 (down)	–
Measured Value(pF)	19.4	26.5	1.55	1.19

Table 3.4: Theoretical and measured capacitances for a packaged CCR.

thickness ($0.5\mu m$) and $\epsilon = 7.5\epsilon_0$. The corresponding A's were calculated from the layout which includes the actuator areas as well as the additional wiring and the pad areas. For C_{em}, theoretical estimate was calculated using Eq. 3.58.

The theoretical and measured values for C_{es} and C_{ms} showed excellent agreement. For all the devices tested, C_{es}, C_{ms}, and C_{bg} are within 10%; however, the ratio of C_{es} and C_{ms}, which should be equal to the ratio of the areas A_{es} and A_{ms}, are consistently within 2%. Unfortunately, the measured values for C_{me} did not appeared to be affected by the position of the actuator. In general, the measured values for C_{me} were several times larger than the theoretical values. Nevertheless, the measured C_me seemed reliable. The discrepancy is probably due to the parasitic capacitances associated with the packaging and the test circuit which are much larger than the actual capacitance.

To minimize the capacitance of the actuator during the operation, the moving mirror node was grounded and electrically connected to the substrate. The driving signal was applied to the driving electrode. Therefore, the capacitance of the device is equal to C_{test_3}, which is about $21pF$. This value can be reduced by optimizing the A_{es} such as carefully routing the wires which connects the drive electrode to the bonding pad.

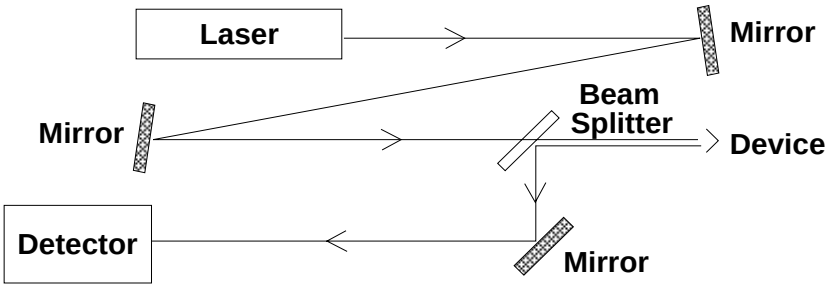

Figure 3.36: A typical optical setup used for testing fabricated CCRs.

3.4 Optical Experiment Results

Numerous fabricated CCRs were tested on an optical bench in controlled lighting. Shown in Fig. 3.36 is a typical test setup. Different optical components were mounted on a breadboard which was placed on a vibration isolation table. A dark environment was created by enclosing the breadboard in a box with black interior. A $10mW$ helium-neon laser with a wavelength of $633nm$ was used as the light source. The beam was aligned so that it was near parallel to the optical bench, and the beam intensity was varied in different experiments using beam splitters and neural density filters (not shown in Fig. 3.36). The device being tested rested on a combination of mounts which provided six-degree of alignment adjustments. In most cases, the reflected light from the device was directed to a silicon pin photo detector using a beam splitter and a mirror. A CCD camera and a power meter were also used in different experiments. Relevant details of each experiments will be discussed in the corresponding sections.

The performance of the fabricated CCRs obviously varied between design iterations. Rather than presenting results from every variations of CCRs, we will present only results which provide insights to the critical design and behaviors of the CCRs.

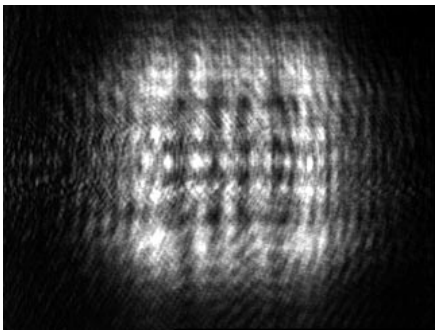

Figure 3.37: A CCD image of a typical mirror reflection. The gold-coated polysilicon mirror has dimensions of about 300 microns.

3.4.1 Reflected beam profile and divergence for a single mirror

When a single micro mirror is illuminated by a large laser beam, a complex reflection is created from the micro mirror. A CCD image of the reflection from a single mirror with dimension of $300\mu m$ is shown in Fig. 3.37. The square image corresponds to the square shape of the mirror, although much more complex compared to the diffraction pattern from a simple square aperture. The complex interference patterns are probably caused by the ridges, edges, and curvature of the mirror.

The divergence of the reflected light beam from the mirror was found to be greatly dependent on the mirror curvature. For example, the measured divergence from fabricated gold-coated polysilicon mirrors with the design in Fig. 3.2 (a) is about $36mrad$. These mirrors had measured radius of curvature, ρ, of about $10mm$ (Section 3.1.2). On the other hand, for the oxide encapsuled mirrors with the design in Fig. 3.2 (b) which had a radius of curvature of about $20mm$, the measured divergence was about $27mrad$. The theoretical estimate based on the diffraction (Eq. 2.16) is only $2.57mrad$, which is much smaller than the measured

values. Using a more simple estimate based on geometry, where

$$\frac{2\theta_{div}}{2\pi} = \frac{W}{2\pi\rho}, \tag{3.73}$$

(W being the mirror dimension), the corresponding estimates for the two different mirrors are $15mrad$ (for $\rho = 10mm$) and $7.5mrad$ (for $\rho = 20mm$), which are much closer to the measured values. Therefore, we conclude that the large mirror divergence is largely due to the mirror curvature. The non-uniform mirror profiles, especially near the mirror edges (Fig. 3.1.2) probably also contributed to the large divergences.

3.4.2 Reflected beam profile and divergence of a micro CCR

Now, consider the reflected image of a CCR. When an interrogating light shines at a CCR from the $-(1,1,1)$ directions, we predicted with our theory from Section 2.2.1 that the reflected light from an inactive CCR (one with a tilted base mirror) would have two light patterns and that the two light patterns would come together to form a single pattern when the CCR becomes active (all its mirrors become orthogonal). Using a CCD camera, we imaged the reflected light from a well-aligned CCR in the inactive and active states. The CCD images are shown in Fig. 3.38.

When the base mirror was tilted, the reflected light from the CCR showed two separate images (Fig. 3.38 (a) and (b)). When the base mirror was pulled down, the two images became overlapped and formed a single bright image (Fig. 3.38 (c)). A faint hexagonal shape is visible in all three images, although it is most clear in the combined image. This shape becomes more evident when the intensity of the image in Fig. 3.38 (c) is reversed and enhanced, shown in Fig. 3.38(d).

A hexagon shape was expected because the projection of a CCR on a plane is indeed a hexagon. Compared to diffraction simulations of a micro CCR with

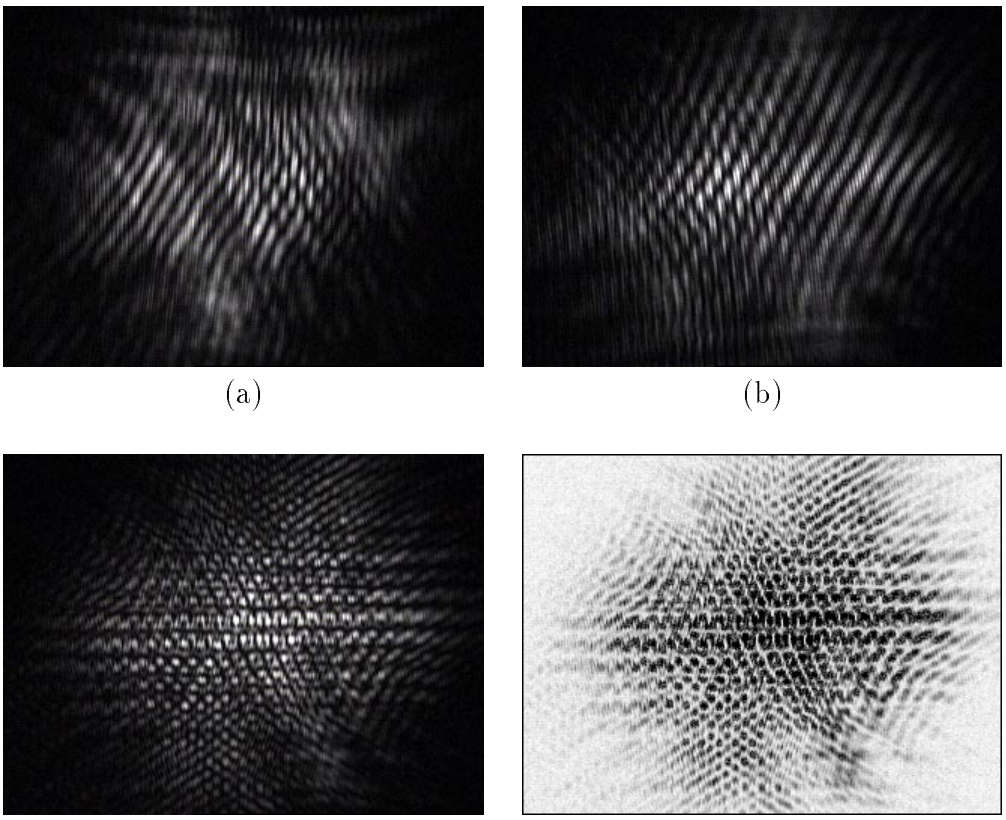

Figure 3.38: The two spots, bottom and top, reflected by a CCR in the inactive mode are shown in (a) and (b) respectively. The two spots combines into a single spot when the CCR becomes active as shown in (c). The reverse image of (c) is enhanced to show the hexagon shape of the CCR's reflection.

flat mirrors [38], the observed images lacked the sharp peak in the center of the beam due to the curvature of the fabricated mirrors. For CCRs with less perfect alignment, the combined light pattern may become enlarged and diffused, and the hexagon shape becomes less identifiable.

Depending on the misalignment, each of the two separate patterns in Fig. 3.38(a) and (b) may also split into 2 or 3 polygon-shaped patterns. If the alignment is significantly poor, the two set of light patterns in the inactive state may not even

meet. Poor alignment is often due to broken tie-downs, hinges, or locking plates. Such CCRs are not operational unless the detector has a large aperture and is placed in close range of the CCR (Section 2.2.1).

The reflected light beam from a CCR is affected by the alignment as well as curvature of the CCR mirrors. For example, we observed in the earlier CCRs that CCRs with the concave-down flipped mirror actuator (Fig. 3.14) generally have smaller divergence (by 10mrad or more) than CCRs with the concave-up mirror actuator with a gold front surface (Fig. 3.17). Despite of this benefit, the concave-down base-mirror design had the disadvantages of low reflectivity and difficult assembly steps (Section 3.1.4), we adopted the later design and further improved the mirror curvature and alignment support.

From optical experiments, it was found that measured divergence for laser light reflected by typical CCRs with gold front-surface mirrors like the one in Fig. 3.9 was about $25mrad$. These CCRs had oxide-encapsulated mirrors and alignment mechanisms with low tolerances. The best observed CCR reflection has divergence of about $15mrad$ while "bad" CCR reflections may be $40mrad$. Compared to the rough divergence estimate based on λ/d (Eq. 2.16), this measurement is about a factor of 5 to 10 greater. Therefore, these current devices are not near the diffraction limit of an ideal micro retro-reflector. Further reduction of the mirror curvature would be desirable for our communication application since the signal-to-noise ratio is inversely proportional to the fourth power of the CCR's divergence (Section 2.3.3).

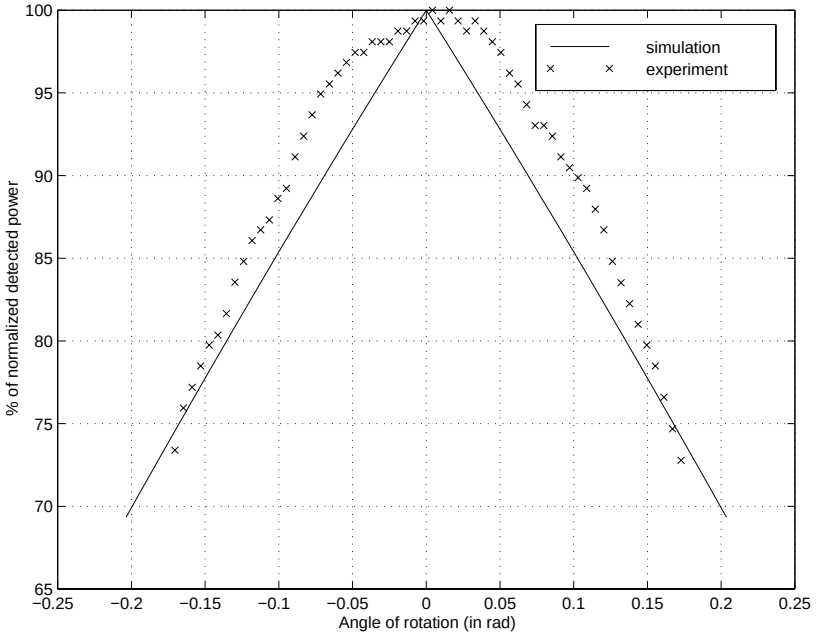

Figure 3.39: Measured and simulated optical response for different CCR orientations are compared in this plot. The simulated and measured response were normalized by the corresponding maximum response (at the 111 direction).

3.4.3 CCR response for different orientations

In Section 2.1.2, we discussed how the effective area of the CCR, which directly corresponds to the reflected power, is dependent on the direction of the incident light, or, equivalently, the orientation of the CCR. To determine the relationship between the response and the CCR orientation, we carried out the following experiment. We shined a laser beam at the CCR where the CCR appeared to have the highest reflectivity. With the laser direction fixed, we rotated the CCR about an axis normal to the optical table. We then measured the intensity of the reflected light from the CCR with a photo detector as a function of rotation and compared the result to simulation.

Although the experiment was conceptually simple, collecting meaningful data

was difficult because precise optical alignment was critical. The laser beam must be adequately columated and wide so that the reflected light from the CCR would only depend on the orientation and not the profile of the laser beam. The laser beam must be aligned to intersect the axis of rotating stage. The CCR must also be properly aligned to the axis of rotating stage. Improper alignment to the rotation axis would cause the CCR to translate away from the center of the laser beam. Finally, it was also necessary that all the reflected light from the CCR (in the active state) was completely collected by the aperture of the detector.

The result of this experiment is shown in Fig. 3.39 and is compared with simulation results based on the analysis from Section 2.1.2 for an ideal CCR. The simulated as well as the measured values were normalized by the corresponding maximum value. The incident laser angle relative to the CCR was changed from -0.17rad (10 degrees) to 0.17rad from the ideal (111) incident direction. Intensity change for larger angles of deviation could not accurately measured because of the limited range of the rotating stages. The measured and simulated values showed good agreements in the range tested.

The intensity, which is proportional to the CCR effective area, was found to decrease nearly linearly as the laser direction deviates from (111). The slope of the intensity decrease is about 10% per 0.05rad (2.9 degrees), which is similar to the predicted value (10% per 0.066rad (3.8 degrees) in the linear region. The round peak of the measured data also differed from the sharp peak of the simulation which assumed that the CCR was in perfect alignment with the CCR and the axis of rotation. The differences between the measured and simulation data are due to the CCR mirror curvature, which is not taken into consideration by our simulation, as well as the non-ideal experiment setup. For example, we found from

simulation that any small initial misalignment in the mount would in fact create a round instead of sharp peak. Therefore, we know that our theoretical model can provide reasonable estimate of the effective area of the CCR.

3.4.4 Dynamic experiment results

We were interested in finding out the dynamic response of the CCRs. Therefore, illuminated CCRs were modulated with a positive square wave at different frequencies. The square wave was generated by a function generator which switches a MOSFET on and off. The reflected light was detected with a photo diode as shown in Fig. 3.36. The output of the photo detector is connected to an oscilloscope.

From Fig. 3.38, we know the reflected beam from a CCR is not uniform in intensity, even for a highly orthogonal CCR. As a result, depending on the position of the photo detection, we were able to observe slightly different waveforms. To achieve consistent results, the photo diode in Fig. 3.36 was aligned so that when the CCR was active (orthogonal), the center of the reflected beam would lie on the center of the photo diode. When the CCR was inactive, no reflection from the CCR would hit the photo diode, and the two reflected beams would be away from the photo diode by the same distance.

The simple setup shown in Fig. 3.36 with a single photo diode actually could not provide precise information about the motion of the actuator due to the nonlinearity of the photo detector and the actuator's large range of motion. Nevertheless, this setup was used because it precisely resembles a typical application of micro CCRs, where the large reflected beam from the CCR will scan back and forth across a small detector aperture.

Figure 3.40: Raw output of photo detector for different CCR modulation frequencies. Direction of incident light is near (-1,-1,-1). The square wave represents the input signal which modulates the CCR, where a low input pulls down the movable mirror. Actuation voltage is 15V.

Fig. 3.40 shows the raw signals (with no amplification) from the detector at the oscilloscope when the CCR in Fig. 3.14 is driven at different modulation frequencies. The square waves represent the input signal to the circuit which powered the CCR, where a low input activates the CCR. The high level of the detector waveforms correspond to increased intensity detected by the photo diode. Fig. 3.40 show that the detector waveforms change in shape and magnitude as the frequency changes.

At low frequencies, the change in detector output could be as high as 260mV (corresponding to about 0.5μW), with a relatively small DC offset of 50mV. Peaks are often observed before the rising and falling edges of the detector output. The source of these peaks is still unclear, although both Fig. 3.23 and Fig. 3.40 suggest

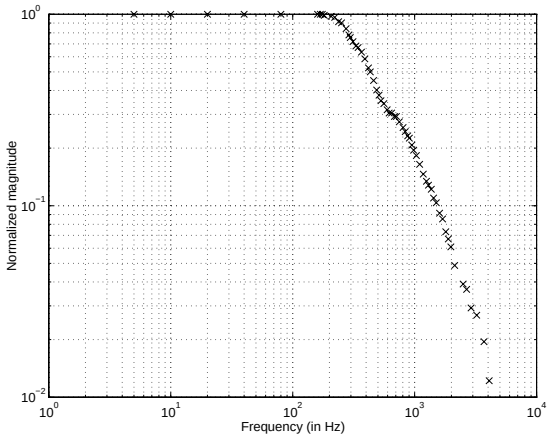

Figure 3.41: Magnitude plot of the intensity change of the photo detector waveform as a function of CCR modulation frequency.

that reflective transitions may occur more than once during each cycle. The rise time and delay of the rising edge have been observed to decrease with increased applied voltage (beyond the pull-in voltage). At high frequencies, the AC component of the detector waveform begins to decrease in amplitude while the voltage peak remains constant, indicating that the actuated mirror lacks time to move away from the pull-down position. Fig. 3.41 shows the AC magnitude change versus the frequency. The -3dB point occurred at 444Hz. It has also been observed that the detector waveform may change in intensity and shape depending on the direction of the incident light, yielding a different frequency magnitude plot (Fig. 3.42).

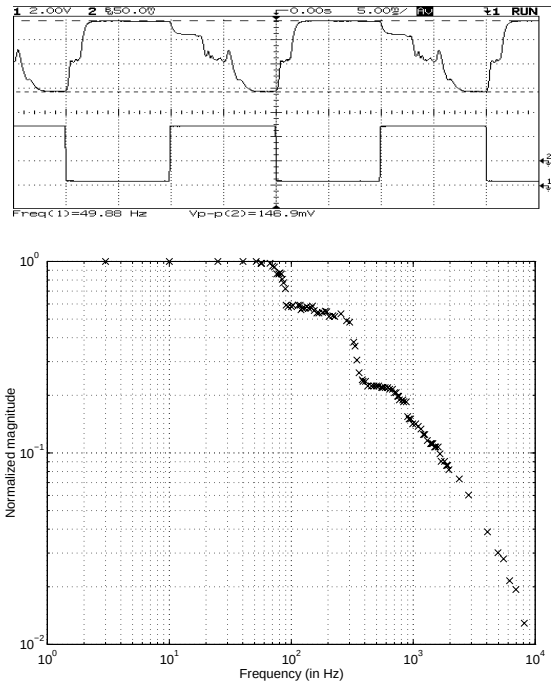

Figure 3.42: Waveform and magnitude plots of the intensity change of the photo detector waveform as a function of CCR modulation frequency. The incident angle as well as the observed spot location are changed from Fig. 3.40. Actuation voltage is 18V.

4 Communicating with Micro Corner Cube Reflectors

Consider a micro corner cube reflector located at a distance which is modulating its shape from perfectly orthogonal to non-orthogonal according to a digital data stream generated from a sensor or some other data source. As described in Section 1.2, we can shine light at the CCR and detect its modulated reflection and thus retrieve data from the CCR. Effectiveness and complexity of this communication method will depend on the choices of light source to use, optical detection method, coding and signal processing schemes. This chapter will focus on these broader system issues, particularly related to designing a receiver for the CCR transmitter.

There are a number of challenges in order to receive data from the modulating corner cube. In Section 4.1 and Section 4.2, we will discuss issues related to establishing a communication link with remote CCR units and interrogating light selection and detection. In Section 4.3 and Section 4.4, we will present two receiver system designs which used two different methods to receive data from CCRs. These systems assume that we know the rough location of the CCR well enough so that we can shine a laser directly at the CCR (the laser beam will be much bigger than the size of the CCR). Although the two methods used in these systems are significantly different, the two methods can potentially be combined or modified depending on the need of the applications.

4.1 Establishing a communication link

To communicate with a CCR, we are required to shine light at the CCR from the proper quadrant of a hemisphere since the CCR is responsive to light only from a

particular quadrant. Fortunately, we do not need to know its precise orientation since precise alignment is not necessary for communication as discussed in Chapter 2. A transmitter ideally would have multiple CCRs with various different orientations so that it may respond to interrogators from any direction. In applications where the general location of the transmitter is known, such as friend-or-foe identification of a tank, we may simply direct an interrogating laser at the tank and analyze the reflected light. In other applications such as distributed sensing, establishing communication may not be as simple since multiple transmitter units may be scattered in a large area. If the transmitters' surrounding is highly reflective, locating and identifying a transmitter will be especially difficult.

In general, the transmitter (and definitely the CCRs) will be invisible to the interrogator. As a result, the interrogator may not easily be able to determine the exact location of the device and must use a broad laser beam to find the transmitter. The interrogator can locate a transmitter with CCRs by scanning an area with the laser beam and searching for highly reflective structures. The reflective structures can further be investigated by verifying whether the reflected light from each structure contains any meaningful information. For example, a random stationary reflective object should be constantly reflective and its reflection will contain no information. On the other hand, a CCR unit can be programmed to give out a periodic data stream so that its reflection can be identified. Once the initial communication link is established, we may then narrow the interrogating laser beam to increase the signal-to-noise ratio during a long data transmission.

In the case where multiple CCR transmitter units are illuminated by a laser simultaneously, cross-talk or interference may occur. If the CCRs have a large bandwidth, spread spectrum techniques such as code-division multiple access (CDMA)

could be used for multiplexing. For CDMA, a significant portion of the bandwidth would be sacrificed.[18] Time-division multiple access(TDMA) and frequency-division multiple access (FDMA) are also non-ideal to implement since the interrogator is required to coordinate all the different units. On the other hand, space-division multiple access (SDMA) may be most simple to implement, and the CCRs would not be required to have high bandwidth. In Section 4.4, we will present a receiver system which uses an imager to communicate with multiple CCRs.

4.2 Competing with ambient light

In a bright environment, the modulation of a micro CCR is visible to our naked eyes if it is placed within a few inches away. The reason is that the CCR reflection is not only stronger but also more directional than the reflection from its surrounding. As a result, we are able to distinguish its reflection from the other light detected by our eyes. In this case, no special interrogating light is needed. In the case where a bright and focused interrogating light is used, one might think that it is always possible to detect the CCR modulation as long as the interrogating light is comparable to the ambient light in intensity.

A bright focused interrogating light is desirable for two reasons. Stronger interrogating light which hits the CCR will result in more reflected light which contains data. Furthermore, less area of the CCR background will be illuminated, thus reducing reflected light which contains no data. However, out shining the ambient light with our interrogating light does not automatically solve all the problems.

From the SNR analysis in Section 2.3.3, we know that ambient light, including the reflection of the interrogating light from the CCR background, has a significant effect on the SNR because of the shot noise it induces in the detector. In

addition, strong ambient light could also create a large current offset and either saturate the detector or decrease the dynamic range of the detector. Therefore, the interrogating light being reasonably bright and focused is not sufficient. It should also have distinct characteristics compared to the ambient light so that the undesired ambient light could be filtered, not ever reaching our detector. For these reasons, in the SNR analysis in Section 2.3.3, we chose to use a laser as our interrogating light so that we could put a narrow bandpass filter in front of the detector to remove the undesirable ambient light.

Naturally, we would like to select a wavelength which does not have a large component in the ambient light spectrum and which will not be absorbed or distorted by the transmission medium. In all our communication demonstrations, we used laser modules with wavelength of $670nm$, largely because of its wide availability. Gold, which is the available coating for our CCR mirrors, is also known to have high reflectivity at this wavelength. Lasers with wavelength of $840nm$ were recommended for long-distance optical transmission because both Rayleigh scattering of solar radiation effect and thermal radiation effect due to the atmosphere may be neglected.[44]

A continuous-wave (CW) laser can be used for interrogation as we will show in Section 4.4. However, a modulated interrogating laser can provide an additional benefit: it can be used to distinguish the CCR reflection (which contains data) from the general ambient light which also happens to pass through the optical filter. In other words, with a modulated laser, the CCR signal spectrum is shifted to the spectrum centered at the modulation frequency away from the noise at the low frequency spectrum. Therefore, by sending the detector output to a bandpass filter (an electronic one instead of an optical one), we can extract the CCR signals

as we will show in Section 4.3.

Note that the extracted signal will contain not only the CCR signal but also the signal from the CCR background illuminated by the interrogating laser. This background reflection can be reduced by narrowing the interrogating beam. Unfortunately, in most applications, the interrogating beam must have adequate width to prevent optical alignment problems. The background reflection can also be reduced or even removed using a spatial filter via a detector array. We will further describe this approach in Section 4.4. A conceptually more simple solution is to add an additional level of modulating or encoding with the CCR. In that case, an additional filter or decoder must follow the first bandpass filter. A portion of the CCR bandwidth will also be sacrificed with this approach.

Depending on the application requirements, different signal modulation and receiver design may be needed. The following sections in this chapter describes how the CCR was demonstrated as a free space optical transmitter using two different receiver systems. The focus in this work is not necessarily to create the best receiver for micro CCR communication but merely to show the feasibility of micro CCR based communication links.

4.3 Transceiver system with a modulated laser and a single photo-detector element

A simple CCR communication link can be built using a single photo detector for optical detection and a modulated laser for interrogation. [12] The schematic diagram for this communication link is shown in Fig. 4.1. The receiver shines a laser beam at a single modulated CCR. The CCR reflected light is collected

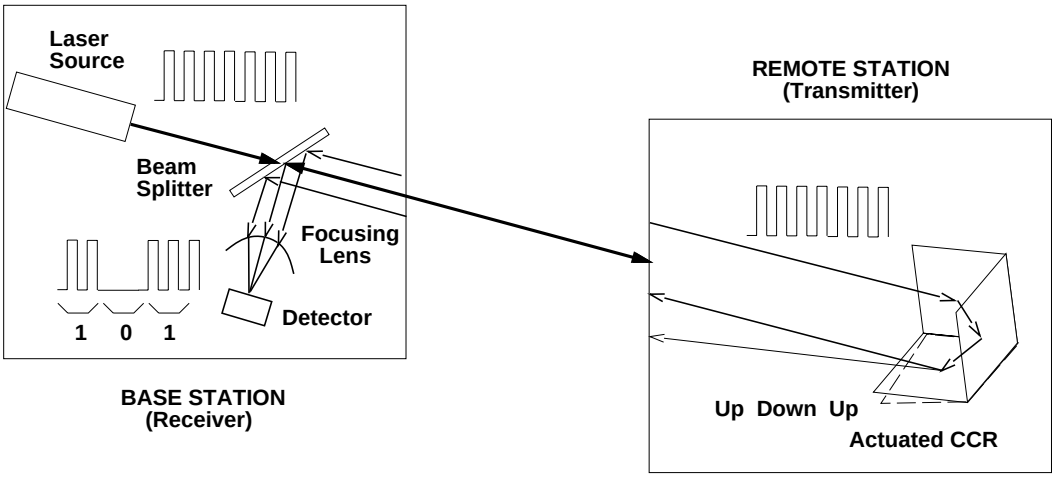

Figure 4.1: Schematic diagram of a CCR communication link using a modulated laser and a single photo detector for interrogation.

with a lens and focused onto a photo detector. The photo detector output is then processed to retrieve the CCR signal.

The advantage of the system shown in Fig. 4.1 is that the CCR data spectrum is shifted to the spectrum centered at the laser modulation frequency away from ambient noise at low frequencies. Many commercial lasers can be modulated to mega Hertz range so that there is still sufficient bandwidth for the CCR data. Furthermore, it is relatively easy to find a high performance single photo detector and to design suitable electronics to amplify and decode a single detector's output.

4.3.1 Prototype hand-held transceiver

To demonstrate this communication scheme and the functionality of the CCR, a palm-size transmitter unit and a similar sized receiver unit have been built (Fig. 4.2). This transmitter can send either a periodic or an arbitrary digital signal to the receiver. The prototype transceiver system with the micro CCR operates in the arrangement shown in Fig.4.2, where the receiver's laser beam is

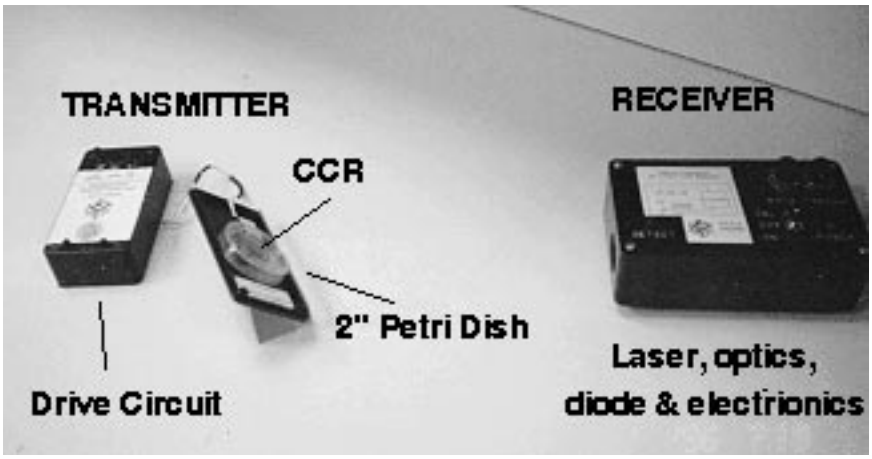

Figure 4.2: Photo of prototype transmitter (on the left) and receiver (on the right). The receiver box is $15 \times 10 \times 6cm^3$ in size, which built-in laser module, photo-detector, and signal processing circuits.

aimed at the CCR of the transmitter. A light emitting diode (LED) on the transmitter unit blinks according to the signal being transmitted, while another LED on the receiver unit blinks in synchrony when the receiver successfully detects the reflected signal.

4.3.2 Hardware implementation

The block diagram of the receiver is shown in Fig. 4.3. The receiver module contains a laser diode module from a commercially available laser pointer with wavelength of about $670nm$. Initially we used laser diode modules taken from commercial laser pointers (CL2000 laser pointer by HSN Marketing Inc., Booton, NJ). Modulated at 2kHz, a typical laser module was found to output a laser beam of $1.7mW$ rms power, although the laser output was found to decay quickly after limited hours of testing and the quality of the laser beams were also found to vary greatly for different laser modules. A miniature $4.2mW$ laser diode module

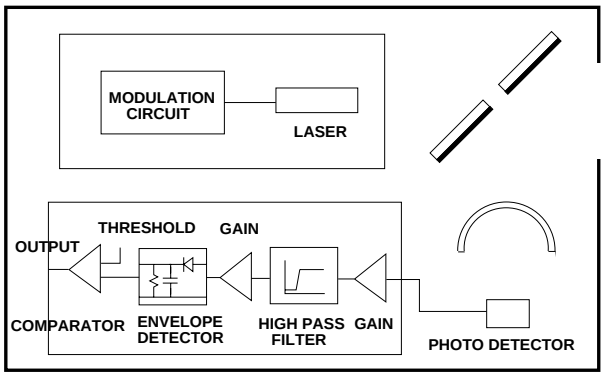

Figure 4.3: Block diagram of the hand-held receiver module.

(A53163 from Edmund Scientific) which can be modulated up to $100kHz$ has also been used. At $70kHz$, the laser has an rms output of about $2.6mW$.

A $2.5cm$ diameter lens was used to focus the returned light onto a silicon P-I-N photo diode (FDS100 by ThorLabs). The photo diode had an active area of $13.7mm^2$ active area with $20nA$ dark current and $1.2\times10^{-14}W/\sqrt{Hz}$ NEP. The purpose of the lens was to increase the photo detector aperture. However, if the returned beam from the CCR had a divergence of 20mrad and the CCR is 2 meters away, the lens will only capture at most a quarter of the returned light. A large lens or aperture was not used because we wanted to build a small size receiver.

Due to space considerations, the lens and the photo detector are placed 90 degrees from the path of the outgoing laser. A beam splitter is placed in front of the laser module to direct the returned light to the photo detector. The use of a 50% beam splitter in this fashion was not ideal because the outgoing laser and the returning laser are reduced in power by half, yielding a 75% reduction in detected laser power. As a result, custom-made beam splitters were also used. One beam splitter was made from a glass slide with metal evaporated on one side and a hole is patterned on the metal to allow the outgoing laser beam to shine through.

Another beam splitter was made from a silicon wafer with gold evaporated on one side and a small hole etched through the wafer with KOH. In both cases, the loss of power is reduced from 75% to about 30 to 40%.

As shown in the system block diagram in Fig. 4.3, the photo detector output is first amplified by a factor of 10 and then high-pass filtered with a four-pole 2 stage Butterworth filter [35]. This filter removes the low frequency noise from ambient light as we had discussed in Section 4.2, although ideally a bandpass filter should have been used instead. A high-pass filter was used in this case largely because of its simplicity so that it could be easily modified (or even left unchanged) when the laser modulation frequency or the data bandwidth was changed.

The filtered signal was further amplified with an adjustable gain amplifier. Although this gain stage was designed to amplify the signal by up to 70 times, the actual achievable gain was only about 5 before the gain stage became unstable. The signal was then passed through an envelope detector to remove the high frequency laser modulation. The signal then went through a threshold comparator to remove additional noise including noise or offset due to CCR background reflection, high frequency noise from ambient light, and inherent sensor noise, yielding the actual transmitted digital data.

The receiver unit is powered by three 9-volt batteries, one for the laser module and driving circuit, and two for the detection circuit. It was found necessary to separate the laser modulation circuit from the detection circuit to minimize cross-talk.

The block diagram of the CCR transmitter module is shown in Fig. 4.4. The chip with the micro CCR is glued and wire-bonded to a plastic substrate with

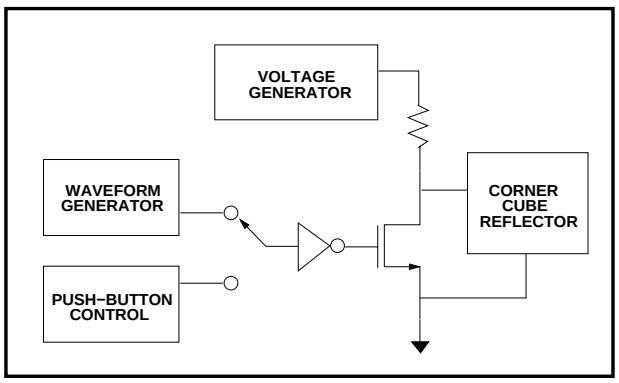

Figure 4.4: Block diagram of the hand-held CCR transmitter module.

copper bonding pads. The plastic substrate with the chip is stored inside a transparent petri dish to prevent damage to the CCR. (Fig. 3.33(a)) The transmitter module can drive the micro CCR with either a low-frequency square waveform (2Hz) or a constant high or low voltage controlled by a push-button. An additional transmitter module was also made to allow the micro CCR to transmit a periodic digital waveform which was set using dip switches. A voltage multiplying circuit using Maxim773 is used to supply a voltage between 10 to $20V$ needed for the CCR actuator. The transmitter module is powered by a 9-volt battery. Note that no effort was made to miniaturize or reduce the power consumption of the transmitter module because these transceiver modules were used to demonstrate only the feasibility of the proposed communication strategy.

4.3.3 Results

Figure 4.5 shows typical waveforms in the receiver circuits when the receiver was successful in interrogating the CCR transmitter. The bottom waveform represents the detector output signal after passing through the high-pass filter. An on-off keyed signal is clearly visible, although the signal-to-noise ratio is only about 5.

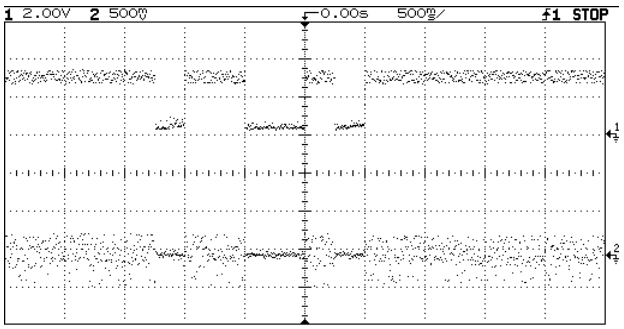

Figure 4.5: Waveforms in the different stages of the in hand-held receiver demo unit. The bottom waveform is the output of the filter stage. The top waveform is the output of the envelope detector stage.

The top waveform represents the signal after passing through the envelope detector which, in fact, strongly resembled the signal used to modulate the CCR.

Free space communication across a distance of more than 4 meters under normal room light was demonstrated. When the CCR is covered with a petri dish lid, the largest distance demonstrated was only about 1 meter. Highest observed communication rate transmitted and detected with the prototype is 1K bps. Therefore, with this system, we successfully demonstrated the concept of communication with a micro CCR.

Nevertheless, the proto-type system was found to have numerous problems, including the internal scattering of the interrogating beam before exiting the interrogator, loss of optical power through the beam splitter, and cross-talk between the laser modulating circuit and the detector circuit despite of using separate power supplies. Precise alignment between the interrogating unit and the transmitter unit was found to be extremely important. Furthermore, with this prototype system configuration, communication with multiple CCR units could not be easily implemented.

There are a number of possible system design changes which would certainly improve the system, such as using a band-pass filter instead of a high-pass filter, increasing the receiver aperture size, adding an optical bandpass filter before the detector, and finally using a robust gain stage. Instead of further improving this proof-of-concept system, we explored a different interrogating system design for long range communication with multiple CCR units. This system is presented in the following section.

4.4 Transceiver system with constant power laser and an imager

In the previous section, we discussed using a single photo-diode to detect reflected light from an interrogated CCR. The fundamental disadvantage of this scheme is that the output of the detector will be an integration of all the light of every light-emitting or reflecting object in the field of view of the optics. Bright or reflective objects in the background of the CCR may then "drown out" the reflection from the CCR. Unless a more sophisticated coding method is used, such as frequency modulating the CCR, we will not achieve an adequate signal-to-background ratio. In this section, we will describe results using a photo-detector array to design a receiver for communication with a corner cube reflector.

Consider that we interrogate a CCR with a CW laser source. In this case, we will focus the view of the interrogated CCR to a photo-detector array instead of a single photo-detector. As shown in Fig. 2.13, each element of the photo-detector array will have light intensity (and color) corresponding to only a specific region of the view. A bright object in the field of view may affect only some elements in

the array significantly but have minimal or no affect on other elements. Moreover, the element or elements corresponding to the region of the view which contains the CCR will be mostly influenced by the CCR reflection and not by other objects nearby. Therefore, the photo-detector array in essence provides a spatial filter which filters out (or spreads out) the background image "noise" so that the CCR reflections can be more easily identified. In fact, as shown in the SNR analysis based on detector shot noise in Section 2.3.4, the SNR could theoretically be increased by N_{det} times given N_{det} detectors in the array. Detectors with N_{det} greater than 100,000 are widely available.

This detection scheme also allows simultaneous communication with multiple CCRs. Suppose multiple CCR units which are spatially separated are illuminated by the interrogating laser. The CCR units, if sufficiently far apart, will appear in different regions of the photo-detector array. Depending on the closeness of the CCRs and the number of the detectors in the array, one or more detectors could be dedicated to communicate to each CCR unit at a given unit of time. Obviously problems would occur if more than one CCR reflections are focused on a single detector element. In that case, each CCR must encode its data, similar to the single detector case.

Using a multiple detector array in the interrogator receiver, we will need to perform image processing to determine which elements of the array correspond to some modulated CCRs and to keep track of these elements to retrieve the actual data transmitted by each CCR. One simple method of identifying a modulated CCR in a set of consecutive images is by performing a image subtraction between one image frame and the previous frame. The image difference will contain pixels

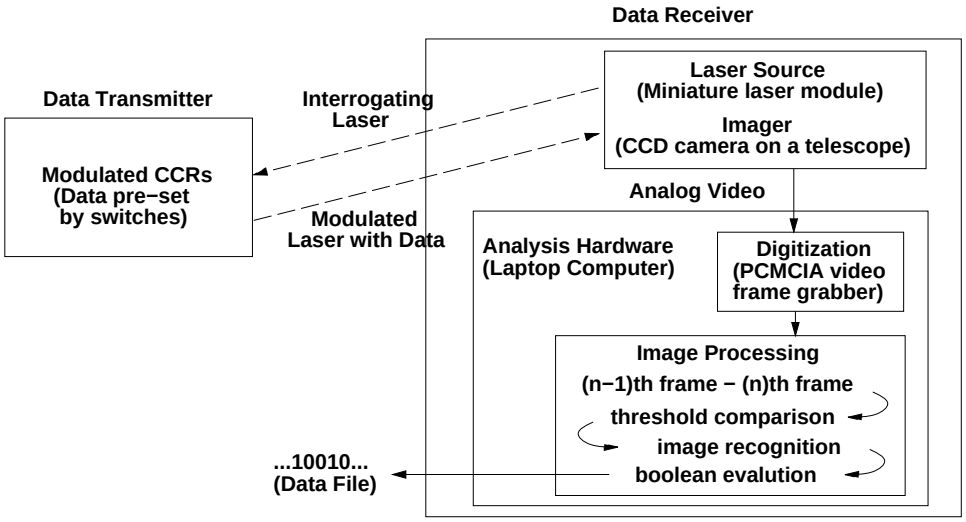

Figure 4.6: Block diagram of a CCR communication link whose receiver uses a multiple-element detector.

which have changed intensity during that time increment. If only pixels corresponding to modulated CCRs change intensity, then the CCRs can immediately be identified from the image difference. A block diagram of a CCR communication system which uses a photo-detector array for detection is shown in Fig. 4.6.

One of the disadvantages of this scheme is that the data transmission rate may be significantly reduced due to photo-detector arrays and system hardware processing speed limitations. While typical video systems run at 30 frames per second, high speed imaging systems with CCD cameras or active pixel CMOS cameras may run at 1000 to even 10000 frames per second (for a short data collection period). Nevertheless, this receiver design could be useful in situation where data bandwidth may be compromised to yield improved signal-to-noise ratio.

4.4.1 Prototype system hardware

A prototype system was built according to the block diagram in Fig. 4.6 to demonstrate the detection and communication concept. The system uses all commercially available components with the exception of two adaptors. The choice of these components was to demonstrate that simple and relatively low-cost off-the-shelf equipments can be used to build a reasonably robust yet portable receiver system for CCR communication.

The prototype system has a miniature $4.2mW$ CW laser module as the interrogating light source, a small telescope as the light collector, a black and white CCD camera as the photo-detector array, a PCMCIA video frame grabber to digitize the analog video output from the camera, and finally a laptop computer as an image processor. Table. 4.1 shows the details of each component.

The telescope is a 4-inch Newtonian reflecting telescope which has a magnification of about 30 with a $15mm$ eyepiece. Although this telescope was cheaper than most competitive telescopes, it was found to be a poor choice of telescope for several reasons. In order to attach a CCD camera to the telescope for eye-piece projection, it was necessary to create a custom-made adaptor to connect the camera (which has a C-mount) to the telescope eye-piece. Moreover, once the CCD camera was mounted on the eye-piece, it became very difficult to adjust the telescope focus because of the instability of the focus knob.

The miniature laser module is set in a custom-machined mount made of acrylic which is attached to the center of the aperture window of the telescope, where the telescope second mirror is connected on the opposite side. The laser module and mount were not found to cause any obstruction to the view of the telescope for far-field objects. The axes of the laser module and of the telescope are set to close

Component	Manufacturer	Part #	Description
Laser source	ThorLabs	98002-083	$670nm$, $4.2mW$, $5.0\times1.2mm^2$ beam, $1.5 \times 0.3mrad$
Telescope	Edmund Scient.	M2015, Astroscan	$4.25in$ diameter, Newtonian, 3.5deg field, $445mm$ focal length
CCD Camera	Cohu, Inc.	2122-2023	Monochrome, $1/2in$, RS-170A: 768(H)$\times$494(V), $8.4\mu m \times 9.8\mu m$
Frame Grabber	MRT	MS801	PCMCIA, 8-bits/pixel for monochrome, max 8Mbyte/sec transfer-rate
Laptop Computer	Dell Comp.	Latitude LM	166 Pentium, 40M RAM

Table 4.1: Brief descriptions of the prototype receiver components

alignment so that the reflection of the laser beam appears near the center of the eyepiece. One can aim the laser at a distant CCR by steering the telescope which is mounted on a tripod for stability during operation.

The CCD camera was selected for its light weight, small size, high resolution, and availability. Unfortunately, this camera had a frame rate of only 30 frames per sec, which is the standard for NTSC video. This frame rate limited the maximum bit rate of the CCR to only 15. Much higher frame rate cameras are commercially available; however, other components of the receiver system including the frame grabber and the computer would be required to have much higher performance. Since this prototype's goal is for demonstrating the communication strategy, we chose not emphasize high data transfer rate.

The laptop computer was used for the system primarily to allow more portability; however, a desktop computer for the same cost would most likely give a faster performance. The particular model of the laptop was selected for its price,

high processor and system speeds, fast graphics display, and a fast PCMCIA bus architecture to service a PCMCIA video frame grabber. This laptop allows data to transfer from the PCMCIA bus directly onto the PCI-32 bit bus, which is (at least twice) faster than many laptops which have to transfer data from the PCMCIA bus to the ISA bus, then finally to the PCI bus. During the course of computer purchase and experiment with the system, faster laptops became available in the market. However, we did not repeat our experiments with the newer computers since it was obvious that high data rate would be achievable. The selection of the video frame grabber was simple since it was the only PCMCIA frame grabber which we could find commercially.

4.4.2 Prototype system software

A software program was developed to locate and keep track of blinking CCRs observed by the telescope. The window-based program was created using Microsoft's Visual C++ Compiler 4.0 and the software developer kit associated with the frame grabber. This program, enhanced from a free demonstration program, used predefined subroutines by the frame grabber manufacture as well as newly developed subroutines.

The program allowed the user to see the view of the telescope on the computer screen so that the user could aim the laser at the CCRs. As shown in Fig. 4.7, the view of 2 CCRs through the telescope is displayed by the CCR demonstration software. These CCRs are kept in transparent boxes with opened lids.

The program also allows the user to see the images generated from the thresholded subtraction between consecutive video frames using another view window as shown in Fig. 4.8. If two consecutive images have pixels with large difference

Figure 4.7: Video display screen of the CCR demonstration software showing two CCRs aligned with a laser beam through the view of a telescope.

in intensity, the corresponding pixels will appear on the white display area. The threshold for the difference is set by one of the scroll bars. Although the background surrounding is expected to remain constant in a controlled environment, slight pixel variations (a few percent of full scale) are often found, possibly due to vibration of the surrounding light sources, digitization errors, or air motion. Based on the noise present in these images, the user can increase the threshold (to a few percent) until all spots in the images disappear except for the blinking spots corresponding to the modulated CCRs.

The user can then define a sampling period during which the program will collect data. Data is collected by calculating the centroid and size of each spot appearing in each generated image and recording the blinking of each spot since its first appearance. Each spot is assumed to be the reflection of a modulated CCR. The user sets the duration of the sampling period with a sliding bar and begins the

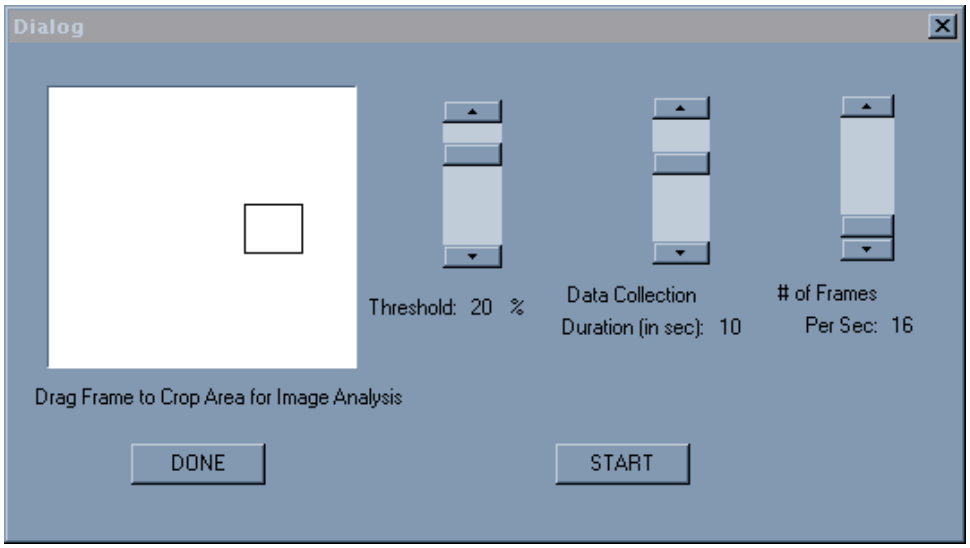

Figure 4.8: Another screen of the CCR demonstration software which is used to show the thresholded differences between consecutive images. Controls for the data collection option are also shown.

data collecting process by pressing the "START" button. At the end of the period, the result is written to a file on the hard drive. The file summarizes the number of CCRs found and the blinking sequence of each CCR during the sampling period.

Furthermore, since the user knows where the blinking CCRs are located in the image prior to data collection, the software also allow the user to specify a small region for analysis during data collection to minimize computation time. The small frame in the white area may be resized using the mouse for that purpose. The user may also set the sampling frequency of the video system. If the analysis region is small (100 by 100 pixels), then 16 frames per second would yield reliable results. 20 frames per second appears to be the maximum rate for our computer system even if the analysis region is further reduced to just a few pixels. Therefore, the data sampling rate for our system was limited by the frame transfer rate between the video frame grabber and the computer.

When collecting CCR data, the program analyses the incoming video frames, carrying out the following steps repeatedly:

1. Capture a new frame and store it as the "new" bitmap.

2. Create a "thresholded" bitmap where each pixel corresponds to the thresholded difference in intensity of the corresponding pixels between the "new" bitmap and the "previous" bitmap. When the intensity difference is greater than the threshold, the pixel of the "difference" bitmap is made black; the difference is less than the threshold, the pixel is made white. (The "threshold" bitmap can be displayed on the computer screen for viewing.)

3. Identify each isolate spot which appears on the "threshold" bitmap. Each spot detected is assumed to be a CCR. Calculate the centroid and size of each spot.

4. Update the list of detected CCRs: new CCRs are added to the list; the reappearance of previously detected CCRs are marked as transmitting a "1"; and the disappearance of previously detected CCRs are marked as transmitting a "0". A CCR is considered new if its centroid does not lie within the circumference of any previously detected CCRs.

5. Store the "new" bitmap as the "previous" bitmap.

4.4.3 Experiment setup

Experiments with the prototype system were carried out indoors. All the indoor experiments were performed under regular room light in the long hallways in the

Engineering IV building or in the basketball courts of the UCLA Men's Gymnasium and Pauley Pavillion. Outdoor experiments were not carried since we were not able to secure a large outdoor area devoid of people.

The $4.2mW$ $670nm$ laser we used was classified as a Class 3A laser. It is similar to laser modules which are commonly used in laser pointers for presentations in classrooms and lecture halls. According to the Laser Institute of America, even though it is possible for a Class 3A laser to exceed exposure levels for the eye in 0.25sec, it poses only a low risk of injury [86]. Following the guidelines provided by the American National Standard Institute [1], we found that the nominal ocular hazard distance (NOHD) for our laser was about 10 meters for a 10 sec exposure. NOHD is defined as the distance along the axis of a direct laser beam to the human eye beyond which the irradiance or radian exposure would not exceed the appropriate maximum permissible exposure (MPE). NOHD can be estimated using the following expression:

$$NOHD = \frac{1}{\phi}\left(\frac{4\Phi}{\pi\ MPE} - a^2\right)^{0.5} \tag{4.74}$$

where ϕ is the beam divergence in radian, Φ, the total laser power output, and a, the diameter of the emergent laser beam.

In other words, our laser was essentially eye-safe as along as no direct viewing of the laser would take place closer than 10 meters. By aiming the laser at waist height and by preventing people from standing close to the laser, we did not create any hazardous situation during our experiments.

The setup of the experiment is shown in Fig. 4.9. One or two CCRs were placed at various distances from the interrogator system. And the CCRs and the interrogating laser were roughly aligned to yield strong reflections from the CCRs. To achieve large distances (greater than 70 meters), a mirror was also used in some

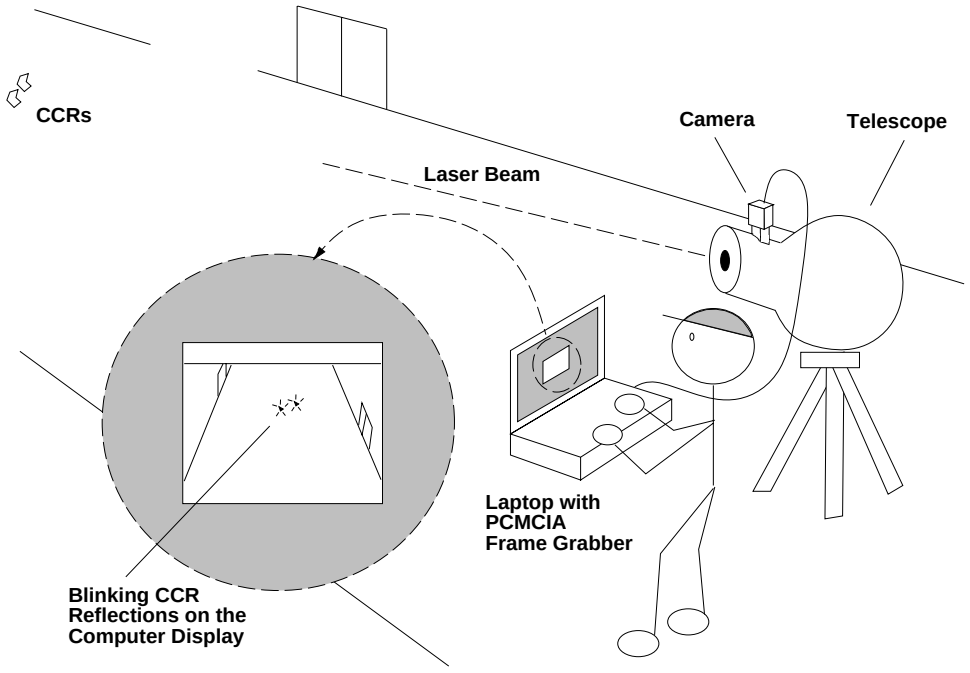

Figure 4.9: The experimental setup for the CCR communication link using a CCD camera.

experiments. In these cases, the interrogating laser on the telescope was directed to a square mirror with $3in$ sides. The mirror was aligned so that the interrogating laser would shine on the CCRs. The reflected light from the CCRs would then hit the mirror and return to the interrogator. The optical path (or the effective communication distance) was generally set to be about twice the distance between the interrogator and the mirror.

The CCRs, mounted only a few centimeters apart, were independently modulated by a battery-powered module, each of them transmitting 16 bits periodically. Each of the 16-bit sequence was composed of 8 bits (set by dip-switches) followed by 8 bits of *1*'s. Since the frame grabber software worked reliably at about 18 frames per second, the bit rate was set to be about 4 bits per second.

4.4.4 A measure of noise

In Section 2.3.4, the analysis of the signal-to-noise ratio for a receiver which uses a detector array was presented. This analysis focused on the effect of shot noise in the detectors but neglected other noise effects. In this section, we would like to define a broader measure of SNR which can be used to evaluate our experimental results.

Assume that we use the image subtraction method in Fig. 4.6 to find CCRs in our camera output. Any intensity changes in a pixel from one frame to another may be interpreted as a CCR being modulated. A valid modulated CCR could certainly change the intensity of a pixel or a cluster of pixels. Random motion of the objects in the CCR background, modulated light sources in the CCR background, relative motion between the interrogator and the background (such as from vibration), and light attenuation from atmospheric effects could also cause some pixels' intensity to change in time. Even though these effects might not necessarily directly introduce noise to the pixels corresponding to valid CCRs, "false-detection" of CCRs is certainly possible.

In addition, constant background light could create an offset in the intensity of the pixels. If the light is strong enough to saturate the CCR pixel regardless of the CCR's state of reflectivity, then no information can be collected from the CCR. If the CCR pixel is saturated only when the CCR is reflective, the CCR signal may still be retrieved from image subtraction. However, the measured CCR intensity change could be much smaller than the actual optical intensity modulated by the CCR. Probability of detection is, therefore, decreased due the intensity offset from the background light.

With these noise effects in mind, we define a measure of signal-to-noise ratio as

the ratio between the intensity change of the CCR pixel divided by the intensity change of a background pixel:

$$SNR = \frac{\Delta intensity\ of\ CCR\ pixels}{\Delta intensity\ of\ background\ pixels} \tag{4.75}$$

Since the change in intensities are calculated from the digitized values of the camera video output, the SNR would include not only all the noise effect we already mentioned in this section but also noise effect due to detector shot noise and video frame grabber quantization noise.

4.4.5 Spatial filter results for a single CCR

Shown in Fig. 4.10 are images captured and created with the receiver system of a modulated CCR at a distance of 50 meters away from the telescope receiver. In Fig. 4.10(a), the CCR is shown in the non-reflective (or inactive) state. In Fig. 4.10(b), the CCR is shown in the reflective state (or active) state. The CCR inside a transparent plastic box was mounted on a piece of transparent plexi-glass. The polygon-shaped plexi-glass mount, although transparent, became extremely bright when illuminated by the interrogating laser. The white wall behind the CCR also created a strong diffused reflection of the interrogating beam.

A casual observer would not easily be able to distinguish the difference between the two images because of the different bright spots (high noise) present in the background. The mean luminosities of the 8-bit digitized images in Fig. 4.10(a) and (b) were 112.95 and 112.90, differing by less than 0.5%. In other words, the CCR signal is less than 0.5% of total energy collected by the imager. Therefore, the signal-to-background is less than -40dB.

By subtracting Fig. 4.10(a) from Fig. 4.10(b), the CCR demonstration software

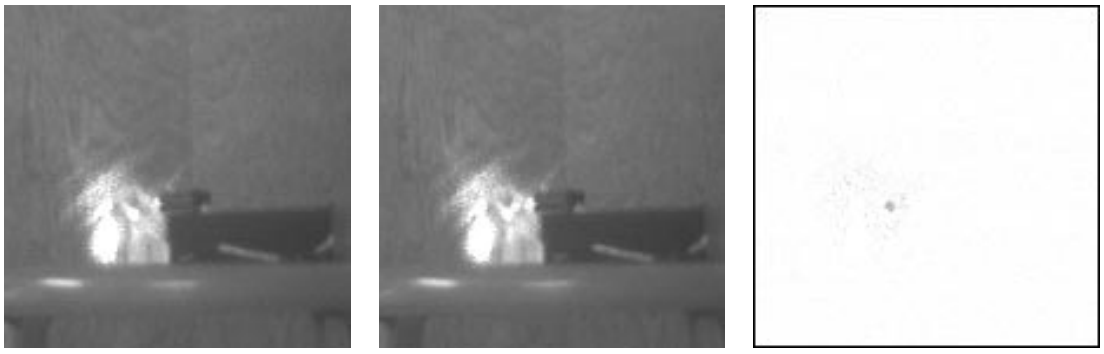

(a) (b) (c)

Figure 4.10: These images are captured or generated by the CCR demonstration software of a modulated CCR under interrogation at 50m away. (a) CCR is off. (b) CCR is on. (c) Image generated by subtracting (a) from (b). Note that the image is inverted to provide a clearer view of the spots.

created the image shown in Fig. 4.10(c). The mean luminosity of the difference image was found to be 1.16. The CCR's reflection was clearly visible in the generated image despite of the high background noise environment. Other small spots were also found in the generated image. Theses spots with lower intensities than the CCR spot were the "noise" in this detecting scheme, possibly due to fluctuation of the laser power supply or video camera and digitization noise. Vibration of the building and air current across the optical path may also contribute to this noise. In this particular case, the maximum intensity of these noise spots is about 10% of the maximum brightness of 255, or 25.5. However, the CCR's reflection was found to be more than 3 times brighter than these spots (greater than 80). Therefore, these spots can easily be eliminated with a digital threshold comparator at 10% or greater. And the CCR signal can be successfully retrieved from the image via software. The signal-to-noise using the spatial filter is increased from -40dB to 9.5dB.

Fig. 4.10 demonstrated how a software spatial filter may provide a solution to

(a) (b) (c)

Figure 4.11: These images are captured by the CCR demonstration software of two modulated CCR under interrogation at $45m$ away. (a) Both CCRs are on. (b) Only bottom CCR is on. (c) Only top CCR is on.

the problem of high background reflection. By taking periodic images of a scene which contains a modulated CCR and computing the "difference" image between consecutive images, it is possible to identify the modulated pixels corresponding to a CCR changing reflective state. However, a photo-detector array is necessary for this detection method. Additional computation power is then required for image processing.

4.4.6 Multiple CCRs imaging results

In Fig. 4.11, images of two modulated CCRs at different instances are shown. In Fig. 4.11(a), both of the CCRs were reflective; in (b) and (c), only one of the CCR was reflective. The mean luminosity of Fig. 4.11(a) was again less than 0.5% higher than that of Fig. 4.11(b) and (c); however, the mean luminosities of Fig. 4.11(b) and (c) were basically equal (within 0.01%). Therefore, it may be possible to detect CCR modulations based on the total intensity measured with a single detector; however, the independent modulations of the two CCRs cannot be distinguished unless sophisticated coding or modulation is used.

As shown in Fig. 4.11, the modulated reflections of the two CCRs were clear

(a) (b)

Figure 4.12: These inverted difference images (a) and (b) are generated by subtracting Fig. 4.11(b) from Fig. 4.11(a) and Fig. 4.11(c) from Fig. 4.11(a) respectively.

and distinct. Given snap shots like those in Fig. 4.11, state changes of each CCR are easily identifiable by taking image differences of two consecutive image frames, just as in the single CCR case. Communication with multiple CCRs may be accomplished with no additional hardware. Shown in Fig. 4.12 are images representing the differences in intensity between Fig. 4.11(a) and (b) and also Fig. 4.11(a) and (c). In both cases, a threshold filter at 30% is needed to remove all the "noise" spots. The signal-to-noise ratio was about 2.1.

4.4.7 Imaging with an optical filter

The images in Fig. 4.10 and Fig. 4.11 were taken under regular room lighting. The camera's automatic gain controller was active and no optical filter was used. In Fig. 4.13 are several images of the modulated CCRs taken with the optical bandpass filter. The filter appeared to remove all the room lighting successfully: only objects illuminated by the laser were visible. Because the average brightness of the image was very low, the camera's automatic gain was expected to be at its maximum (20dB). The background brightness was found to be about 6.7%. (In contrast, the value for Fig. 4.11 was about 55%.)

(a) (b) (c)

Figure 4.13: These images show two modulated CCR under interrogation at 45m away with an optical filter and camera AGC active. (a) Both CCRs are on. (b) Both CCRs are off. (c) Image (b) is subtracted from (a) and then inverted.

In Fig. 4.11 and Fig. 4.13, although both CCRs were mounted inside a plastic box, only one of them (bottom) has its lid closed. At these interrogation distances, the presence of the plastic lid did not cause noticeable degradation to the CCR's reflection. On the other hand, the internal reflection of the plastic case were more evident with the optical filter, indicating that a better packaging scheme was desirable.

Fig. 4.13 shows the image difference between the CCR "on" and "off" images. A significant portion of the background spots were removed. Unfortunately, the remaining spots had reasonably high intensity such that a 40% threshold filter was needed to remove the "noise" spots in the difference image. The resulted signal-to-noise level was about 2.5, which is only a small increase from the case where no optical filter was used (Section 4.4.6). The small SNR increase with the optical filter in Fig. 4.13 resulted from the non-linearity of the digitization of the video signal by the frame grabber board due to finite dynamic range. The amplified intensity of the CCR pixels were saturated to 255 such that the amplified intensity of the background scattering spots became comparatively stronger, thus yielding a lower SNR.

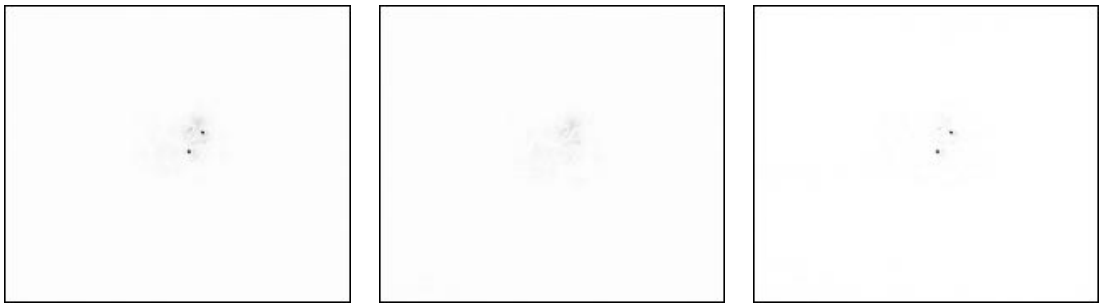

(a) (b) (c)

Figure 4.14: These inverted images show two modulated CCR under interrogation at $70m$ away. A bandpass filter was mounted on the camera and AGC was turned off. (a) Both CCRs are on. (b) Both CCRs are off. (c) Image (b) is subtracted from (a).

There are several solutions to this non-linear saturation problem. One solution is to change the gain control algorithm, such as setting the gain based on both the maximum pixel brightness and the average pixel brightness. Another solution is to use a camera with a larger dynamic range, although saturation could still potentially happen in that case. In our detection system, the gain controller of our camera unfortunately can only be externally controlled manually with two options, on and off. Therefore, we could not dynamically adjust the gain control to prevent saturation. As a result, most of the communication experiments were carried out with the optical filter mounted and the automatic gain controller turned off.

Fig. 4.14 showed inverted images of two modulated CCRs under interrogation at 70 meters with an optical filter but no AGC. All the images as shown are inverted. In these images, both CCR lids were opened. The CCR background was a bulletin board with different colors of posters, identical to the previous experiment, although the CCR was now closer to the bulletin board. Once again, the reflections from the two CCRs were clearly visible in the images. The general background appeared nearly black, about 0.78% of saturation, almost a factor of 10

less than the background in Fig. 4.13 where the gain was probably at maximum, which would be 10. A small halo, corresponding to the size of the laser spot, was also visible in the background. The ratio between intensity of the brightest CCR pixels and the brightest background pixels was about 4.2 for Fig. 4.14(a), although generally the ratio was 10 or greater. In Fig. 4.14(b), only 4.9% of the total luminosity was estimated to be from the two CCRs.

After the background lighting Fig. 4.14(b) was subtracted from (a), the ratio between the brightest CCR pixels and the brightest background pixel was increased to 7 in the difference image (Fig. 4.14(c)), while most of the background had zero brightness. Therefore, setting a threshold at 10% would remove all the noise in the difference image.

One problem with using the optical filter with an imager was that focusing the telescope became much more difficult because the image mostly consisted of spots and halos instead of shape features. Unless the laser happens to illuminate some easily identifiable objects, focusing the CCR reflections on the camera was often not trivial. If the optical filter were applied after a rough focus is first achieved, then focusing would not be as difficult. Unfortunately, in our case, the process of adding the filter was almost guaranteed to significantly mess up the focus of the camera. Moreover, the mechanical design of our telescope often prevented achieving a precise focus. As a result, the CCR reflections might became focused on two to four or more pixels. Different SNRs could be achieved depending on how well the camera was focused.

4.4.8 Communication results

With the camera's automatic gain controller disabled, successful communication with a CCR was achieved at different distances up to 150 meters (500 feet). Data was transmitted at only 4bps due to the hardware speed limitation. Based on our device capacitance measurement (Section 3.3.5), $16nW$ was consumed to actuate the mirror actuator.

For distances less than 100 meters, communicating with 2 CCRs simultaneously could also be achieved easily, as long as the interrogating laser could shine on both CCRs. However, for larger distances, communicating with two CCRs became more and more difficult. The reason was that the two CCRs had slightly different orientations. As a result, getting good optical response from one CCR often led to poor response from the second CCR at large distances.

In most of our experiments, establishing a communication link with the CCR unit was relatively easy. We first aimed the laser at the remote CCR unit, then we turned the CCR unit so that the CCRs are roughly facing the direction of the laser and the telescope. (The CCR unit acted as a cooperative target.) In most cases, the laser incident angle to the CCR was probably within a few degrees from the (111) ideal direction. It was, however, impossible to know the exact angle due to the unprecise position and orientation of the telescope on which the laser was mounted and the unknown orientation of the CCRs which was dependent on the rough visual alignment and by the angle of the non-uniform floor.

Even though the interrogating laser incident angle did not have to be precise, alignment between the CCR and the interrogating laser was found to have an important effect on successful data transmission, especially when the communication distance was greater than 100 meters. For example, we discovered that the

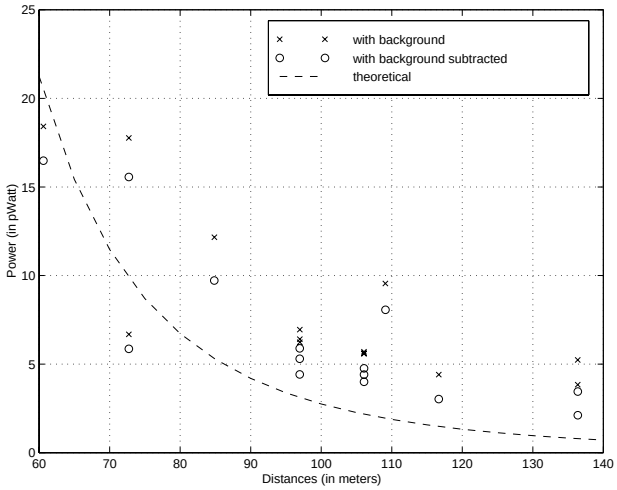

Figure 4.15: Intensity of the CCR reflection was measured at different interrogating distances using the CCD camera. The measured value was found to be strongly depended on not only distance but also CCR orientation.

weight of a person could flex the floor panel sufficiently to misalign the CCR unit and break a successful communication link. Because of this alignment sensitivity, the increase in CCR signal strength (and SNR) were not necessarily found to be consistent with decreasing communication distance.

Fig. 4.15 shows the CCR signal strength measured at several different communication distances compared to theoretical values. At each distance, after successful communication was demonstrated, images of the CCR at both "on" and "off" states were captured. The total intensity level for each CCR reflection in the "on" image was calculated by summing the intensity (less than or equal to 255) of all CCR pixels and multiplying by the camera's power conversion factor. (From calibration test, it was found that the least significant bit (LSB) corresponded to about $0.01pW$.) We also computed the total intensity level for each CCR reflection found in the "difference" image created from the "on" and "off" images. Note

that some of the pixels in the images for short distances were saturated. Therefore, the calculated intensity may be smaller than the actual reflected intensity. The theoretical values of the incident CCR power at the detector, $P_{CCR-inc}$ were computed using expressions derived in Section 2.3.1 for a $275\mu m$ CCR with $20mrad$ divergence and 85% reflectivity.

As expected, the intensity values computed from the "difference" images were smaller than the corresponding values from the "on" images. The intensity difference represented the background light which was not modulated by the CCR. In other words, the CCR surrounding also contributed small amount of light to the CCR pixels, despite the spatial separation.

Both sets of experiment data were found to be larger than the theoretical estimates. This is probably due to the inaccurate calibration of our CCD camera, where the reference power meter only had one significant figure. Nevertheless, the measured values seemed well within the expected power range from simulation. However, the results did not match our theoretical expectation in the sense that the decease in detected intensity did not show a strong fourth power of the distance according to Eq. 2.22. Many factors contributed to these non-ideal results, including the inconsistent orientation of the CCR, the non-uniformity of the interrogating laser beam, and the saturation of some of the CCD pixels which we have mentioned earlier.

Nevertheless, the results in Fig. 4.15 demonstrates an important point. Despite of the CCR signal intensity's strong dependence on the orientation of the CCR, it is clear that without precise alignment between the CCR and the interrogating light, communication is still possible. The unique optical property of CCRs makes CCRs ideal for this communication application. On the other hand, to create a

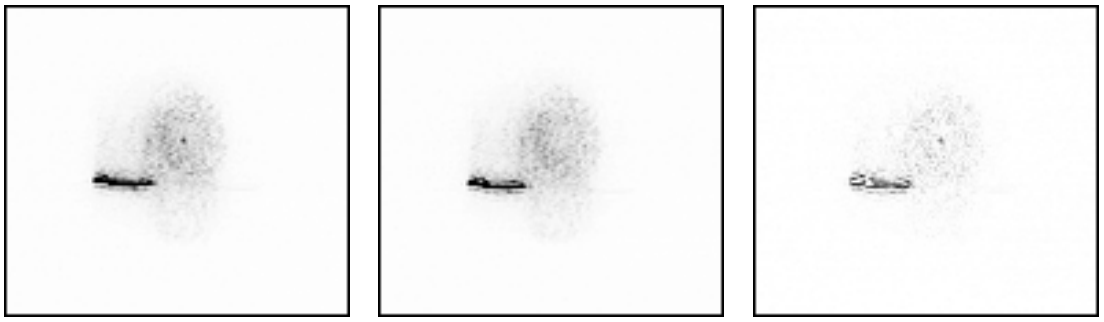

(a) (b) (c)

Figure 4.16: These images show a modulated CCR under interrogation at $136m$ away. Images were taken with a bandpass filter and no AGC. (a) CCR is on. (b) CCR is off. (c) Image (b) is subtracted from (a).

truly robust communication link, a CCR unit should have multiple CCRs facing different orientations, then the unit will be able to respond to interrogating lasers from all directions.

From images which we captured, we also learned that our simple image subtraction algorithm had some drawbacks. As an example, Fig. 4.16 shows the "on" and "off" images of an interrogated CCR at 136 meters. Again, all these images are inverted to create a clearer presentation. The "difference" image is also shown. The bright line which is visible in all three images resulted from the reflection of the laser beam by the edge of the mirror which was used to extend the optical path of the interrogation. The "difference" image showed that the image subtraction failed to remove completely the bright line and many small spots around the CCR, although in general, each background pixel intensity was decreased by 50% to 70%.

The poor subtraction result was largely due to room vibration, although air motion may also be a factor. Because of this problem, we found was that the software would find false CCRs in the image as the communication distance increased.

Since the false CCR reflections contained no useful information, theoretically one could create more intelligent software to identify them. However, we found that we could establish successful communication in these long distance test without modifying our software. Instead, we set the interrogating area not to include the bright line. Furthermore, we set the threshold limit to a high value, like 40% (about 100) or higher. For the case of Fig. 4.16 where the interrogating distance was 136 meters, the brightest CCR pixel in the "difference" image has an intensity of only 52.5% (134); therefore, successful data transmission with no false CCR detection was just barely possible. The largest distance we successfully achieved was 150 meters; however, larger distances than 150 meters were not attempted.

5 CMOS Corner Cube Reflectors

We have conducted a preliminary study of using CMOS technology to fabricate micro CCRs. Although the CMOS process was not originally designed to fabricate mechanical structures, it offers many interesting design possibilities. In this work, we focused on creating structures made of silicon dioxide, aluminum, and polysilicon by chemically removing selected parts of the supporting silicon substrate. Large suspended plates connected to the substrate by metal interconnects or oxide beams were fabricated. Using carefully designed metal interconnects as metal hinges, large released plates were rotated from the substrate to form three-dimensional corner cube reflectors.

To fabricate micro CCRs for communication in CMOS, we need to develop micro mechanical components including large mirrors, hinges, alignment and locking mechanisms, and micro actuators as we have done for the MCNC's MUMPS process. In this work, we designed and fabricated these components, although not including micro actuators, using the Orbit $2\mu m$ CMOS process through the MOSIS Foundry Service. The CMOS structures were released using a novel etching process using xenon difluoride (XeF_2). Without actuators, only static CCRs were made. However, these CCRs can be integrated with actuators developed elsewhere [52] to form modulatable CCRs.

5.1 Micromachining with CMOS

The $2\mu m$ Orbit CMOS process is a standard CMOS process with four conducting layers (2 polysilicon and 2 aluminum), and 5 insulating layers (all oxide layers) which is suitable for fabricating both analog and digital circuits [11]. Fig. 5.1 shows

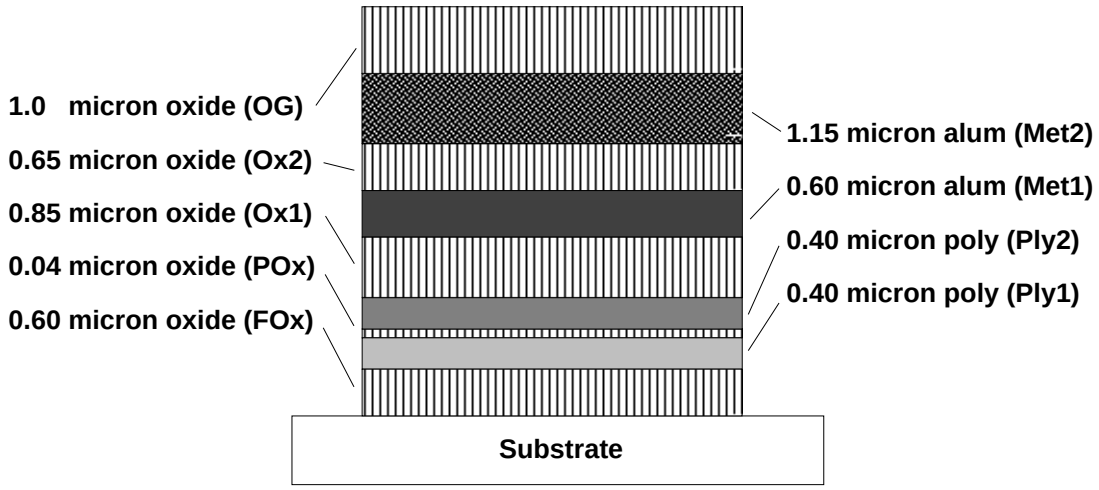

Figure 5.1: Cross-sectional view of the layer structure for the $2\mu m$ Orbit CMOS process is shown. Note that the exact thickness of each layer in a stack of layers varies depending on the exact composition of the layer stack.

a cross-section of all the layers stacked on a substrate with the corresponding ideal thickness information. In contrast with MCNC's MUMPS process, the polysilicon layers are only a small fraction of the total layer stack in thickness. The oxide and metal layers are the dominating layers in this case. In this section, we will explain how to create mechanical structures using this CMOS process.

In this CMOS process, all the conductor layers can ideally be patterned to a specified geometry according to the layout submitted to MOSIS as long as a set of design rules are followed. Interconnections between these layers and with the substrate are also possible by using the appropriate via and contact layers which define the holes in the oxide layers. Since the poly and metal layers are generally required to have small features in integrated circuits, the minimum line width and spacing for the polysilicon layer and the metal layers are relatively small, 2 and $3\mu m$ respectively. The vias and contacts also have $2\mu m$ line-width and spacing.

The oxide layers can be patterned with one or multiple via and contact layers.

A deep oxide cut through several oxide layers generally requires stacking several different via and contact layers. For best results, the sizes of these stacked should increase incrementally according to the order of the oxide layers, with smaller via and contact cuts for the lower oxide layer and larger openings for the higher oxide layer. Patterning of an oxide layer or conductor layer may also cause the underlying oxide layer to be partially etched. As a result, the sidewalls and thickness of the oxide layers in general are not as well defined as for the conductor layers. As an example, cantilevers composed of different layers were reported to have thicknesses a few percent to 20 percent less than the ideal thicknesses [96]. Some cantilevers were also found to be completely over-etched.

By stacking the various contacts, large areas of the silicon substrate can be exposed. The exposed silicon areas as well as their surrounding areas can be chemically etched away. To facilitate design and fabrication of suspended structures on CMOS which require exposed silicon area, MOSIS added an "open tile" or "pit" layer to the CMOS design rules [66]. The *Open* layer has a minimum width of $5\mu m$ and a minimum spacing of $8\mu m$ and is composed of several via and contact layers including the overglass opening, $Met2-Met1$ contact, $Met1-Ply$ contact, the active area layer (Field Ox opening), and the active contact ($Met1$-Active area contact).

Using the Open Tile, suspended oxide and aluminum micro structures can be created [73, 81]. Shown in Fig. 5.2 is an example of an oxide plate with embedded metal which can be fabricated in CMOS. The sides of the oxide plate is defined by the bare-silicon pit area. After the chip is etched using a silicon etchant which is selective against oxide (and also aluminum in other cases), the silicon underneath the oxide plate is removed and the oxide plate becomes a suspended structure.

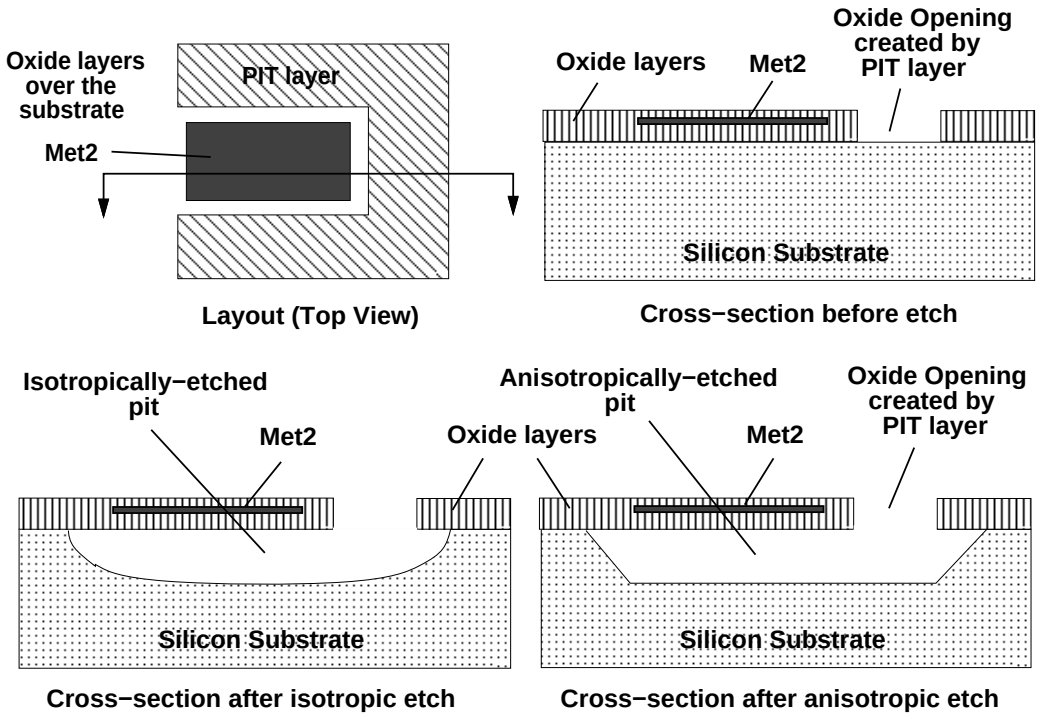

Figure 5.2: Process steps to create a suspended oxide plate is shown. The shape of the oxide plate is defined by the *PIT* layer in the layout. After the chip is fabricated and returned by MOSIS, the silicon underneath the oxide plate can be chemically removed. Depending on the etchant used, pits with different shape will be created during the etch.

A benefit of the fabrication approach shown in Fig. 5.2 is that only one post-process etch step is required to create MEMS structures with standard CMOS. No additional masking or lithography step is needed as long as the etchant used is selective against aluminum and oxide. Many other techniques are in fact available for fabricating MEMS structures using CMOS as discussed in Section 1.4 and Section 5.3. However, we found that this basic fabrication approach shown in Fig. 5.2 is in fact very suitable for micro CCR development. While exploring other approaches could also be beneficial, we were only able to explore this fabrication approach in this work. Details regarding the post-process chemical etch will be

presented in Section 5.3.

5.2 Building blocks for CMOS CCRs

Similar to the polysilicon CCR designs, we would like to create CMOS CCRs by folding up mirror plates and locking them to form 90 degree angles. Therefore, we created hinged plates and alignment mechanisms for these plates. We also studied different mirror designs to create flat mirrors. We will describe our CMOS results in the following sections.

5.2.1 Micro mirrors

The CMOS process was originally designed to fabricate integrated circuits; therefore, mechanical properties of the films such as stress of the films were not important concerns. To fabricate useful corner cube reflectors in CMOS, we would like to find out if it is possible to fabricate flat mirrors despite the film stresses. Mirrors with several different layer combinations were fabricated. Reported reflectance for aluminum films is greater than 95% for long wavelengths (greater than $1\mu m$)[20]. For wavelengths between 0.2 to $1\mu m$, the reflectance is above 85%.

The curvature of the fabricated mirrors was measured using a Wyko white light interferometer (Fig. 5.1. The layer combinations which we used, however, only represent a small subset of all the possible combinations. Therefore, the results here are not conclusive although still useful. We found that it is indeed possible to make CMOS mirrors with comparable curvature to polysilicon mirrors in Section 3.1.2.

Fig. 5.3 shows the cross-sectional view of some of the fabricated mirrors. These mirrors include metal mirrors with oxide frames and metal mirrors embedded in

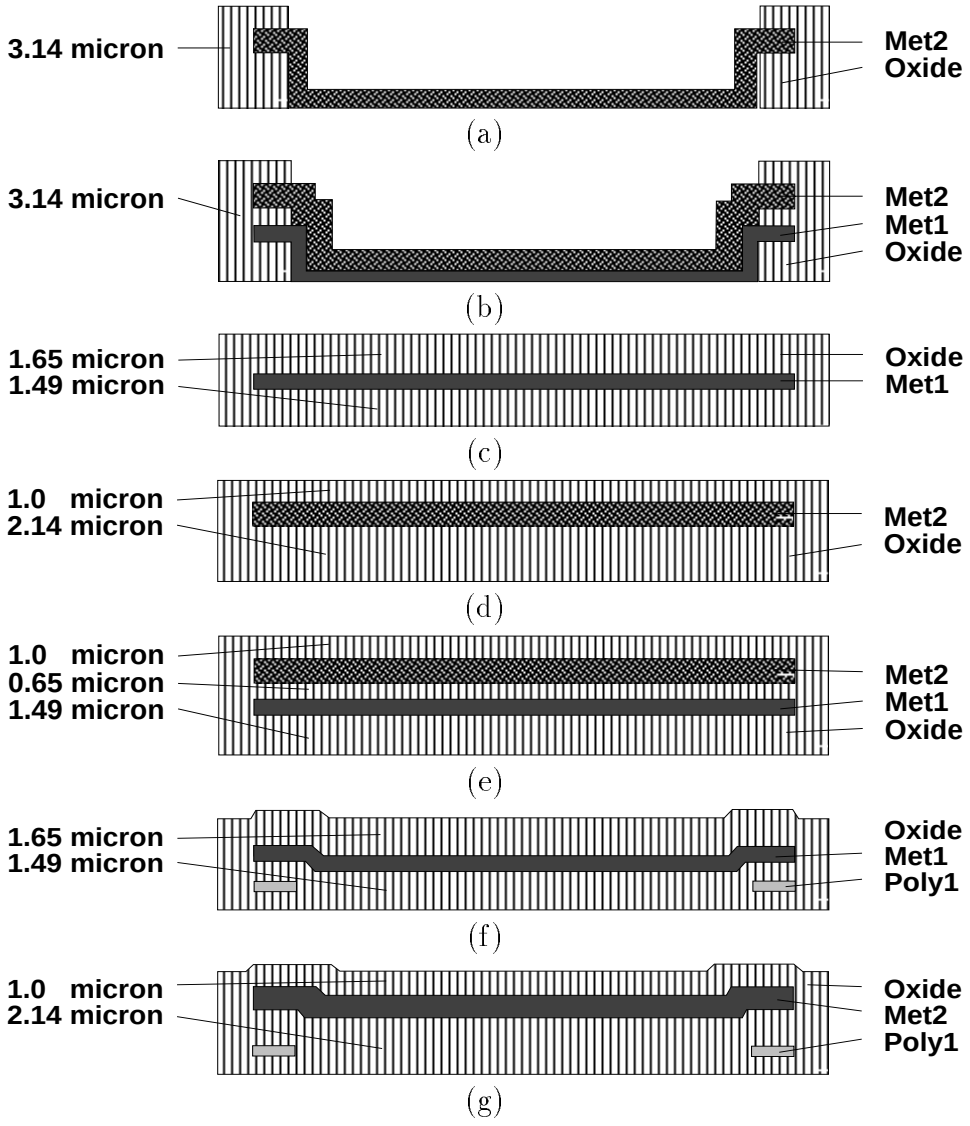

Figure 5.3: Cross-sectional views of various fabricated CMOS mirrors are shown. These figures are not drawn to scale. The oxide thicknesses are based on the ideal values given in Fig. 5.1. The mirror curvature results of the fabricated mirrors are shown in Table 5.1.

Figure	Composition	Curvature(mm)	Comments
5.3(a)	$Met2$		oxide frame, astigmatic
5.3(b)	$Met1 + Met2$		oxide frame, astigmatic
5.3(c)	$Met1$	15	ox plate, concave down
5.3(d)	$Met2$	4	ox plate, concave up
5.3(e)	$Met1 + Met2$	3.5	ox plate, concave up
5.3(f)	$Met1$	3.55	ox plate, poly frame, concave up
5.3(g)	$Met2$	2.8	ox plate, poly frame, concave up

Table 5.1: The curvature results for the fabricated CMOS mirrors are shown. These results, which correspond to $200\mu m$ mirrors with cross-sections shown in Fig. 5.3, were collected using a Wyko white light interferometer.

oxide. The metal mirrors with oxide frames have $190\mu m$ square aluminum membranes with $25\mu m$ width oxide frames so that the overall mirror size was $(200\mu m)^2$. As shown in Fig. 5.3(a) and (b), the metal membranes were made of the $Met2$ layer or the $Met2$ layer contacted to $Met1$. These mirrors were created by placing a $150\mu m$ square "Open" layer in the center of the mirror layout shown in Fig. 5.2. The advantage of this design is that incident light can directly shine on the reflective metal surface. Note that it is not possible to make a $Met1$ membrane because patterning of the $Met2$ layer, which would be deposited directly on the $Met1$ layer due to the lack of the $Ox2$ layer, will remove the $Met1$ layer.

The metal mirrors embedded in oxide were made of $200\mu m$ (or $250\mu m$) square oxide plates enclosing either $Met1$, $Met2$, or both metal layers (Fig. 5.3(c), (d), and (e)). These mirrors are created using the basic mirror layout shown in Fig. 5.2. Variation of these mirrors were created by adding a $15\mu m$ width polysilicon frame under the metal mirror (Fig. 5.3(f) and (g)). $10\mu m$ or $12\mu m$ etch holes have been used to reduce release etch time, although plates with dimensions of $200\mu m$ with no etch holes could also be successfully released (Section 5.3).

Table 5.1 shows results of fabricated $200\mu m$ square mirrors. The mirrors with

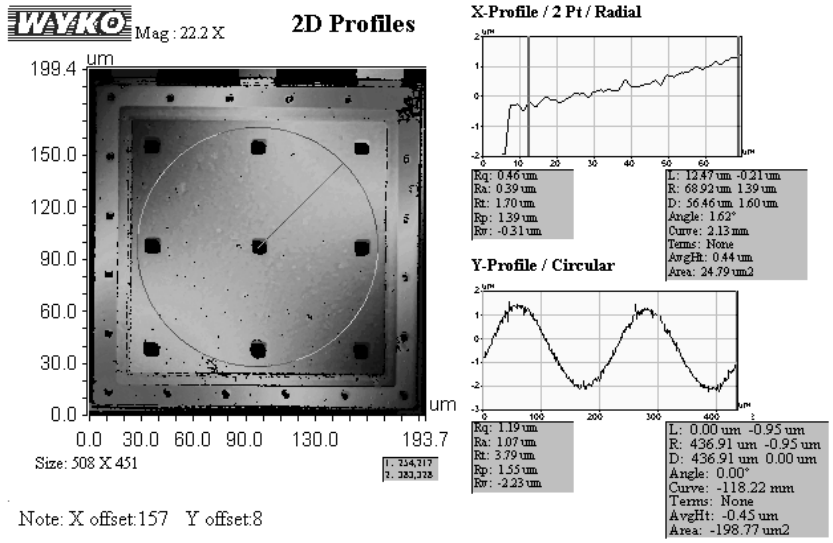

(a)

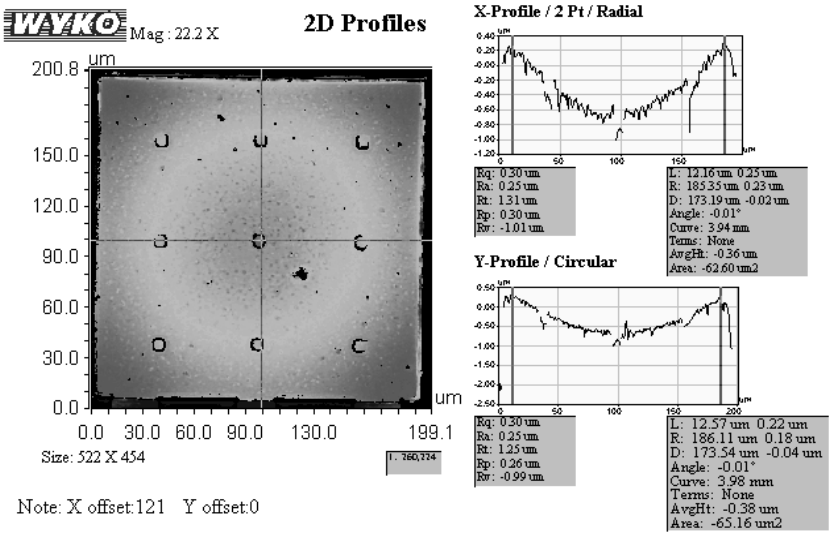

(b)

Figure 5.4: (a)The 2-D profile of an astigmatic CMOS square mirror with $200\mu m$ sides is shown. The cross-section of this mirror is shown in Fig. 5.3(b). (b)The 2-D profile of a typical concave CMOS square mirror with $200\mu m$ sides is shown. The cross-section of this mirror is described by Fig. 5.3(d).

only oxide frames as support (Fig. 5.3(a) and (b)) were found to be severely distorted, forming an astigmatic or toric surface [32]. Radii of curvature measured across the diagonals of these mirrors ranged from 1.4 to 2.8mm. An example of an astigmatic mirror profile is shown in Fig. 5.4(a). This image is taken from a released mirror with cross-section shown in Fig. 5.3(b). Most of the other mirrors formed symmetric concave surfaces with still undesirably small radius of curvature (about 3.5 to 4mm). An example of a concave mirror profile is shown in Fig. 5.4(b). This image is taken from a mirror with cross-section shown in Fig. 5.3(d).

The flattest fabricated mirrors have only $Met1$ encased in oxide, with curvature ranging from 15mm up to almost 80mm for 200μm square mirrors. The large radius of curvature for these mirrors is due to the large thickness of oxide (which is compressive) compared to that of aluminum (which is tensile). The large variation is due to the CMOS process variation and the curvature's sensitivity to the balance of the film stresses in the composite plate.

Table 5.1 also indicated that the oxide mirrors with polysilicon frame have small radii of curvature despite of the addition of a polysilicon frame. It is important to note that the mirror area with polysilicon was actually found to be very flat. Therefore, the radius of curvature measurements were taken from the region inside the poly frame instead of the whole mirror so that a fair comparison cannot be made. These fabricated mirrors, however, strongly indicated that the polysilicon layers should be used to counteract the metal stresses. With the addition of one or two polysilicon layers in the mirror stack, it may even be possible to expose the aluminum surface by removing the overglass layer without decreasing the radius of curvature of the mirror. Therefore, successful fabrication of CMOS mirrors with good optical quality is promising.

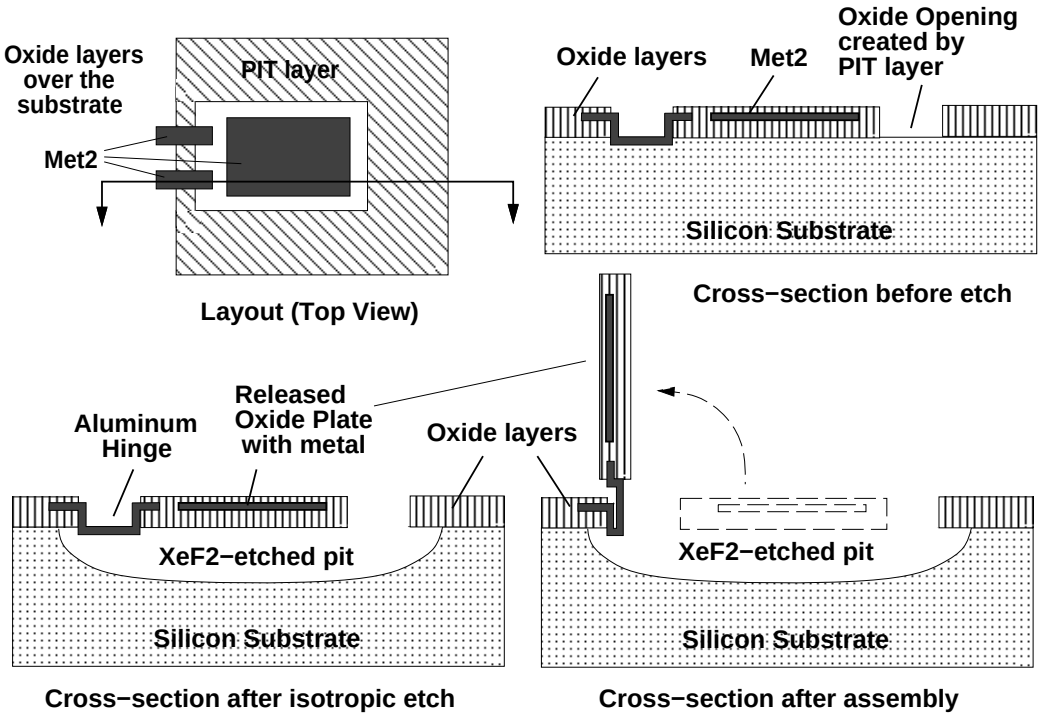

Figure 5.5: Process steps to create a hinged oxide plate are shown. The oxide plate is defined by the PIT layer in the layout. Two $Met2$ beams link the isolated oxide plate to the surrounding oxide area. After the chip is fabricated and returned by MOSIS, the silicon underneath the oxide plate and the aluminum beams is chemically removed using XeF_2. The oxide plate can then be rotated upward.

5.2.2 Aluminum micro hinges

Fig. 5.5 shows the layout for an oxide plate which is free to rotate after the sacrificial silicon substrate is removed. Similar to the plate in the Fig. 5.2, this oxide plate is defined by several rectangular regions of bare silicon area. In this case, the center oxide plate is completely isolated from the surrounding oxide except for the metal interconnect which forms a bridge across the bare silicon area. After the release etch, the oxide plate becomes suspended over the silicon pit by the aluminum interconnect. Since the aluminum beam is flexible, the plate can be rotated away from the substrate while the aluminum beam becomes plastically

deformed (Fig. 5.5). In essence, the aluminum beam acts as a hinge for the oxide plate.

An aluminum hinge can be created using $Met2$ (hinge thickness would be $1.1\mu m$) or $Met2$ contacted to $Met1$ (hinge thickness would be $1.75\mu m$). Due to the layer order of the metal layers (Fig. 5.1), an aluminum hinge naturally has a sharp bend at the edge of the oxide plate to which the hinge is connected. This non-ideal hinge topology can be observed in the cross-section illustrations in Fig. 5.5. The sharp bends as shown are also contributed by the over-etching in the CMOS process, where the exposed silicon area on which the metal beams rest are often etched by more than $1\mu m$. Because of this topology, it is most common for the hinge to bend near the oxide edges. Despite the large stresses which are present at the bent locations, aluminum hinges were demonstrated to survive cycles of large bending while maintaining good electrical properties [52].

To create hinged structures with precise mechanical alignment, it is desirable to make the aluminum hinge bend at only a specific location. One method is to make the beam more narrow at the desired bending location than the other parts of the beam. Another method is to use double metal layers to form the hinge except for the area where bending is desired to occur [61].

Fig. 5.6 shows two metal hinges which are connecting two released plates to the substrate. The plate on the right is resting parallel to the substrate, while the plate on the left is lifted up to a near vertical position. These hinges are $10\mu m$ long and $35\mu m$ wide. We found that these hinges were reasonably rugged and did not easily break during plate rotation. We also found that even though the hinge would naturally bend at the desired (narrower) end, the hinge could also bend at the other end if the plate is pressed incorrectly with the probe tip during assembly.

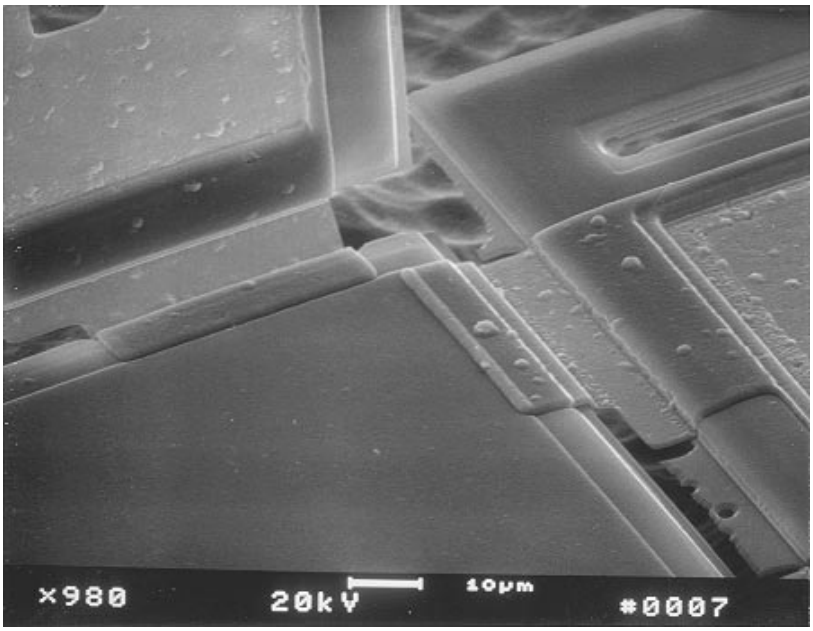

Figure 5.6: Close-up view of the metal hinges which allows the rotation of the mirror plates. The hinges are made of a $1.1\mu m$ aluminum layer.

Shorter and wider hinges are generally desirable because of their strength. However, the unetched oxide found next to the right hinge in Fig. 5.6 suggests that short hinge designs could potentially be problematic. As shown in the figure, the CMOS process failed to completely remove the oxide in a $10\mu m$ wide pit area, even though the design rules only required $5\mu m$ openings. This is a particularly serious problem if an anisotropic wet etchant is used to release the structure. In our case, since we used an isotropic gas etchant (XeF_2), we never experienced any problems with this design.

5.2.3 Mechanical alignment aids

Using micro mirrors and hinges described in the previous sections, we can create hinged mirrors to form the vertical mirrors of a CMOS CCR. Unlike the polysilicon

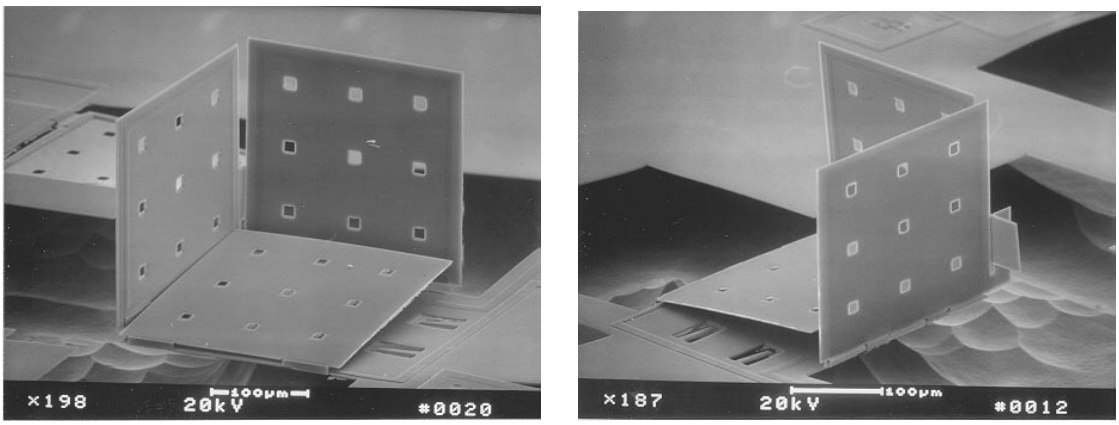

(a) (b)

Figure 5.7: The front (a) and rear (b) views of a CMOS CCR is shown. This CCR made of oxide, aluminum, and polysilicon, has dimensions of about $250\mu m$. The two vertical mirrors are aligned together by sliding a stub of one plate through a slide on the second plate.

hinged mirrors, the CMOS hinged mirrors do not necessarily need to be locked to remain in a vertical position because the aluminum hinges are plastically deformed when bent by a large angle. However, it is still necessary to make sure that the two vertical mirrors are well aligned with each other and with substrate.

Fig. 5.7 shows a fabricated CMOS CCR. This CCR has two vertical mirrors and a rotated mirror which could be used to modulate incident light like the polysilicon actuators in Section 3.1.4. The actuated base mirror as shown, however, is not functional. The two vertical mirrors are aligned with each other using an alignment stub and slit similar to the ones used in the polysilicon designs (Section 3.1.4). From the rear view of the CCR in Fig. 5.7, we can see the stub (or tenon) of one mirror which was slid into a slit (or mortise) of the other mirror.

The thickness of the stub (assuming no over-etching) was about $3.14\mu m$. The width of the slit was designed to be $4\mu m$, although the fabricated slit might be more narrow because the oxide cut forming the slit did not necessarily remove

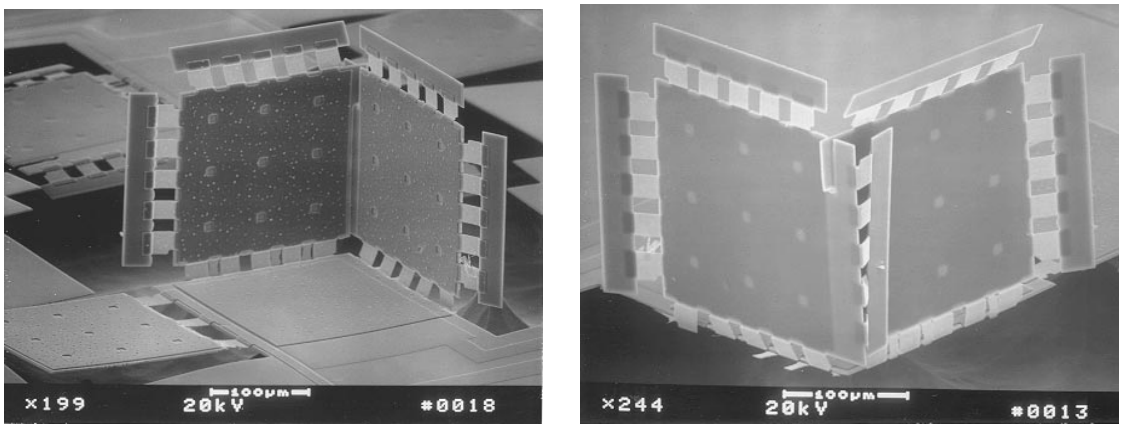

(a) (b)

Figure 5.8: The front (a) and rear (b) views of a different CMOS CCR is shown. The alignment stub and slit are located near the top of the mirror plates. Stiffeners made of oxide and poly are added to the edges of the mirrors, although they were not found to affect the mirrors' curvatures.

all the oxide. This effect is more evident in the alignment slit on the right plate in Fig. 5.6. However, it is possible for this oxide residue to become completely detached from the plate when the stub is pushed through the slit. Therefore, the oxide residue generally was not found to prevent successful assembly of the mirrors.

On the other hand, we found that the design of the plate extension where the slit is located could cause problems. Because of the weak support near the base, the plate extension would break if a probe tip pushes against it during assembly. Another undesirable feature of this alignment design is that it is hard to know if the mirror with the slit is rotated adequately. In other words, even though the vertical mirror with the stub is well aligned to the substrate, the other vertical mirror could be misaligned. Therefore, the alignment of CCRs with this design largely depends on the assembly process.

A different alignment stub and slit design is shown in the CCR in Fig. 5.8. In this design, the alignment stub and slit are located near the top of the mirror plates

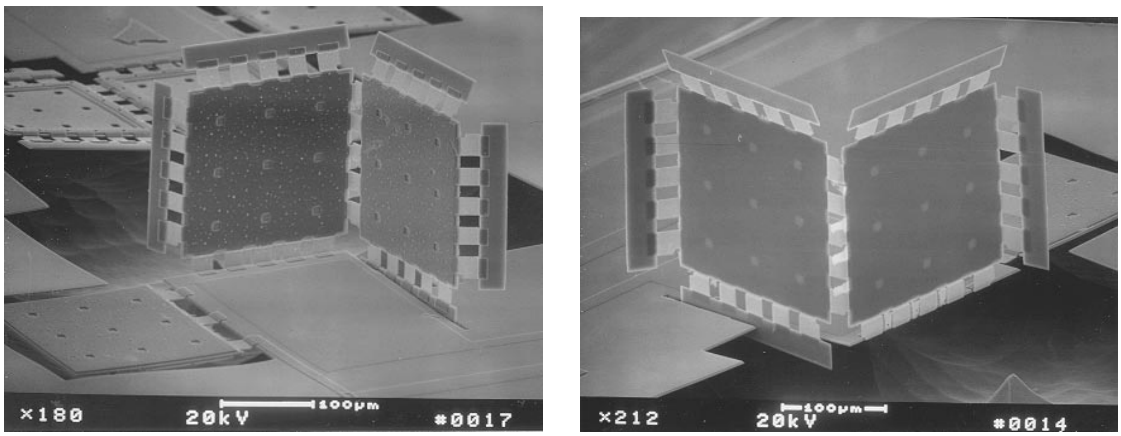

(a) (b)

Figure 5.9: The front (a) and rear (b) views of a CMOS CCR with linked-mirrors is shown. In this CCR, the two vertical mirrors are linked together by hinges. The long alignment slit is located on the substrate such that the one edge of the hinged mirror is rotated through the top surface of the substrate.

so that more accurate alignment could be achieved. Similar to the other design, the stub is about $3.14\mu m$ thick. However, the slit was designed to be $5\mu m$ wide, following the design rule. Even though the slit is wider, this design was found to be more rugged than the previous design since the slit is only a small section of a continuous plate. Another advantage of this design is that the edge of one mirror rests against the side of the other mirror. Therefore, it is easy to know if the both plates are adequately rotated. Moreover, there is no gap between the two vertical mirrors after assembly.

Fig. 5.9 shows a CCR with an alignment design which is very different from the other design. In this CCR as shown in Fig. 5.9(a), the right vertical mirrors is hinged to the left vertical mirror. When the left vertical mirror is rotated to a vertical position, part of the right mirror enters a long slit on the substrate. As shown in Fig. 5.9, the vertical plates show excellent orthogonality; however, both mirrors are slightly misaligned from the substrate because the left mirror (in

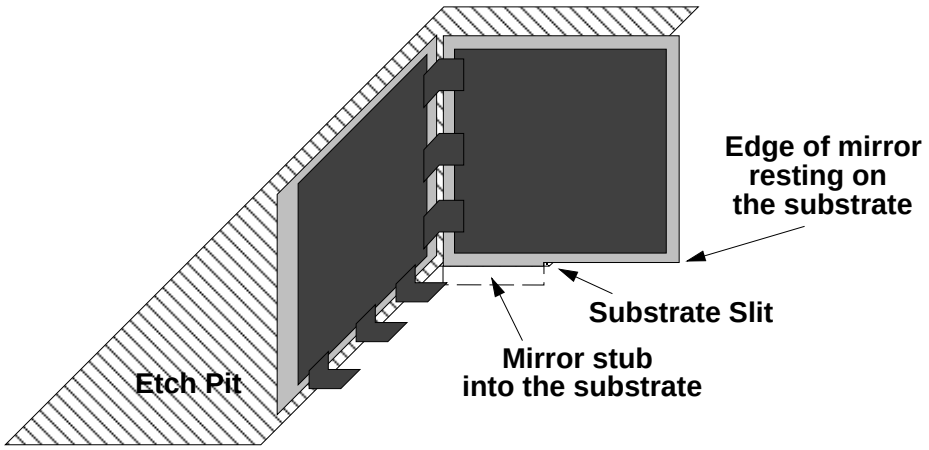

Figure 5.10: Illustration of alignment design improvement for the CCR in Fig. 5.9 is shown.

Fig. 5.9) was not rotated adequately. The problem with this present design is that it is difficult to know whether the mirror which is hinged to the substrate is rotated sufficiently.

The CCR design in Fig. 5.9 can be improved with several minor modifications. The mirror stub or extension should be made from a continuous plate like the stub in Fig. 5.8. Furthermore, the mirror with the stub should be shaped so that instead of the whole bottom mirror edge going through the slit, part of the edge would rest on the substrate as shown in Fig. 5.10. In that case, over or under-rotation of the substrate-hinged mirror would be prevented.

Similar to the CCRs in Fig. 5.7, the mirror alignment of the CCRs in Fig. 5.9 as well as in Fig. 5.8 was also largely dependent on how carefully the CCR was assembled. For the later designs, the main reason is that the hinge lengths were simply too long and could easily bend incorrectly. Therefore, the hinge length of the CCRs with either designs should also be significantly reduced. Then CCRs with precise alignments would be possible.

5.3 Fabrication of CMOS microstructures

Layout of the CMOS CCR designs are electronically submitted to MOSIS for fabrication. Fabricated dies are generally delivered between 8 to 10 weeks. The CMOS CCR dies could ideally be packaged and bonded before the post-processing etch and assembly process. We did not do so because the CCR test structures were usually crowded on the die to yield a large number of test structures per die. If all the devices were bonded, the bondwires inevitably would cross over one or more structures, adding unnecessary complications to the assembly process. Therefore, the CMOS dies were post-processed with no packaging. In the following sections, we will discuss post-processing of CMOS chips including bulk etching and assembly of microstructures.

5.3.1 Bulk etching of CMOS chips

The chips from the CMOS process must be post-processed by etching away the silicon to which our oxide and metal structures are attached. Many different options are available for etching bulk silicon. In our application, we must use a process which would cause minimal damage to oxide and metal (aluminum) which are used as the MEMS structural materials. Anisotropic etchants including ethylenediamine-pyrocatechol (EDP) [71] and pH-controlled tetramethyl ammonium hydroxide (TMAH) with water and dissolved silicon [83] were found to preserve oxide and aluminum (protected by native aluminum oxide) effectively. Potassium hydroxide (KOH) may also be used if the aluminum layer is properly protected, such as using electroplated gold [80] or oxide passivation layers [42]. Conventional plasma etching could also be used to etch silicon, but in general,

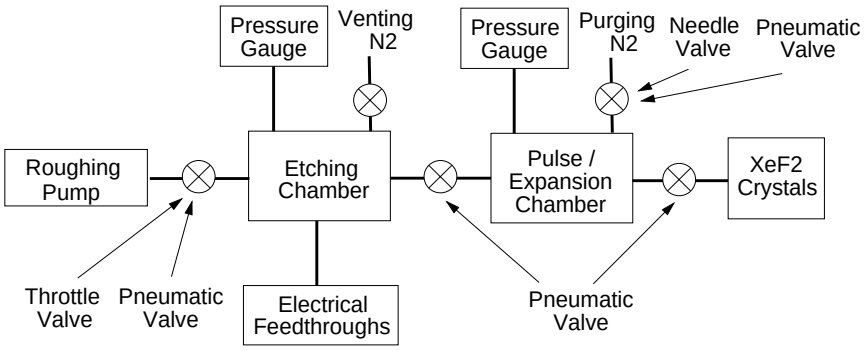

Figure 5.11: Block diagram of the XeF_2 etching system used to post-process the CMOS chips.

plasma etches do not have high selectivity against oxide [97]. Therefore, an additional masking layer is needed [25].

To etch our CMOS chips, we used an isotropic dry-etching process with xenon difluoride (XeF_2) [14]. XeF_2 is a member of a family of fluorine-based silicon etchants which includes ClF_3, BrF_3, BrF_5 and IF_5. All of these compounds can be used for vapor-phase chemical etching of silicon [39, 40]. XeF_2 and BrF_3 both exhibit very high etch rates for silicon at room temperature, yet zero or near zero etch rate for oxide and aluminum [97, 14, 95]; therefore, these etchants are very suitable for CMOS. The isotropic nature of the etchant also allows quick undercut and release of the structures. Moreover, dry etching is advantageous compared to wet etching because the microstructures do not have to experience large fluid forces present in a wet bath.

At room temperature, XeF_2 has a sublimation pressure of about 4 Torr. The overall reaction equation for the Si/XeF_2 reaction is the following:

$$2XeF_2 + Si \rightarrow 2Xe + SiF_4 \tag{5.76}$$

We used XeF_2 as a vapor-phase etchant by placing XeF_2 crystals in high vacuum

(about $10mT$) where the crystals sublime to gas and then exposing the gas to our CMOS chips. We had initially used a simple vacuum system as an etcher. Unfortunately, we found that direct exposure of the XeF_2 crystals to the etch reaction often caused the crystals to stop subliming after a period of silicon etching. We believed that the crystal surfaces become contaminated by the moisture and various chemicals present in the etching chamber. Therefore, we developed a technique called controlled pulse-etching where the vapor from the crystal expanded into a designated chamber, and only pulses of XeF_2 vapor were exposed to the etched sample. The block diagram of the system is shown in Fig. 5.11. With this system, we were able to release CMOS structures quickly and reliably [62, 21, 53]. Details of this etching system are described elsewhere [14].

The CMOS chips generally needed no special preparation before etching. However, we found that some CMOS chips with no preparation would only be partially etched. In these cases, white scum would often appear on the silicon surface. However, CMOS chips which were given a dehydration bake on a hot plate shortly prior to etching. Baking generally prevented this problem. A short buffered hydrofluoric acid (BOE) dip may also be used prior to etching to clean the silicon surface. In this work, BOE dip, however, was rarely applied.

In general, about 20 to 25 one-minute etch pulses (about 30 minutes of etching) are needed to release $200\mu m$ square oxide plates with no etch hole. Etch pits may have depth greater than $50\mu m$. Fig. 5.12 shows a CMOS corner cube reflector on a MOSIS chip after being etched in XeF_2. Because of the isotropic nature of the etchant, bond pads should be placed far away from an etch pit opening. Otherwise, the chip should be bonded before the release etch.

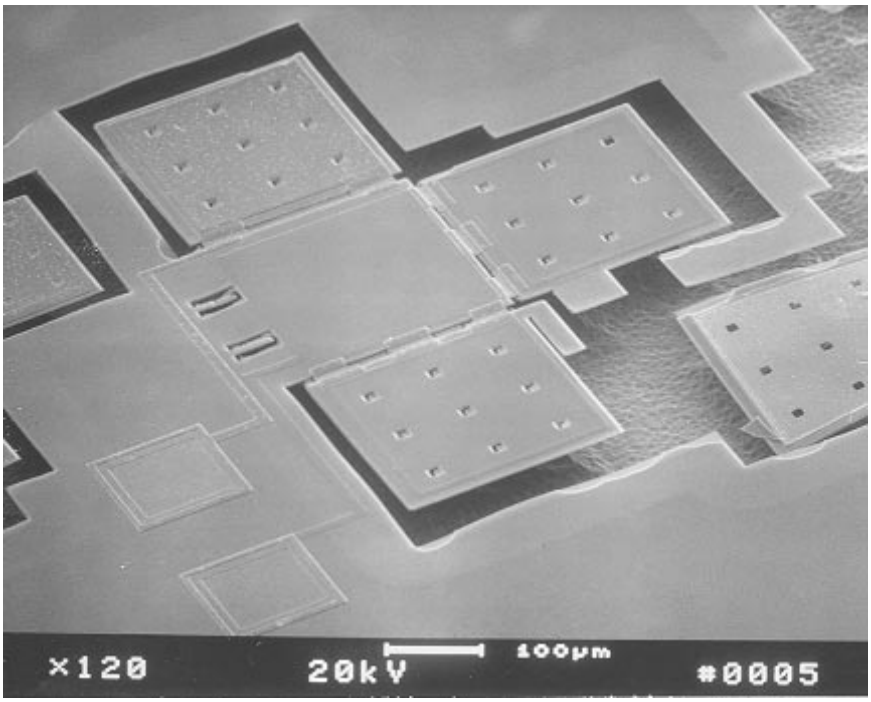

Figure 5.12: The top view of the CMOS CCR in Fig. 5.7 before being assembled. The CMOS chips was etched in XeF_2 to remove the supporting bulk silicon.

5.3.2 Manual assembly

The manual assembly process for the CMOS structure is similar to that of the polysilicon structure. The CMOS structures are assembled using micro-manipulators under a microscope. To lift up a plate, one must carefully place a probe tip underneath the plate and slowly raise the tip, guiding the plate through the rotation about the hinges. In the polysilicon case, there may be at most about $5\mu m$ of gap to slide a probe underneath a plate. Therefore, we used microjacks as an assembly aid (Section. 3.3.2). In the CMOS case, generally there would be a gap of tens of microns so that placing a probe underneath the plate is relatively easy. Because of the alignment designs, the plates must be lifted up in a sequence. For example, Fig. 5.13 shows the order of the plates to be rotated for the CCR design in Fig. 5.7.

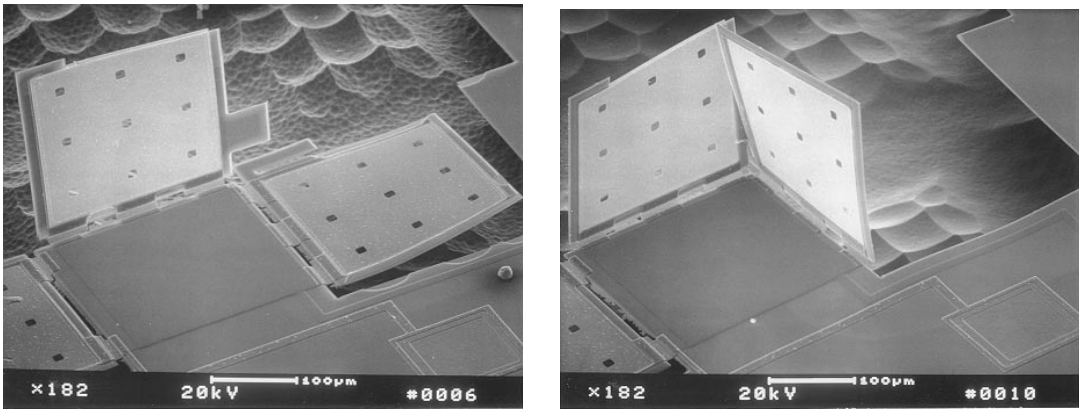

(a) (b)

Figure 5.13: The two vertical mirrors are lifted up in a sequence as shown in (a) and (b). These mirrors are made of a metal membrane supported by an oxide and poly frame. Residual stress has caused the membranes to curve.

Lifting up a CMOS plate could be easier than a polysilicon plate for another reason. While a polysilicon plate is being lifted up by a probe tip, if the probe accidentally loses contact with the plate, the plate would fall back down on the substrate because the hinges are a free pin-joint. On the other hand, as a CMOS hinged plate is being lifted up, the metal hinges are becoming plastically deformed so that even if the probe loses contact with the plate during the rotation, the plate would stay rotated and not fall back down toward the substrate.

Despite the advantages already described, overall CMOS microstructure assembly is more difficult than polysilicon assembly for several reasons. One main reason is that the silicon etch pit surrounding the structure is rough and unreflective. As a result, when a probe tip is placed above the pit, the probe tip is generally invisible through the microscope unless the probe tip is in perfect focus. Another reason is that the oxide plates are difficult to see under the microscope compared to the polysilicon plates, especially when the plate is near vertical. Part of the difficulty is due to the lack of light reflecting from the chip background. Furthermore, an

oxide plate, like glass, appears almost transparent unless some metal is present. Nevertheless, the presence of metal on a plate was found to offer limited benefits, such as when the plate is near flat or near 45 degrees from the substrate.

In spite of these difficulties, all the CMOS structures which are presented in this work were assembled using the same probe station setup as for the polysilicon structures with reasonable success. These assembly difficulties can be alleviated by setting the chip on a tilted stage or applying illumination to the side of the chip during assembly. Stereo-microscopes with high magnification would also significantly simplify the process.

6 Conclusion

6.1 Summary of Results

Fabricated polysilicon CCRs using a standardized MEMS process yielded functional CCRs with excellent mirror alignment but only satisfactory optical qualities and bandwidth. Precise mirror alignments were achieved using novel designs including torsional tie-down, tenon, and mortise. The largest (best) radius of curvature for fabricated mirrors was about $20mm$, leading to CCR-reflected beam divergence of about $20mrad$. Further improvement would require additional post-processing steps or refining the fabrication process.

Novel electrostatic actuator designs have bandwidth ranging from $500Hz$ to $3kHz$ and require 15 to $37V$. Angular motions of up to 3 degrees was achieved. Theoretical capacitance is about $0.3pF$ so that a CCR modulated at $10kH$ using $20V$ would consume only $0.6\mu W$. Measured actuator capacitance of package devices was about $1.55pF$, although actual capacitance of the device during operation is about $21pF$ due to pads and wiring layout. The mechanical design can definitely be improved to increase the bandwidth and power efficiency, but proper vacuum packaging will be necessary to create devices suitable for high data bandwidth applications. Self-assembled CCRs based on scratch-drive actuators were also designed and tested. Although no self-assembled devices were fully functional, self-assembly is shown to be a viable option for large volume CCR fabrication.

Fabricated CCRs devices, though unoptimized, successfully demonstrated data transmission across 150 meters at 4bps, consuming $16nW$ for mirror actuation.

Low data rate was limited by our commercial off-the-shelf hardware. The experimental results not only support our communication analysis but also strongly suggest that long range communication (greater than $1km$) is achievable with suitable improvement of the CCRs' performance (such as the mirror curvature) and the receiver system. Communication with multiple CCRs was also demonstrated, which suggests that CCRs can be used in applications requiring multiple communication channels.

We also demonstrated successful fabrication of static CCRs in CMOS using aluminum micro-hinges and a novel silicon etching process with vapor XeF_2. Fabricated mirrors made of aluminum and oxide have a large range of curvatures, but some designs were found to have less curvature than the polysilicon mirrors. Unfortunately, from our results, we cannot draw conclusions about the performance limit of CMOS-fabricated CCRs. Nevertheless, our results strongly support further development of monolithic CCR-based transmitters using CMOS.

6.2 Future Work

6.2.1 CCR Applications

In this work, we have shown that CCR-based communication links are definitely feasible. There are many potential applications where asymmetric power consumption between two communicating nodes can be beneficial. However, only field-testing of these CCR devices in different environments would indicate the best possible use of CCR-based communication links. Test environments may include the desert, the jungle, the North Pole, on the moon, outer-space, inside a

wind-tunnel, on the ocean, and even inside the ocean. At the end, the environmental effects in different applications will naturally define the best use of this communication technology.

6.2.2 Micro assembly and packaging

Micro assembly technology has an important role in the successful development of micromachined devices. For micro CCRs based on hinged plates, the need of a low-cost high-yield self-assembly process is especially critical in order to meet many potential application requirements. Although many MEMS designs have been demonstrated for micro-assembly, a common drawback is the requirement of large chip area. These micro-assembly devices (including scratch-drive actuators) must be further miniaturized to assemble small devices with high precise and lower cost.

Advanced packaging technology is also necessary to create rugged and useful micro CCRs and MEMS devices in general. Micro CCRs ideally should be sealed and packaged immediately after the sacrificial release etch and then activated to self-assemble inside the sealed medium. As an example, for infrared applications, a silicon wafer with micromachined cavities can be wafer-bonded to a CCR wafer after the sacrificial release etch. Then the wafer can be diced and appropriate packaged. Non-planar substrates or packages may also be considered to create CCR arrays with multiple orientations.

6.2.3 Actuator Designs

High bandwidth, low-power actuators have applications in micro CCRs as well as many other devices. Higher CCR bandwidth would allow not only high data

rate but also signal coding. Besides general mechanical design improvements, several aspects of the actuators designed in this work can be further investigated including squeeze-film damping for non-parallel surfaces, non-linear electrostatic feedback control, and impact actuation[56]. Among different micromechanical designs, micromachined diffraction gratings appear to provide the highest potential modulation speed for CCR applications; however, appropriate packaging is needed to make CCRs visible only to desired wavelengths. Designs of actuators using thermally reshaped polysilicon could also lead to interesting devices.

6.2.4 Process Development

Analog Devices has already shown that a combination of a MEMS single-layer polysilicon process with a CMOS electronics process can be used to produce commercially viable products. Development of process which combines multi-layer (and possibly thick-layer) polysilicon with CMOS may allow many interesting possibility. Hinged polysilicon technology combined with liquid-crystal and other electro-optics technology may also open doors to many interesting possibilities, especially in development of micro-optical MEMS.

References

[1] *ANSI Z136.1 Safe Use of Lasers*. The Laser Institute of America, Orlando, Florida, 1993.

[2] C. H. Ahn, Y. J. Kim, and M. G. Allen. A planar variable reluctance magnetic micromotor with fully integrated stator and wrapped coils. In *Proc. IEEE Micro Electro Mechanical Systems Workshop*, pages 1–6, Ft. Lauderdale, Florida, 1993.

[3] T. Akiyama, D. Collard, and H. Fujita. Scratch drive actuator with mechanical links for self-assembly of three-dimensional MEMS. *IEEE/ASME J. Microelectromechanical Systems*, 6(1):10–17, 1997.

[4] M. Andrews, I. Harris, and G. Turner. A comparison of squeeze-film theory with measurements on a microstructure. *Sensors and Actuators (A)*, 36:79–87, 1993.

[5] H. Baltes. CMOS as sensor technology. *Sensors and Actuators (A)*, 37-38:51–56, 1993.

[6] H. Baltes and D. Moser. CMOS vacuum sensors and other applications of cmos thermopiles. In *Proc. 7th Int. Conf. on Solid State Sensors and Actuators (Transducers '93)*, pages 736–741, Yokohama, June 7-10, 1993.

[7] K. W. Brendley and R. Steeb. Military applications of microelectromechanical systems. Technical Report MR-175-OSD/AF/A (ISBN: 0-8330-1344-0), RAND Corporation, Santa Monica, CA, 1993.

[8] J. Bühler, J. Funk, J. G. Korvink, F.-P. Steiner, P.M. Sarro, and H. Baltes. Electrostatic aluminum micromirrors using double-pass metallization. *IEEE/ASME J. Microelectromechanical Systems*, 6(2):126–135, 1997.

[9] S.R. Burgett, K.S.J. Pister, and R. Fearing. Three dimensional structures made with microfabricated hinges. In *Proc. Micromechanical Systems, ASME*, pages 1–11, Winter 1992.

[10] F.I. Chang, R. Yeh, G. Lin, P.B. Chu, E. Hoffman, E.J.J. Kruglick, K. S. J. Pister, and M.H. Hecht. Gas-phase silicon micromachining with xenon difluoride. In *Proceedings of the SPIE*, volume 2641, pages 117–28, Austin, TX, October 1995.

[11] J.Y. Chen. CMOS–the emerging VLSI technology. *IEEE Circuits and Devices Magazine*, 2:16, 1986.

[12] P. B. Chu, N. R. Lo, E. C. Berg, and K.S.J. Pister. Optical communication using micro corner cube reflectors. In *Proc. IEEE Micro Electro Mechanical Systems Workshop*, pages 350–355, Nagoya, Japan, 1997.

[13] P. B. Chu, P. R. Nelson, and K. S. J. Pister. Dynamics of polysilicon parallel-plate electrostatic actuators. *Sensors and Actuators (A)*, A52:216–220, 1996.

[14] P.B. Chu, J.T. Chen, R. Yeh, G. Lin, J. Huang, B. Warneke, and K.S.J. Pister. Controlled pulse-etching with Xenon Difluoride. In *Proc. 9th Int. Conf. on Solid State Sensors and Actuators (Transducers '97)*, pages 665–668, Chicago, June 16-19, 1997.

[15] P.F. Combes. *Microwave Transmission for Telecommunications*. John Wiley & Sons, Inc., New York, 1991.

[16] J.H. Comtois and V. Bright. Surface micromachined polysilicon. In *Proc. IEEE Solid State Sensor and Actuator Workshop*, pages 174–177, Hilton Head, South Carolina, June 2-6, 1996.

[17] T.A. Core, W.K. Tsang, and S.J. Sherman. Fabrication technology for an integrated surface-micromachined sensor. *Solid State Technology*, pages 39–47, Oct. 1993.

[18] L.W. Couch. *Digital and Analog Communication Systems.* Macmillian Publishing Company, 1993.

[19] M.J. Daneman, N.C. Tien, O. Solgaard, K.Y. Lau, and R. Muller. Linear vibromotor-actuated micromachined microreflector for integrated optical systems. In *Proc. IEEE Solid State Sensor and Actuator Workshop*, pages 213–220, Hilton Head, South Carolina, June 2-6, 1996.

[20] W.G. Driscoll. *Handbook of Optics.* McGraw-Hill, Inc., New York, 1978.

[21] B. Eyre and K.S.J. Pister. Micromechanical resonant magnetic sensor in standard CMOS. In *Proc. 9th Int. Conf. on Solid State Sensors and Actuators (Transducers '97)*, pages 405–408, Chicago, June 16-19, 1997.

[22] L.-S. Fan, Y.-C. Tai, and R.S. Muller. Integrated movable micromechanical structures for sensors and actuators. *IEEE Trans. Electron Devices*, 35(6):724–730, 1988.

[23] L.S. Fan, Y.C. Tai, and R.S. Muller. IC-processed electrostatic micromotors. *Sensors and Actuators*, 20(1&2):41–47, 1989.

[24] L.S. Fan, Y.C. Tai, and R.S. Muller. Pin-joints, springs, cranks, gears, and other novel micromechanical structures. In *Proc. 4th Int. Conf. on Solid State Sensors and Actuators (Transducers '87)*, pages 849–852, Tokyo, Japan, June 1987.

[25] G.K. Fedder, S. Santhanam, M.L. Reed, S.C. Eagle, D.F. Guillou, M.S.-C. Lu, and L.R. Carley. Laminated high-aspect-ratio microstructures in a conventional CMOS process. In *Proc. IEEE Micro Electro Mechanical Systems Workshop*, pages 13–18, San Diego, California, 1996.

[26] E.R. Fossum. CMOS image sensor: electronics camera-on-a-chip. *IEEE Trans. Electron Devices*, 44(10):1689–98, 1997.

[27] J. Gowar. *Optical Communication System.* Prentice-Hall International, Inc., London, 1984.

[28] H. Guckel, T. R. Christenson, K. J. Skrobis, T. S. Jung, and J. Klein. A first functional current excited planar rotational magnetic micromotor. In *Proc. IEEE Micro Electro Mechanical Systems Workshop*, pages 7–11, Ft. Lauderdale, Florida, 1993.

[29] R.D. Guenther. *Modern Optics.* John Wiley & Sons, Inc., New York, 1990.

[30] D. S. Gunawan. Micromachined corner cube reflectors as a communication link. Master's thesis, University of California, Los Angeles, 1994.

[31] D. S. Gunawan, L.-Y. Lin, and K.S.J. Pister. Micromachined corner cube reflectors as a communication link. *Sensors and Actuators (A)*, 46-47:580–583, 1995.

[32] E. Hecht. *Optics.* Addision-Wesley Publishing Company, Inc., Massachusetts, 2nd edition, 1987.

[33] C. Hierold, A. Hilderbrandt, U. Naher, T. Scheiter, B. Mensching, M. Steger, and R. Tielert. A pure CMOS surface micromachined integrated accelerometer. In *Proc. IEEE Micro Electro Mechanical Systems Workshop*, pages 174–179, San Diego, California, 1996.

[34] E. Hoffman, B. Warneke, E. Kruglick, J. Weigold, and K. S. J. Pister. 3D structures with piezoresistive sensors in standard CMOS. In *Proc. IEEE Micro Electro Mechanical Systems Workshop*, pages 288–93, Amsterdam, Netherlands, 1995.

[35] P. Horowitz and W. Hill. *The Art of Electronics.* Cambridge University Press, Cambridge, 2th edition, 1992.

[36] M.R. Houston, R. Maboudian, and R.T. Howe. Self-assembled monolayer films as durable anti-stiction coatings for polysilicon microstructures. In *Proc. IEEE Solid State Sensor and Actuator Workshop*, pages 42–47, Hilton Head Island, South Carolina, June 3-6, Hilton Head, South Carolina, June 2-6, 1996.

[37] R.T. Howe and R.S. Muller. Polycrystalline silicon micromechanical beams. *Journal of Electrochemical Society*, 130:1420–1423, 1983.

[38] V.S. Hsu, J.M. Kahn, and K.S.J. Pister. Wireless communications for smart dust. Technical Report UCB/ERL M98/2, UC Berkeley Electronics Research Laboratory, Berkeley, CA94720, December 1998.

[39] D.E. Ibbotson, D. L. Flamm, J. A. Mucha, and V. M. Donnelly. Comparison of XeF_2 and F-atom reactions with Si and SiO_2. *Appl. Phys. Lett.*, 44(12):1129–1131, 1984.

[40] D.E. Ibbotson, J.A. Mucha, D.L. Flamm, and J.M. Cook. Plasmaless dry etching of silicon with fluorine-containing compounds. *J. Appl. Phys.*, 56(10):2939–42, 1984.

[41] V.P. Jaecklin, C. Linder, J.-M. Brugger, J. Moret, R. Vuilleumier, and N.F. de Rooij. Mechanical and optical properties of surface micromachined torsional mirrors in silicon, polysilicon and aluminum. In *Proc. 7th Int. Conf. on Solid State Sensors and Actuators (Transducers '93)*, pages 958–961, Yokohama, June 7-10, 1993.

[42] D. Jaeggi. *Thermal Converters by CMOS Technology.* PhD thesis, ETH Zurich, Physical Electronics Laboratory, Swiss Federal Institute of Technology, Zurich, 1996.

[43] D. Jaeggi, C. Azeredo Leme, P. O'Leary, and H. Baltes. Improved cmos ac power sensor. In *Proc. 7th Int. Conf. on Solid State Sensors and Actuators (Transducers '93)*, pages 462–465, Yokohama, June 7-10, 1993.

[44] G. Jensen and C. Swenson. A laser downlink for small satellites using an optically modulating retroreflector. In *Proc. 6th Annual AIAA/USU Conf. on Small Satellites*, Sept. 21-24 1992.

[45] J.W. Judy and R.S. Muller. Batch-fabricated, addressable, magnetically actuated microstructures. In *Proc. IEEE Solid State Sensor and Actuator*

Workshop, pages 187–190, Hilton Head Island, South Carolina, June 3-6, Hilton Head, South Carolina, June 2-6, 1996.

[46] M.W. Judy, Y-H. Cho, R.T. Howe, and A.P. Pisano. Self-adjusting microstructures (SAMS). In *Proc. IEEE Micro Electro Mechanical Systems Workshop*, pages 51–56, Nara, Japan, Jan. 30 - Feb. 2, 1991.

[47] J.M. Kahn and J.R. Barry. Wireless infrared communications. *Proceedings of the IEEE*, 31(28):6015–6020, February 1997.

[48] J.Y. Kim and C.-J. Kim. Comparative study of various release methods for polysilicon surface micromachining. In *Proc. IEEE Micro Electro Mechanical Systems Workshop*, pages 442–447, Nagoya, Japan, 1997.

[49] C.R. King, L.Y. Lin, and M.C. Wu. Out-of-plane refractive microlens fabricated by surface micromachining. *IEEE Photonics Technology Letters*, 8(10):1349–1351, October 1996.

[50] E.H. Klaassen, R.J. Reay, C. Storment, Audy J., P. Henry, A.P. Brokaw, and G.T.A. Kovacs. Micromachined thermally isolated circuits. In *Proc. IEEE Solid State Sensor and Actuator Workshop*, pages 127–131, Hilton Head, South Carolina, June 2-6, 1996.

[51] E. J. J. Kruglick, S. Damle, and K. S. J. Pister. Three-dimensional structures for micro-optical mechanical systems in standard CMOS. In *Proceedings of the SPIE*, volume 2642, pages 33–9, Micromachined Devices and Components, Austin, TX, October 1995.

[52] E.J.J. Kruglick. Aluminum hinges and electrostatic actuators in standard CMOS. Master's thesis, University of California, Los Angeles, 1996.

[53] E.J.J. Kruglick, B.A. Warneke, and K.S.J. Pister. CMOS 3-axis accelerometers with integrated amplifier. In *Proc. IEEE Micro Electro Mechanical Systems Workshop*, pages 631–6, Heidelberg, Germany, 1998.

[54] S.G. Lambert and W.L. Casey. *Laser Communications in Space.* Artech House, Inc., MA, 1996.

[55] P. Langlet, D. Collard, T. Akiyama, and H. Fujita. A quantitative analysis of scratch drive actuator for integrated x/y motion system. In *Proc. 9th Int. Conf. on Solid State Sensors and Actuators (Transducers '97)*, pages 773–76, Chicago, June 16-19, 1997.

[56] A.P. Lee. *Impact Actuation of Polysilicon Micromechanical Structures.* PhD thesis, University of California, Berkeley, Berkeley, CA 94720, 1992.

[57] S.S. Lee, L.-Y. Lin, and M.C. Wu. Realization of FDDI optical bypass switches using surface micromachining technology. In *Proceedings of the SPIE*, volume 2641, pages 41–8, 1995.

[58] S.S. Lee, L.Y. Lin, and K.S.J. Pister. Surface-micromachined free-space fiber optic switches. *Electronics Letters*, 31:1481–1482, 1995.

[59] Y.-I. Lee, K.-H. Park, J. Lee, C.-S. Lee, H.J. Yoo, C.-J. Kim, and Y.-S. Yoon. Dry release for surface micromachining with HF vapor-phase etching. *IEEE/ASME J. Microelectromechanical Systems*, 6(3):226–233, 1997.

[60] R. Lenggenhager, Jaeggi D., P. Malcovati, H. Duran, H. Baltes, and E. Doering. CMOS membrane infrared sensors and improved TMAHW etchant. In *Proc. IEEE International Electron Devices Meeting*, pages 531–4, 1994.

[61] G. Lin. *MEMS force transducer system for cellular force measurements.* PhD thesis, University of California, Los Angeles, Los Angeles, CA 90095, 1998.

[62] G. Lin, R.E. Palmer, K.S.J. Pister, and K.P. Roos. Single heart cell force measured in standard CMOS. In *Proc. 9th Int. Conf. on Solid State Sensors and Actuators (Transducers '97)*, pages 199–200, Chicago, June 16-19, 1997.

[63] L.Y. Lin, S.S. Lee, K.S.J. Pister, and M.C. Wu. Three-dimensional micro-Fresnel optical elements fabricated by micromachining technique. *Electronics Letters*, 30(5):448–9, March 1994.

[64] L.Y. Lin, J.L. Shen, S.S. Lee, and M.C. Wu. Surface-micromachined micro-XYZ stages for free-space microoptical bench. *IEEE Photonics Technology Letters*, 9(3):345–347, March 1997.

[65] M.M. Liu. *Principles and applications of optical communications.* Richard D. Irwin, a Times Mirror Higher Education Group, Inc., MA, 1996.

[66] J. Marshall, M. Gaitan, M. Zaghloul, D. Novotny, V. Tyree, J.I. Pi, C. Piñó, and W. Hansford. Realizing suspended structures on chips fabricated by CMOS foundry processes through the MOSIS service. Technical Report NISTIR 5402, National Institute of Standards and Technology, June 1994.

[67] R.A. Miller, G.W. Burr, Y.-C. Tai, D. Psaltis, C.-H. Ho, and R. R. Katti. Electromagnetic mems scanning mirrors for holographics data storage. In *Proc. IEEE Solid State Sensor and Actuator Workshop*, pages 183–186, Hilton Head Island, South Carolina, June 3-6, Hilton Head, South Carolina, June 2-6, 1996.

[68] A. Minato, N. Sugimoto, and Sasano Y. Optical design of cube-corner retroreflectors having curved mirror surfaces. *Applied Optics*, 31(28):6015–6020, October 1992.

[69] W.L. Morgan and G.D. Gordon. *Communications Satellites handbook*. John Wiley & Sons, Inc., New York, 1989.

[70] D. Moser, O. Brand, and H. Baltes. A CMOS compatible thermally excited silicon oxide beam resonator with aluminium mirror. In *Proc. 6th Int. Conf. on Solid State Sensors and Actuators (Transducers '91)*, pages 547–550, San Francisco, June 1991.

[71] D. Moser, R. Lenggenhager, and H. Baltes. Silicon gas flow sensors using industrial CMOS and bipolar technology. *Sensors and Actuators (A)*, 27:577–581, 1991.

[72] G.T. Mulhern, D.S. Soane, and R.T. Howe. Supercritical carbon dioxide drying of microstructures. In *Proc. 7th Int. Conf. on Solid State Sensors and Actuators (Transducers '93)*, pages 296–299, Yokohama, June 7-10, 1993.

[73] M. Parameswaran, H.P. Baltes, L. Ristic, A.C. Dhaded, and A.M. Robinson. A new approach for the fabrication of micromachined structures. *Sensors and Actuators (A)*, 19:289–307, 1989.

[74] A. Paul, O. Haberli, P. Malcovati, and H. Baltes. Novel integrated thermal pressure gauge and read-out circuit. In *Proc. IEEE International Electron Devices Meeting*, pages 131–4, 1994.

[75] O. Paul, D. Westberg, Hornung M., V. Ziebart, and H. Baltes. Sacrificial aluminum etching for CMOS microstructures. In *Proc. IEEE Micro Electro Mechanical Systems Workshop*, pages 523–528, Nagoya, Japan, 1997.

[76] Kurt E. Petersen. Silicon as a mechanical material. *Proceedings of the IEEE*, 70(5):420–457, May 1982.

[77] K.S.J. Pister, M.W. Judy, S.R. Burgett, and R.S. Fearing. Microfabricated hinges. *Sensors and Actuators (A)*, 33(3):249–256, 1992.

[78] C.R. Pollock. *Fundamentals of Optoelectronics.* Richard D. Irwin, a Times Mirror Higher Education Group, Inc., MA, 1995.

[79] M. Rafalowski. Determination of the working area for the corner-cube mirror system with variable angle of incident beam for interferometric applications. *Optica Applicata*, 25(2):141–8, 1995.

[80] W. Riethmuller, W. Benecke, U. Schnakenberg, and B. Wagner. Development of commerical CMOS process-based technologies for the fabrication of smart accelerometers. In *Proc. 6th Int. Conf. on Solid State Sensors and Actuators (Transducers '91)*, pages 416–419, San Francisco, June 1991.

[81] L. Ristic. CMOS technology: A base for micromachining. *Microelectronics Journal*, 20:153, 1989.

[82] B.E.A. Saleh and M.C. Teich. *Fundamentals of Photonics.* John Wiley and Sons, New York, 1991.

[83] U. Schnakenberg, W. Benecke, and P. Lange. TMAHW etchants for silicon micromachining. In *Proc. 6th Int. Conf. on Solid State Sensors and Actuators (Transducers '91)*, pages 815–818, San Francisco, June 1991.

[84] M.S. Scholl. Ray trace through a corner-cube retroreflector with complex reflection coefficients. *Journal of the Optical Society*, 12(7):5394–7, 1995.

[85] W.N. Sharpe, B. Yuan, R. Vaidyanathan, and R. L. Edwards. Measurements of Young's modulus, Poisson's ratio, and tensile strength of polysilicon. In *Proc. IEEE Micro Electro Mechanical Systems Workshop*, Nagoya, Japan, 1997.

[86] D.H. Sliney. *Laser Safety Guide*. The Laser Institute of America, Orlando, Florida, 9th edition, 1993.

[87] U. Srinivasan, M. R. Houston, R.T. Howe, and R. Maboudian. Self-assembled fluorocarbon films for enhanced stiction reduction. In *Proc. 9th Int. Conf. on Solid State Sensors and Actuators (Transducers '97)*, pages 1399–1402, Chicago, June 16-19, 1997.

[88] J.B. Starr. Squeeze-film damping in solid-state accelerometers. In *Proc. IEEE Solid State Sensor and Actuator Workshop*, pages 44–47, Hilton Head, South Carolina, June 4-7, 1990.

[89] C.W. Storment, D.A. Borkholder, V. Westerlind, J.W. Suh, N.I. Maluf, and G.T.A. Kovacs. Flexible, dry-released process for aluminum electrostatic actuators. *IEEE/ASME J. Microelectromechanical Systems*, 3(3):90–96, 1994.

[90] Y.C. Tai and R.S. Muller. Fracture strain of LPCVD polysilicon. In *Proc. IEEE Solid State Sensor and Actuator Workshop*, pages 88–91, Hilton Head, South Carolina, June 6-9, 1988.

[91] W.C. Tang, T.H. Nguyen, and R.T. Howe. Laterally driven polysilicon resonant microstructures. *Sensors and Actuators*, 20:25–32, 1989.

[92] N.R. Tas, A.H. Sonnenberg, A.F.M. Sander, and M.C. Elwenspoek. Surface micromachined linear electrostatic stepper motor. In *Proc. IEEE Micro Electro Mechanical Systems Workshop*, pages 215–220, Nagoya, Japan, 1997.

[93] T. Tsumura. Optical two-way vehicle-to-vehicle communication by the use of laser and corner cube. In *Robotics and Autonomous Systems*, number 1-2, pages 81–6, 1996.

[94] T. Tsumura, H. Okubo, H. Komatsu, and N. Aoki. A proposed automobile communication and traffic control system. In *Proc. International Symposium on Advanced Vehicle*, pages 535–8, 1992.

[95] X.-Q. Wang, X. Yang, K. Walsh, and Y.-C. Tai. Gas-phase silicon etching with bromine trifluoride. In *Proc. 9th Int. Conf. on Solid State Sensors and Actuators (Transducers '97)*, pages 1505–1508, Chicago, June 16-19, 1997.

[96] B. A. Warneke. Triaxial monolithic piezoresistive accelerometers in foundry CMOS. Master's thesis, University of California, Los Angeles, 1996.

[97] K. William and R. Muller. Etch rates for micromachining processing. *IEEE/ASME J. Microelectromechanical Systems*, 5(4):256–269, 1996.

[98] M.C. Wu. Micromachining for optical and optoelectronic systems. *Proceedings of the IEEE*, 85(11):1833–1856, November 1997.

[99] R. Yeh, E.J.J. Kruglick, and K.S.J. Pister. Surface-micromachined components for articulated microrobots. *IEEE/ASME J. Microelectromechanical Systems*, 5(1):10–17, 1996.

[100] W.C. Young. *Roark's Formulas for Stress & Strain*. McGraw-Hill, Inc., New York, 6th edition, 1989.